Electronic Transport in a Magnetic Topological Insulator $(V,Bi,Sb)_2Te_3$

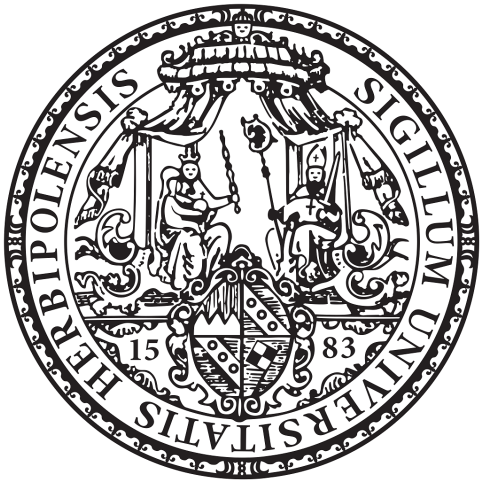

Dissertation zur Erlangung des naturwissenschaftlichen Doktorgrades der Julius-Maximilians-Universität Würzburg

vorgelegt von:

Kajetan Maciej Fijalkowski

aus Kluczbork, Polen

Würzburg, 2021

Eingereicht am: 11.10.2021

bei der Fakultät für Physik und Astronomie.

1. Gutachter: Prof. Dr. Charles Gould

2. Gutachter: Prof. Dr. Ronny Thomale

3. Gutachter: Prof. Dr. Tomasz Dietl

der Dissertation.

Vorsitzender: Prof. Dr. Bert Hecht

1. Prüfer: Prof. Dr. Charles Gould

2. Prüfer: Prof. Dr. Ronny Thomale

3. Prüfer: Prof. Dr. Sebastian Klembt

im Promotionskolloquium.

Tag des Promotionskolloquiums: 15.07.2022

Doktorurkunde ausgehändigt am:

Contents

List of abbreviations.

- OHE - Ordinary Hall Effect
- AHE - Anomalous Hall Effect
- AH - Anomalous Hall
- QHE - Quantum Hall Effect
- QSHE - Quantum Spin Hall Effect
- QAHE - Quantum Anomalous Hall Effect
- TI - Topological Insulator
- TIs - Topological Insulators
- 1D - One-dimensional
- 2D - Two-dimensional
- 3D - Three-dimensional
- ARPES - Angle Resolved Photoemission Spectroscopy
- MBE - Molecular Beam Epitaxy
- XRD - X-ray Diffraction
- XRR - X-ray Reflectivity
- ALD - Atomic Layer Deposition
- UHV - Ultra High Vacuum

- DC - Direct Current
- AC - Alternating Current
- PTB - Physikalisch Technische Bundesanstalt
- CCC - Cryogenic Current Comparator
- SQUID - Superconducting Quantum Interference Device
- SC - Superconducting
- ZHP - Zero Hall plateau

Chapter 1

Context and motivation.

The breakthrough discovery by Edwin Hall in 1879 of what we now know as the ordinary Hall effect (OHE) [1], created a useful scientific tool, and laid the foundation of modern solid state physics as we know it. Two years later in 1881 Edwin Hall noticed that the same effect, in magnetic materials, exhibits interesting additional properties. This brought to life a second member of the Hall effects family; the anomalous Hall effect (AHE) [2]. Studied extensively since, the AHE still remains enigmatic in some theoretical aspects as a universal theory of the effect is still missing, despite a high degree of phenomenological understanding in a variety of material systems [3]. To this day the AHE remains a valuable tool in material characterization, and it's investigation in modern materials continues to yield rich novel physics.

Condensed matter has since risen to become one of the most important fields in physics, as evidenced by a large amount of breakthrough discoveries made over the years. In the context of this thesis, some are more relevant than the others. These include the experimental discoveries of the quantum Hall effect (QHE) in 1980 [4], massless Dirac fermions in graphene in 2005 [5] and the first insulating state of nontrivial topology in HgTe/(Hg,Cd)Te quantum wells manifested as the quantum spin Hall effect (QSHE) in 2007 [6]. Moreover in the last few years magnetic doping of topological insulators gained a lot of attention due to a discovery of a quantized version of the AHE, the quantum anomalous Hall effect (QAHE) in 2013 [7].

From the practical application standpoint, due to its quantized conductance at zero external magnetic field, the QAHE was quickly recognized as a potential successor to the QHE for quantum resistance metrology. Operation at zero external magnetic field provides an extraordinary advantage, as it should allow one to combine the quantum resistance

standard with the quantum voltage standard based on the AC Josephson effect [8, 9] into a single reference instrument in the future. Such a combined instrument would be capable of providing a universal quantum electrical standard, potentially useful for a quantum kilogram standard based on the electromechanical Kibble (or Watt) balance [10, 11]. This promise is already supported by experimental results where quantum resistance metrology methods were implemented to confirm the zero field transport quantization to an excellent precision [12, 13]. This experiment however requires both ultra low temperature (less then 100mK) and low current (of the order of nanoamps), thus leaving challenges to making a commercially feasible quantum standard in the future.

The reason behind the requirement of such low temperatures for the observation of the QAHE still remains an open question. A level of understanding of magnetic state in prototypical QAHE materials: V and Cr doped $(Bi,Sb)_2Te_3$ [7, 14] remains rather low. Many in the literature describe the state as simply "ferromagnetic". Experiments however reveal that in addition to the ferromagnetic component, there is evidence of superparamagnetism and magnetic fluidity [15, 16], or even claims of adiabatic cooling [17]. The reason for difference in magnetic anisotropy between the V and Cr doped layers [14] also remains not understood. A detailed analysis of the AHE indicates the coexistence of surface and bulk ferromagnetism in these material class [18], and some reports claimed the existence of skyrmion Hall effect [19]. All of this points towards a more complicated mechanism driving the magnetism in the material, and a deeper understanding of the underlying magnetism will likely lead to a deeper understanding of the QAHE itself.

When the Hall resistance is quantized, it is clear that the electronic transport is carried by the chiral edge channels. The situation is not at all clear when the temperature is increased and the Hall signal drops below the quantized value, as observed in the experiment. As in a traditional Hall bar geometry, due to a uniform current distribution, it is impossible to clearly separate the chiral edge channels contribution from the bulk AHE, it is not clear if the chiral edge channels even exist at temperatures approaching the Curie temperature of the material, which in the involved materials is typically of the order of 20 K [7, 14]. The implementation of a multi-terminal Corbino geometry allowed for a proper experimental separation of the ordinary bulk transport and chiral edge channel contributions, establishing that indeed the chiral quantum anomalous Hall channels survive as long as the material remains ferromagnetic. This in turn allows the identification of thermally activated bulk conductance electrically shorting the edge channels, as the main reason why the experimentally observed quantization is constrained to ultra low temperatures. This

further shows that the quantization breakdown is not a feature of the topological edge channels itself, indicating that the protection of a topological state is robust against temperature. This is extremely promising for potential applications, as in principle in order to increase the operational temperature of the QAHE, now we know that the bulk resistivity is the parameter that needs to be improved.

From the academic interest perspective, the QAHE provides a vast playing field for interesting physics. It is a result of two ingredients: topology and magnetism. If one successfully manages to introduce a third ingredient in the form of superconducting correlations, it should in principle be possible to create a chiral topological superconductor [20], where quasi-particle excitations behave like Majorana fermions, particles that are their own antiparticles. This has recently attracted a lot of attention in the community, even with claims of experimental detection of chiral Majorana fermions in 2017 [21], however recent experimental results bring those earlier claims into question [22], implying that this exotic quasi-particle still remains elusive. Nonetheless the search for experimental signatures of chiral topological superconductivity goes on.

Another fascinating consequence of topological properties is axion electrodynamics. Frank Wilczek noticed in 1987 [23], that the same equations as those from axion electrodynamics [24] describe electrodynamics on the "anti-phase boundaries" in PbTe, what we now know as the topological surface state of a three-dimensional topological insulator. This in turn modifies the Maxwell equations governing the electrodynamics in the system. While the search for axion electrodynamics in particle physics remains unsuccessful, solid state manifestations of the effect already brought to life a rich phenomenology [25, 26, 27, 28, 29], and the search for further signatures continues.

Chapter 2

Introduction.

2.1 Topological insulators.

In this section I briefly describe the concept of topological insulators (TIs), mainly focusing on dimensionality of the system as this is going to be important in the context of some of the experimental results in this thesis. After that I discuss the concept of magnetic doping of topological insulators, and as a consequence the QAHE.

2.1.1 2D and 3D topological insulators.

Topology is a way of classifying things, where in the context of solid state systems one talks about the topology of the band structure. In that sense one can classify insulating materials into different categories, "topological" and "trivial" (or "non-topological"). In trivial insulators it is possible through smooth deformations to transform the band structure into a vacuum equivalent, where "smooth deformation" strictly means that no electronic bands can cross. In case of a TI such smooth deformation to the vacuum is not possible, as band ordering is distinct from a trivial state, and band crossing must happen upon the deformation.

When such a TI is surrounded by a trivial insulator (or vacuum), a metallic boundary state appears at the interface between the two. This is a direct consequence of the band ordering in the two interfaced insulating materials, where the distinct topology ensures that energy bands must cross the Fermi level at the interface between the two materials. This leads to existence of gapless electronic states with low-energy linear band dispersion described by the Dirac equation, where elementary quasiparticle excitations are Dirac

Fermions [30].

The physical properties of the boundary state depend crucially on the dimensionality of the TI material itself, as the boundary state (in the first order TIs) is always one dimension lower then the topologically distinct bulk. First discovered experimentally was a 2D TI state in HgTe/HgCdTe quantum wells [6], where a 2D topological bulk results in the 1D dissipationless helical edge states at the boundary, the QSHE characterized by a quantized electronic conductance signature in the experiment. Shortly after, the dispersion of a 2D boundary state of a $Bi_{1-x}Sb_x$ 3D TI was measured using angle-resolved photoemission spectroscopy (ARPES), revealing a Dirac cone-like band structure [31]. ARPES experiments in a Bi_2Se_3 TI reveal a thickness driven transition between the 3D and 2D regime [32] happening at approx. 6 nm, where below this thickness the surface Dirac cone was found to develop a gap resulting from the hybridization between top and bottom plane of the film.

2.1.2 Magnetic doping of topological insulators.

Masaru Onoda and Naoto Nagaosa proposed in 2003 the existence of quantized version of the AHE, the QAHE in 2D ferromagnets [33]. It turned out that experimental breakthrough required adaptation of this idea into 2D TIs, where the same effect was predicted to emerge upon magnetic doping of 2D TIs [34, 35]. First experimental observation of the effect in Cr-doped $(Bi,Sb)_2Te_3$ came in 2013 [7], reproduced by few other groups shortly after [36, 37, 17, 38]. The second material from the same family experimentally confirmed to exhibit the QAHE was V-doped $(Bi,Sb)_2Te_3$ [15, 14], interestingly at the same time showing considerably larger out-of-plane magnetic anisotropy than its Cr-doped counterpart [14], reason of which still remains an open question.

The initial idea behind the QAHE in TIs pertained to a 2D system, where the band inversion of one spin species is lifted by exchange interaction resulting from the magnetic doping [34, 35]. In this scenario the QSHE with two helical edge modes gets transformed into a state with single chiral edge state, constituting the QAHE characterized by a quantized Hall conductivity $\sigma_{xy} = e^2/h$. Perspective of the QAHE in a 3D system is rather different and ties to axion electrodynamics [25]. A half-integer quantized contribution to Hall conductivity $\sigma_{xy} = e^2/2h$ is predicted to emerge from a single topological surface state with magnetization normal to its surface enclosing a volume with axion electrodynamics. A material system exhibiting such half-integer quantization can be regarded as an "axion insulator", and a half-integer quantization itself a direct evidence for axion electrodynamics.

In a realistic experimental setting, it is impossible to investigate such isolated surface. In a transport experiment in the flat film geometry, in a 3D TI one probes two parallel planes ("top" and "bottom") dominating the transport properties. In that scenario one expects to detect the same topological contribution twice, resulting in a total Hall conductivity being a sum $\sigma_{xy} = e^2/2h + e^2/2h = e^2/h$, which interestingly is equivalent to a signature expected from a two dimensional system where $\sigma_{xy} = e^2/h$. As I present in this thesis, an experimental signature distinguishing between the 2D and 3D limits is a fundamental scaling of conductivity tensor elements adapted to the flat film geometry, predicted by Kentaro Nomura and Naoto Nagaosa in 2011 for an isolated surface on a cylinder [25]. Specifically the location of the central point in the scaling is robust against the number of parallel channels, thus providing a direct experimental probe of axion electrodynamics and axion insulating state in a 3D magnetic TI [28].

2.2 Experimental details.

In this section I present a brief description of the experimental techniques, material growth and device fabrication used in the thesis.

2.2.1 Molecular beam epitaxy of (V,Bi,Sb)$_2$Te$_3$ layers.

The material system investigated throughout this thesis is $V_y(Bi_{1-x}Sb_x)_{2-y}Te_3$, where "y" is the magnetic doping level and "x" is the Sb fraction of nonmagnetic atoms from the group 5 elements. Thin films with thickness ranging from 5 to 11 nm were grown on insulating hydrogen passivated 2 inch Si(111) substrates, using molecular beam epitaxy (MBE). The grown layers were capped in-situ with a 8 to 10 nm thick layer of Te, to prevent oxidation of the surface of the film, and provide a protection from the chemicals used in the lithography process. Te cap is insulating at investigated temperature range. The MBE system is equipped with thermal effusion cells and the substrate temperature control during the growth. Films investigated in this thesis were grown at temperature of 190 degrees centigrade. Material content (the magnetic doping level and the Bi/Sb ratio) was controlled by variation of the fluxes from the effusion cells, by precise cell temperature control. After the growth the Bi/Sb ratio was determined using X-ray diffraction (XRD) measurement of the lattice constants [39], and layer thickness was determined using X-ray reflectivity (XRR) method. In case of magnetic hetero-structures where magnetic doping level is varied along the growth direction, doped/undoped interfaces were controlled by

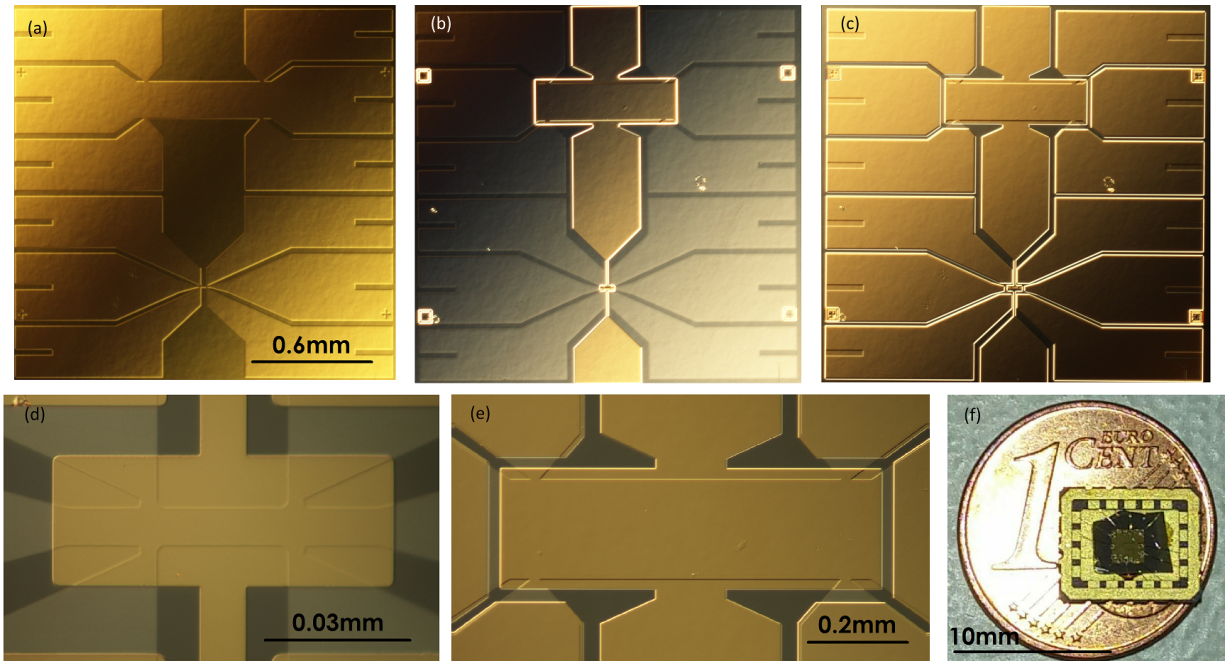

Figure 2.1: Optical microscope images of one of the samples. (a) First lithographic step, (b) second lithographic step, (c) third lithographic step (image magnification is the same in (a), (b), and (c)), image of the finished (d) small Hall bar device, and (e) big Hall bar device, and (f) photo of the processed glued sample. Figure taken from [18].

opening/closing V cell shutter during the co-deposition.

For more details regarding the epitaxy and structural properties of the grown films, the reader is referred to the ref. [39], as well as doctoral theses of Dr. Martin Winnerlein [40], and Dr. Steffen Schreyeck [41].

2.2.2 Typical device fabrication and lithography.

After the MBE growth, a sample of proper size (big enough to accommodate the device and small enough to fit inside the chip carrier) is manually cleaved with a diamond tip. Electrical transport devices are patterned using standard optical lithography methods. In the first step a mesa is patterned using Ar milling (Fig. 2.1a). For the top gate fabrication the sample is transfered into the atomic layer deposition (ALD) chamber where a dielectric layer is deposited, consisting of 15 nm of AlOx followed by 1 nm of HfOx. After the ALD process the gate metal stack is evaporated in an ultra-high vacuum (UHV) e-beam evaporator, consisting of 5 nm of Ti (sticking agent) and 100 nm of Au (Fig. 2.1b). Finally ohmic contacts are patterned (Fig. 2.1c). For that a sample is transferred into a UHV

chamber where the protective Te cap is removed from the contact area using Ar milling, and after that without braking the UHV conditions the sample is transfered into an e-beam evaporator where 50 nm AuGe / 2 nm Ti / 50 nm Au layer stack is deposited. Figs. 2.1d and e show optical microscope images of patterned Hall bar devices, the sample contains two Hall bars of the same aspect ratio 3:1 and different widths: 10 and 200 μm. After the lithographic process the sample is glued with a GE varnish to a chip carrier (Fig. 2.1f), and electrically connected with Au wires using a mechanical wedge bonder.

2.2.3 Transport experiment details.

Every transport experimental setup is adapted to the layout of the chip carrier hosting the sample. The sample gets mounted on the sample stick or a cold finger that contains a proper wiring. At room temperature outside of the cryostat, every contact on the device is accessible with coaxial cable connections via a break-out-box. The transport measurements are always performed in a linear ohmic response regime, with a voltage biased scheme with a small calibrated series resistor for a current value determination. Some of the measurements are DC with a total voltage excitation in the range of 1-10 mV, whereas majority of the collected measurements are low frequency AC with frequency lower than 20 Hz and use of lock-in amplifiers. When specified, additional high input impedance (approx. 1 TΩ) differential amplifiers were used to remove the influence of approx. 10 MΩ input impedance of the lock-in instruments. At temperature above 1.4 K the AC voltage excitation amplitude is typically in the range 1-10 mV) whereas at lower temperature (especially in the QAHE regime) excitation does not exceed 100 μV.

Transport experimental setups used in this thesis can be divided into two groups: ^{4}He cryostats, and dilution refrigerators. Every setup is equipped with a superconducting magnet with a field in the direction perpendicular to plane of the sample for Hall measurements. ^{4}He cryostats are ordinary vacuum dewars with a ^{4}He directly cooling the sample, either physically submerged in the liquid or via exchange gas. When actively pumping on the ^{4}He liquid surface, the lowest accessible temperature is approx. 1.4 K. This is as a result of the balance between the heat load and the pumping efficiency.

Lower temperature measurements (below 1 K) are performed in dilution refrigerators, where thermodynamic properties of the ^{3}He/^{4}He isotope mixture are used. At sufficiently low temperature, there are two thermodynamically stable phases of such mixture, a "condensed phase" (almost pure ^{3}He) and a "diluted phase" (approx. 6.6 percent of ^{3}He). Vapor pressure of ^{3}He is significantly higher than that of ^{4}He (at 700 mK in the still, where the

liquid-gas interface is located it is approx a factor of 1000), which allows by means of external pumping system to efficiently remove ^{3}He from the diluted phase, and then externally return it into the condensed phase. This creates an osmotic pressure difference between the two phases, forcing ^{3}He atoms to flow from the condensed phase to the diluted phase, resulting in a continuous phase transition. Heat cost of that phase transition is actively cooling the sample. Thermodynamically this process resembles a continuous "evaporation", as ^{3}He atoms in the diluted phase move without any obstruction from the superfluid ^{4}He, resembling a "gas" over the liquid. The key difference from the ordinary "evaporation", is that the diluted phase is thermodynamically stable at a fixed ^{3}He content down to a temperature of absolute zero, leading to a non-decreasing "vapor pressure", making the refrigeration process highly efficient. This dynamical equilibrium state allows to cool down samples to temperatures of the order of 20 mK. The mixing chamber (where the refrigeration is happening and the sample is located or thermally anchored to) is equipped with a heater allowing to thermally equilibriate the sample at any desired temperature ranging from the base to a couple of Kelwins.

Chapter 3

Anomalous Hall effect in $(V,Bi,Sb)_2Te_3$ - coexistence of surface and bulk ferromagnetism.

In this chapter I present detailed analysis of the AHE in our $(V,Bi,Sb)_2Te_3$ / $(Bi,Sb)_2Te_3$ hetero-structures, where we observe a rich AHE dependence on a variety of structural and experimental parameters, such as: magnetic doping level, magnetic layer thickness, temperature, and applied gate voltage. In all layers the Bi/Sb content ratio is aimed to be the same and close to 1:4. Table 3.1 summarizes the list of 14 devices labeled D1-14 analyzed in this chapter, where the layer stack arrangement and magnetic doping level are manipulated. Total TI layer stack thickness was aimed to be the same in all of the films, and ranges from approx. 7.5 to 10.5 nm. Parameters d_1-d_3 and n_1-n_3 denote thickness and percentage of V atoms (as a fraction of all atoms) in each of the layers (where the subscript numerates the layers in the TI stack starting from the bottom), and an entry of "-" indicates that the layer is not present in the hetero-structure. The x/y column shows the Hall bar dimensions for each of the investigated devices.

I begin with detailed analysis of the transport behavior in the device D1, due to the fact that it most clearly illustrates the rich nature of AHE in these samples. Afterwords I discuss the remaining devices D2-D14 where we manipulate the structural parameters in order to further investigate the observed unusual ferromagnetic behavior. Finally I comment on the alternative interpretation of "bump"-like magneto-transport behavior in the literature in this material (and other materials) involving magnetic skyrmion textures. The results from this chapter are published in the ref. [18].

	$\mathbf{d}_1$	$\mathbf{n}_1$	$\mathbf{d}_2$	$\mathbf{n}_2$	$\mathbf{d}_3$	$\mathbf{n}_3$	x/y
D1	2	6.5	7	0	-	-	200x600 μm^2
D2	6	0	2	6.5	-	-	200x600 μm^2
D3	3.5	0	4	6.5	-	-	10x30 μm^2
D4	6	0	2	4	-	-	10x30 μm^2
D5	2.5	0	6	6.5	-	-	10x30 μm^2
D6	7	0	3	2	-	-	10x30 μm^2
D7	10.5	6.5	-	-	-	-	200x600 μm^2
D8	9	1.5	-	-	-	-	200x600 μm^2
D9	3.5	0	2	6.5	3.5	0	10x30 μm^2
D10	2	6.5	7	0	-	-	10x30 μm^2
D11	2	6.5	4.5	0	2	6.5	10x30 μm^2
D12	2	6.5	6.5	0	2	4	200x600 μm^2
D13	2	6.5	4.5	0	2	4	200x600 μm^2
D14	10	2.7	-	-	-	-	10x30 μm^2

Table 3.1: Table presenting thicknesses and magnetic doping contents for individual layers in the heterostructure stack for all devices presented in this chapter (devices D1-D14). Parameters $d_{1,2,3}$ and $n_{1,2,3}$ denote thickness and percentage of V atoms (as a fraction of all atoms) in each of the layers (where the subscript numerates the layers in the TI stack starting from the bottom), and an entry of "-" indicates that the layer is not present in the hetero-structure. The x/y column shows the Hall bar dimensions for each of the investigated devices.

3.1 Two anomalous Hall components.

Fig. 3.1 shows Hall magneto-resistivity measurement collected at temperature 2.4 K and gate voltage 0 V from the device D1. As is visible in Fig, 3.1a, the hysteresis loop measurement is vertically off center (labeled in red). This is a result of an effective misalignment of Hall probes due to the fact that in a realistic experimental setting, the Hall voltage is never probed ideally perpendicular to the current flow direction. This is schematically depicted in Fig. 3.1 (vastly exaggerated), where in our samples due to the fact that the samples are patterned using precision lithography, the ratio describing this effective misalignment $\Delta x/L$ never exceeds 0.005.

In some of the samples the longitudinal voltage signal is 2-3 orders of magnitude larger than the Hall signal, therefore despite such small misalignment, the voltage pick-up is big enough to visibly vertically shift the hysteresis loop. In order to carefully analyze the AHE signal, this fraction $\Delta x/L$ of longitudinal signal is subtracted from the Hall signal, restoring the anti-symmetric properties. In addition the OHE background is subtracted as a linear

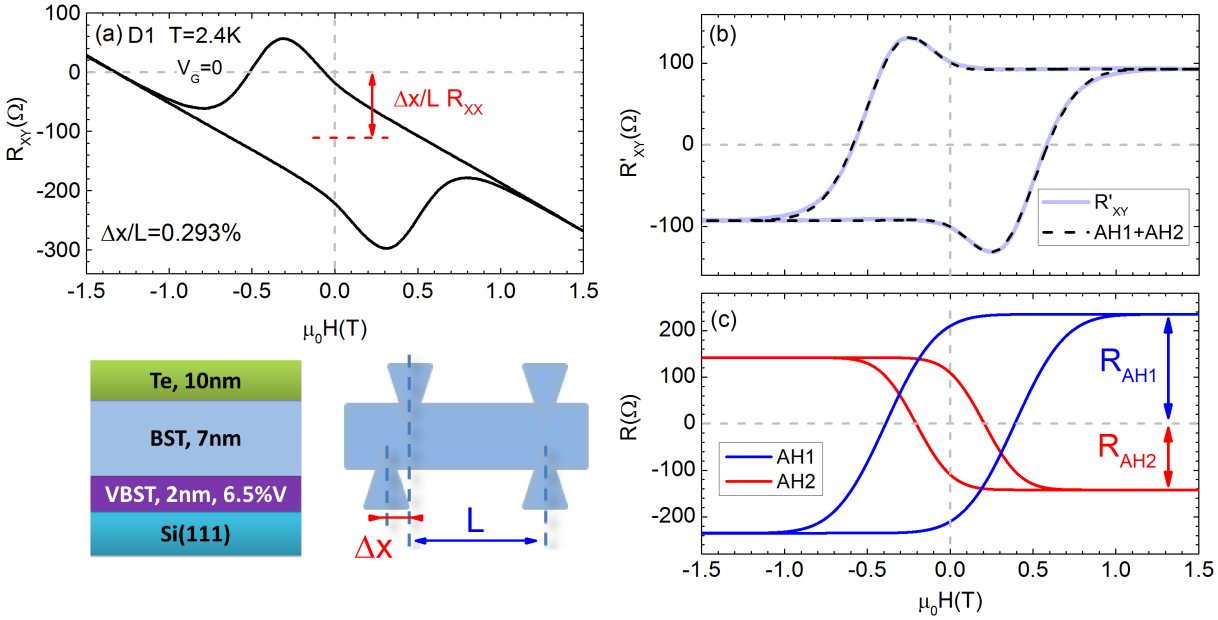

Figure 3.1: The double anomalous Hall model. a) Measurement of the Hall resistance as a function of H field for device D1 (layer schematic in the left bottom corner). The red arrow indicates the offset resulting from mixing of the longitudinal resistance (see text for details). b) Solid line: Same data after removing the offset and classical Hall contributions as described in the text. Dashed line: result of the two component model used to describe the data. c) each of the two anomalous Hall contributions extracted from fitting the data.

slope around H=0 (positive slope here corresponds to n-type transport). The resulting AHE signal is plotted in Fig. 3.1b, and it is apparent that the qualitative appearance of the curve differs from a typical ferromagnetic hysteresis loop. A clear "bump"-like feature develops close to magnetic field corresponding to the magnetization reversal events.

3.1.1 Details of the double anomalous Hall model.

It turns out that the AHE signal from Fig. 3.1b can be rather easily decomposed into two separate signals, each resembling an ordinary AHE hysteresis loop. Both components are plotted separately for clarity in Fig. 3.1c, and a sum of both components (the fit) is overlaid on the data in Fig. 3.1b, demonstrating a good agreement. Both fitted components follow a mathematical expression $R_{xy}=R_{AH}\mathrm{erf}(A(H-H_C))$, where R_{AH} is the AHE amplitude, A is the transition width, and H_C is the switching field defined as the field value when $R_{xy}=0$.

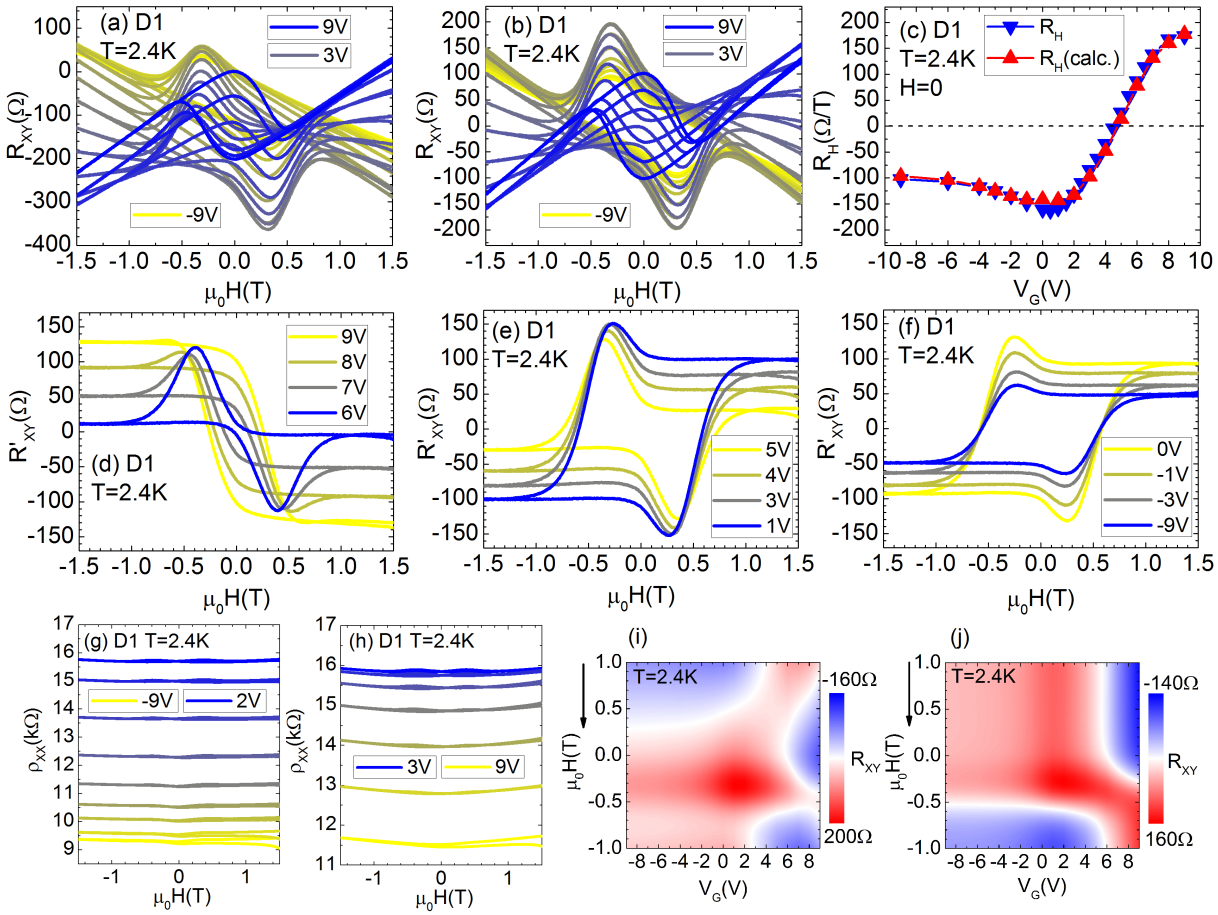

Figure 3.2: Data from device D1 collected at 2.4K. a) Raw Hall magneto-resistance for a full range of gate voltage values from V_G=-9 V (yellow line) to V_G=9 V (blue line). b) The same data set, after removal of the voltage crosstalk (color coding is the same). c) Subtracted ordinary Hall slope as a function of gate voltage (blue points), and the expected slope value (a consistency check) calculated from the fitting parameters obtained from the high field analysis later in the thesis (red points). d)-f) Sampling of the corrected Hall resistance magnetic field sweeps. g)-h) Raw longitudinal magneto-resistivity corresponding to the Hall data set. i) and j) show color maps of the Hall resistance magnetic field sweeps for a full range of investigated gate voltages, respectively before (i) and after (j) the ordinary Hall slope removal. Figure taken from [18].

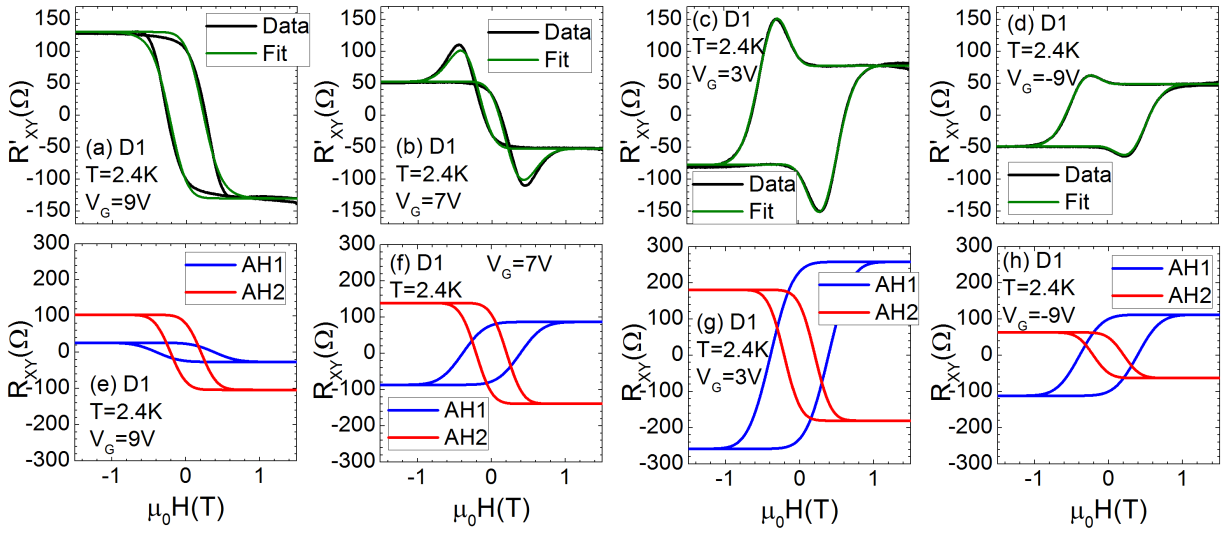

Figure 3.3: Sampling of Hall resistance magnetic field sweeps R'$_{xy}$ for different gate voltage values, collected from device D1 at 2.4 K. The black color represents the experimental data, and olive lines represent the simulated curves using the two component model. The two anomalous Hall contributions obtained from the fitting are plotted separately for clarity below, where the red color depicts the negative contribution, and the blue color shows the positive contribution.

3.1.2 Evolution of both components with gate voltage.

Our devices are equipped with a top gate, which allows for the analysis of the evolution of both components with gate voltage. Fig. 3.2a shows sampling of Hall magneto-resistance data from the same device D1 collected at temperature 2.4 K for a variety of gate voltage values. For further analysis, the longitudinal voltage crosstalk (Fig. 3.2b), and OHE slope (Fig. 3.2d-f) is subtracted. Value of the OHE slope subtracted from each sweep is plotted in Fig. 3.2c (blue color), compared to the zero-field OHE slope as calculated from the high magnetic field analysis later in the thesis, as a consistency test. Fig. 3.2g and h depict the corresponding longitudinal magneto-resistivity data (ρ_{XX}), and Fig. 3.2i and j represent the color plots of the data from Fig. 3.2a-f.

The same AHE decomposition is performed for all of the Hall magneto-resistance hysteresis loops, and sampling of that procedure is plotted in Fig. 3.3. Top row depicts the corrected R'$_{XY}$ data (black color) with overlaid double AHE fit (green color), bottom row shows two components separately for clarity. In all fits the coercive fields (H_{C1} and H_{C2}) and magnetic reversal widths (A_1 and A_2) from both contributions are fixed. In case of all of the sweeps the model describes the data very well, despite only two parameters (both AHE amplitudes) being used as fitting parameters for different magnetic field sweeps at

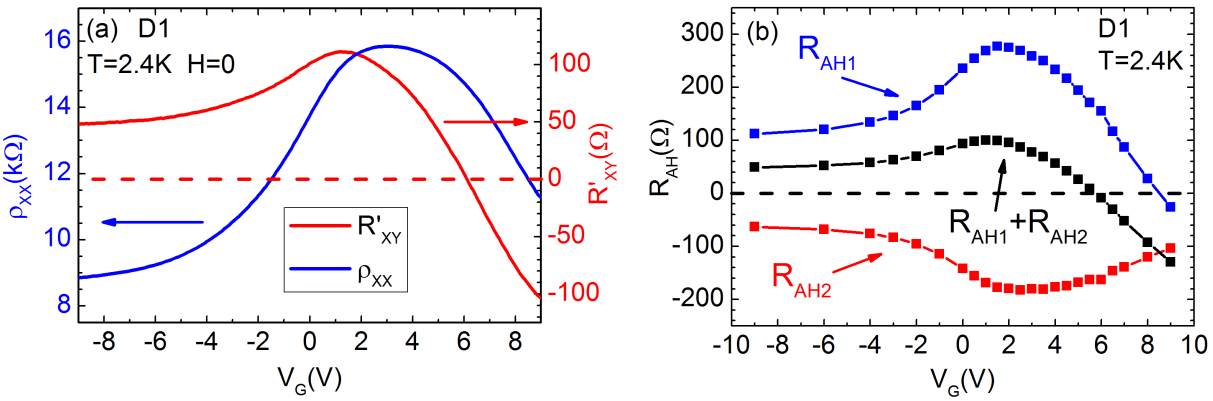

Figure 3.4: a) Zero-field ρ_{xx} and R'$_{xy}$ from the device D1 as a function of gate voltage. b) Strength of each of the contributions extracted from the magneto-resistance data (blue and red), as well as a sum of both components (black color), reproducing the total Hall signal depicted in (a) (red color).

different gate voltages.

Fig. 3.4a shows zero-field gate voltage dependence of the corrected Hall resistance R'$_{xy}$ and longitudinal film resistivity ρ_{xx}, demonstrating that the film can be electrostaticaly tuned through the minimum conductivity point. Moreover the total AHE signal changes sign when the gate voltage is changed to high positive values. Reason behind this sign tunability becomes apparent when the resulting AHE amplitudes of both components are analyzed. Fig. 3.4b shows the magnitude of the positive R$_{AH1}$ (blue points) and negative R$_{AH2}$ (red points) components as a function of applied gate voltage, with sum (black points) reproducing the overall sign reversal. This is a direct consequence of different gate dependence of both components, that individually do not change sign within the accessible gate voltage range. A single blue data point with negative value at gate voltage 9V is a fitting artifact, resulting from the fact that positive component becomes too small to reliably extract using the fitting (as can be seen in Fig. 3.3a).

Interestingly both positive and negative components experience a maximum that coincides with the maximum of film resistivity. However, as gate voltage is increased and the material is tuned towards the n-type regime, the positive component vanishes, while the negative in contrast remains clearly non-zero. The positive contribution depending considerably stronger on the applied gate voltage is not inconsistent with the hypothesis of surface and bulk origin of both ferromagnetic components, as will be discussed later in the thesis.

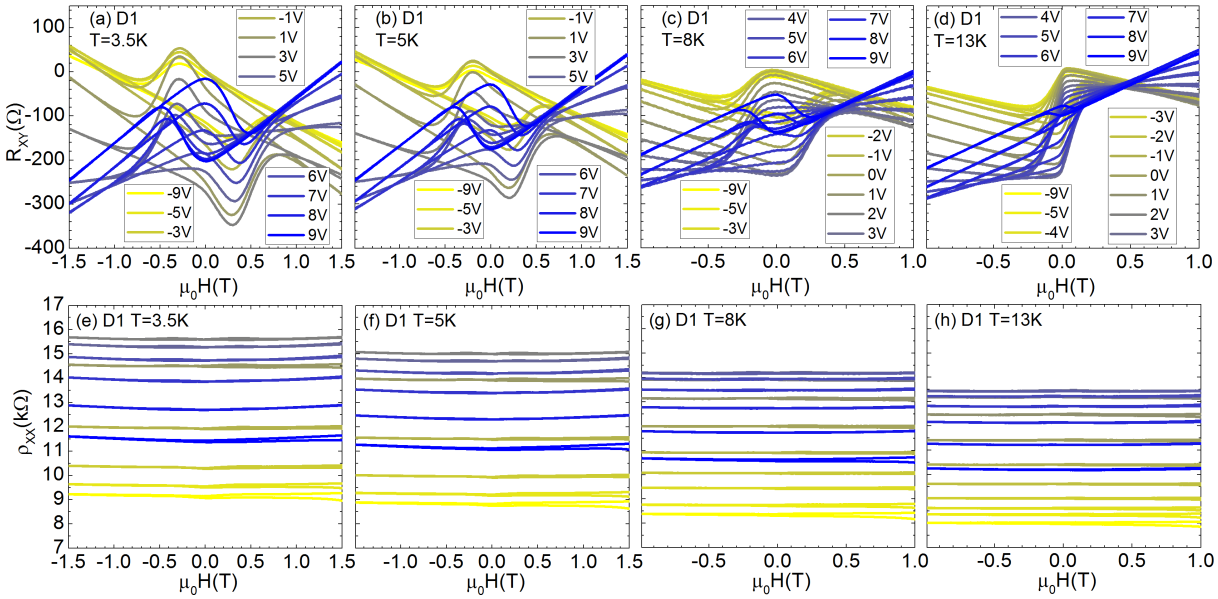

Figure 3.5: Experimental measurements from the device D1 collected at higher temperature values. Hall magneto-resistance is collected at the temperature 3.5 K (a), 5 K (b), 8 K (c), and 13 K (d), for a full range of gate voltage values. Below the corresponding ρ_{xx} data sets are plotted (e)-(h). Figure taken from [18].

3.1.3 Evolution of both components with temperature.

The next experimentally accessible parameter is the sample temperature. Fig. 3.5 shows magnetic field sweeps from the same device, collected for a wide range of gate voltages at elevated temperatures. To carefully analyze the AHE signal, the same longitudinal voltage pick-up and OHE linear slope removal is performed, and sampling of resulting corrected R'$_{xy}$ plots including the 2.4 K data is presented for clarity in Fig. 3.6, in form of a temperature/gate voltage matrix. One can see that the total AHE signal exhibits sign reversal not only with the gate voltage value, but also with the temperature.

This seemingly complicated behavior turns out to be rather easily analyzed employing the same two-component model. Summary of the analysis is presented in Fig. 3.7, where an overall AHE sign reversal with temperature is a consequence of both components exhibiting different temperature dependence. Negative contribution nearly vanishes at 13 K, whereas the positive one remains clearly non-zero at the same temperature. Both: different temperature evolution, and different coercive fields of both AHE components, suggests the distinct ferromagnetic origin.

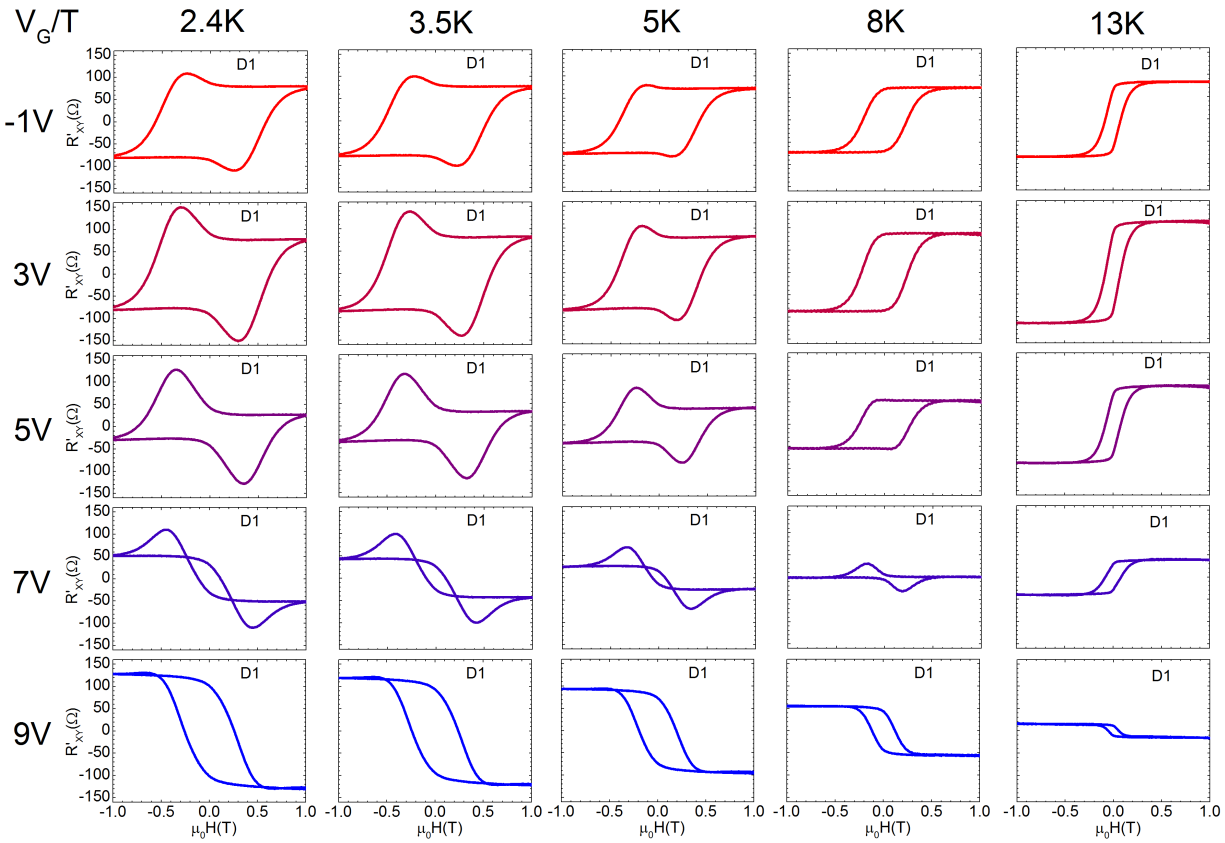

Figure 3.6: Sampling of R'$_{xy}$ evolution with the gate voltage and temperature for device D1. The columns represent the temperatures: 2.4 K, 3.5 K, 5 K, 8 K, and 13 K, and rows represent the gate voltage: -1V, 3V, 5V, 7V, and 9V. The range and values for both axis are the same in all figures. Figure taken from [18].

3.2 High magnetic field analysis and relation between the type of carriers contributing to transport and both anomalous Hall components.

A different gate voltage evolution of both AHE components, with a positive component vanishing at high positive gate voltages, suggests some relation to the type of carriers dominating the transport properties. In order to investigate that, in this section I present detailed high magnetic field analysis performed on the same device (D1) at temperature 2.4K, and directly compare the results to the individual AHE amplitudes obtained from the double AHE modeling.

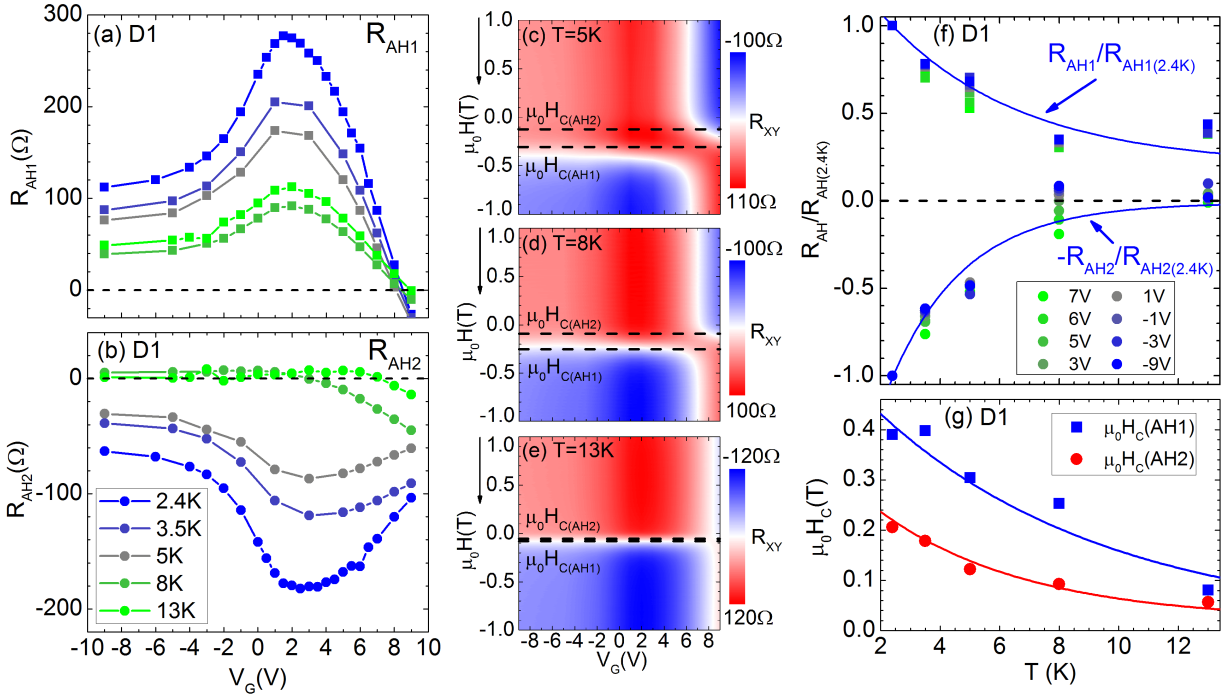

Figure 3.7: a)-b) gate voltage dependence of the positive/negative contribution for measurements at various temperatures. c)-e) Color plots of magnetic field sweeps of total AHE signal at 5K, 8K and 13K with dashed lines depicting the reversal fields of both components. f) Temperature dependence of each of the (normalized) components, and g) temperature dependence of the coercive field associated with each of the component. (The lines are guides to the eye.) Figure adapted from [18].

3.2.1 Details of the two carrier model.

In order to proceed with the multiple carrier analysis of the Hall effect, a pair of assumptions need to be made.

The first assumption is the magnetic field independence of the anomalous Hall effect, in comparison to the ordinary Hall magneto-resistance. Under this assumption the contribution from the AHE can be treated over the entire magnetic field range (at fields larger than the range corresponding to a hysteresis loop) as an offset equal to the sum of both AHE amplitudes, obtained from the low field fitting.

The second assumption is the external magnetic field being sufficiently large to dominate the internal magnetic field of the investigated system, thus satisfying the $B \approx \mu_0 H$ condition. Under these circumstances the total Hall resistance response of the system will be a sum of a constant offset caused by the AHE and the traditional multiple carrier type formula.

The formula for R_{XY} within the two carrier Hall effect model can be expressed as follows: $R_{XY} = (\omega B + \theta B^3)/(\epsilon + \zeta B^2)$, where $\omega = en_1\mu_1^2 + en_2\mu_2^2$, $\theta = en_1\mu_1^2\mu_2^2 + en_2\mu_1^2\mu_2^2$, $\epsilon = (en_1\mu_1 + en_2\mu_2)^2$, and $\zeta = \mu_1^2\mu_2^2(en_1 + en_2)^2$, where $n_{1/2}$ are the carrier densities and $\mu_{1/2}$ are the carrier mobilities. In this convention, the carrier density for holes is a negative number, and for electrons is positive.

Due to the absence of knowledge regarding the influence of magnetism and AHE on the longitudinal conductivity, a reliable ρ_{XX} fitting is not possible. Therefore instead of fitting both ρ_{XX} and R_{XY}, careful constraints need to be placed on the parameters in the R_{XY} fitting. The constraints also serve to correlate the R_{XY} curves collected at different gate voltages.

The first constraint pertains to the total amount of carriers in the system. Based on a simple capacitor picture, the magnetic TI sample behaves like one plate of a capacitor, with the other plate being the gate metal, both separated by a AlOx/HfOx dielectric layer stack. Therefore upon increasing the applied positive gate voltage, the total amount of carriers must increase monotonically.

In order to further reduce the parameter space, a second constraint is put in place. To correlate the curves at different gate voltages, the assumption is made that the total conductivity $\sigma_0 = en_1\mu_1 + en_2\mu_2$ is directly proportional to the experimentally measured zero-field σ_{XX} value, as the experimental σ_{XX} value includes the unknown effects from the magnetism. The magnitude of the proportionality constant affects the absolute values of the resulting fitting parameters, however the relevant trends between different parameters remain unaffected and can be qualitatively analyzed nonetheless. For the purpose of the following analysis, this constant is assumed to be 0.8.

3.2.2 Comparison between electron/hole transport parameters and amplitudes of surface and bulk anomalous Hall coefficients.

Summary of the high field analysis is presented in Fig. 3.8. The gate voltage sweeps are collected at different magnetic field values. The resulting data set is transposed in order to obtain the magnetic field dependence at different gate voltages, the Hall signal is corrected for the voltage pick-up, and the resulting data is plotted in the Fig. 3.8c and d (solid lines). Curves as obtained from the two carrier model fitting (dashed lines) are overlaid on the data, demonstrating a good agreement with the experiment. Fig. 3.8e-g shows

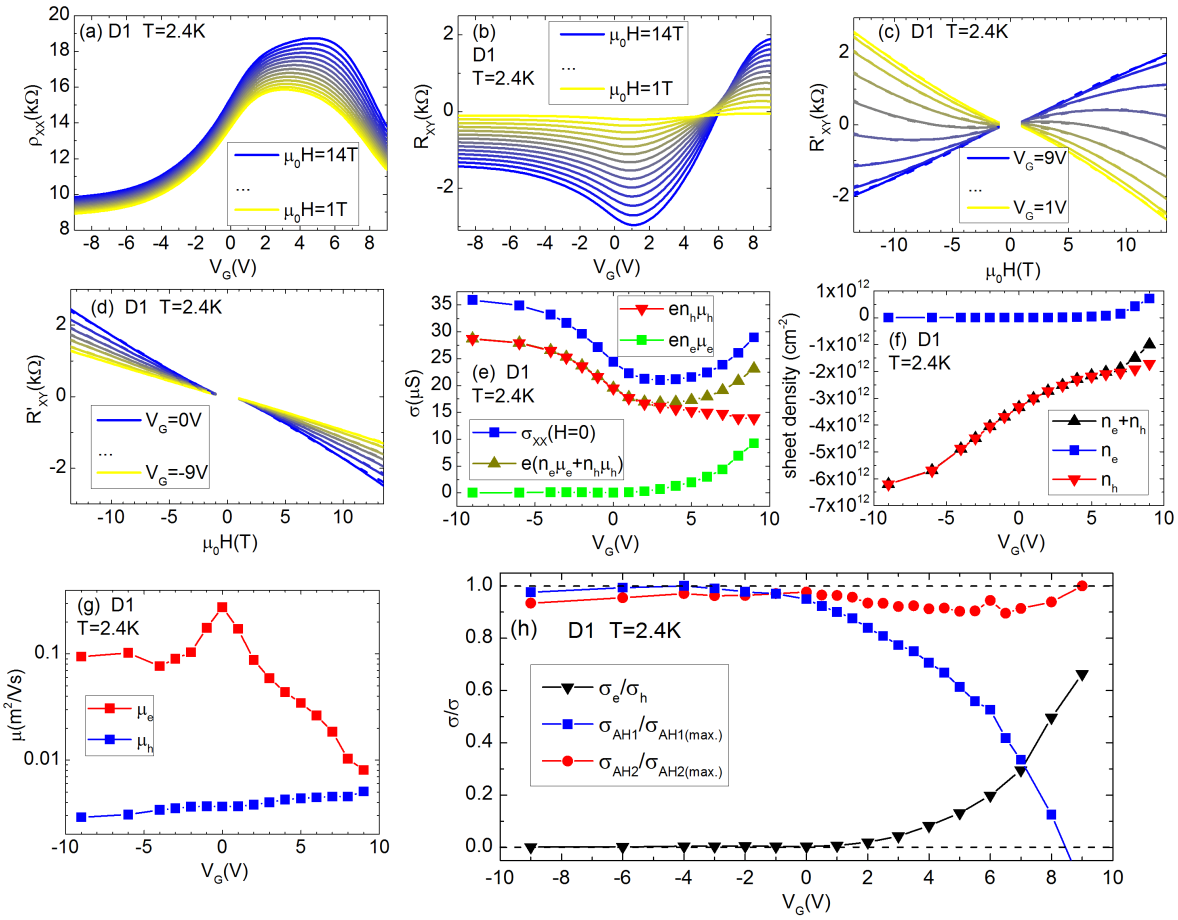

Figure 3.8: High magnetic field analysis of the device D1 collected at 2.4 K. Sampling of raw ρ_{xx} (a) and R_{xy} (b) gate voltage sweeps collected for fixed external magnetic field values ranging from μ_0H=14 T to μ_0H=1 T in intervals of 1 T. R'$_{xy}$ curves after the voltage crosstalk correction were plotted as a function of external magnetic field in (c) and (d). e) Conductivity of holes (red points), electrons (green points), as well as sum of electrons and holes conductivity (dark yellow). f) Black points show the total carrier density, blue and red points show the obtained sheet densities respectively for electrons and holes. g) Mobilities of electrons (red points) and holes (blue points). h) Comparison between the electrons/holes conductivity ratio and the normalized AH amplitudes from both ferromagnetic components. Figure adapted from [18].

the resulting parameters: electron and hole conductivities ($en_1\mu_1$ and $en_2\mu_2$), as well as electron and hole sheet densities (n_1 and n_2) and mobilities (μ_1 and μ_2). It is clear that in the high gate voltage regime the electron conductance switches on, consistently with the overall appearance of the change in slope in the Hall data.

As a consistency test, a zero field Hall slope is calculated from the obtained parameters using the two-carrier model (a magnetic field derivative of $R_{XY} = (\omega B + \theta B^3)/(\epsilon + \zeta B^2)$ at zero field gives $R_H(B = 0) = \omega/\epsilon$), and compared to slopes removed "by hand" in the low field analysis in Fig. 3.2c. This demonstrates the self-consistency of the analysis, and validates the linear slope subtraction in the low field limit used earlier in the analysis.

Fig. 3.8h shows a direct comparison of the AHE amplitudes to the type of carrier contributing to magneto-transport obtained from the two-carrier Hall fitting parameters, as a function of gate voltage. Blue (positive component) and red (negative component) data points represent the normalized anomalous Hall conductivities of both components, calculated using a matrix inversion method, where $\sigma_{AH1/2} = R_{AH1/2}/(R^2_{AH1/2} + \rho^2_{XX})$. The black points represent a ratio of electron and hole conductivity $\sigma_e/\sigma_h = (en_1\mu_1)/(en_2\mu_2)$. It is clear that the positive component (blue color) vanishes when electron conductivity switches on, whereas the negative (red color) component remains nearly gate voltage independent. The hypothesis of a positive component originating on the surface, and negative in the bulk of the material is consistent with this behavior, as one would expect the surface contribution to be electrostatically more affected by the top gating.

3.3 Anomalous Hall sign tunability with magnetic layer thickness and doping.

In order to gain more insight into the possible origin of both AHE components, a series of samples was characterized, where the layer stack structural parameters were varied. Fig. 3.9 depicts the Hall magneto-resistance data as collected from each of the devices D2-D14 (layer stack parameters are presented in the Table 3.1) at the temperature 4.2K and gate voltage providing the highest longitudinal resistivity ρ_{XX} for each device.

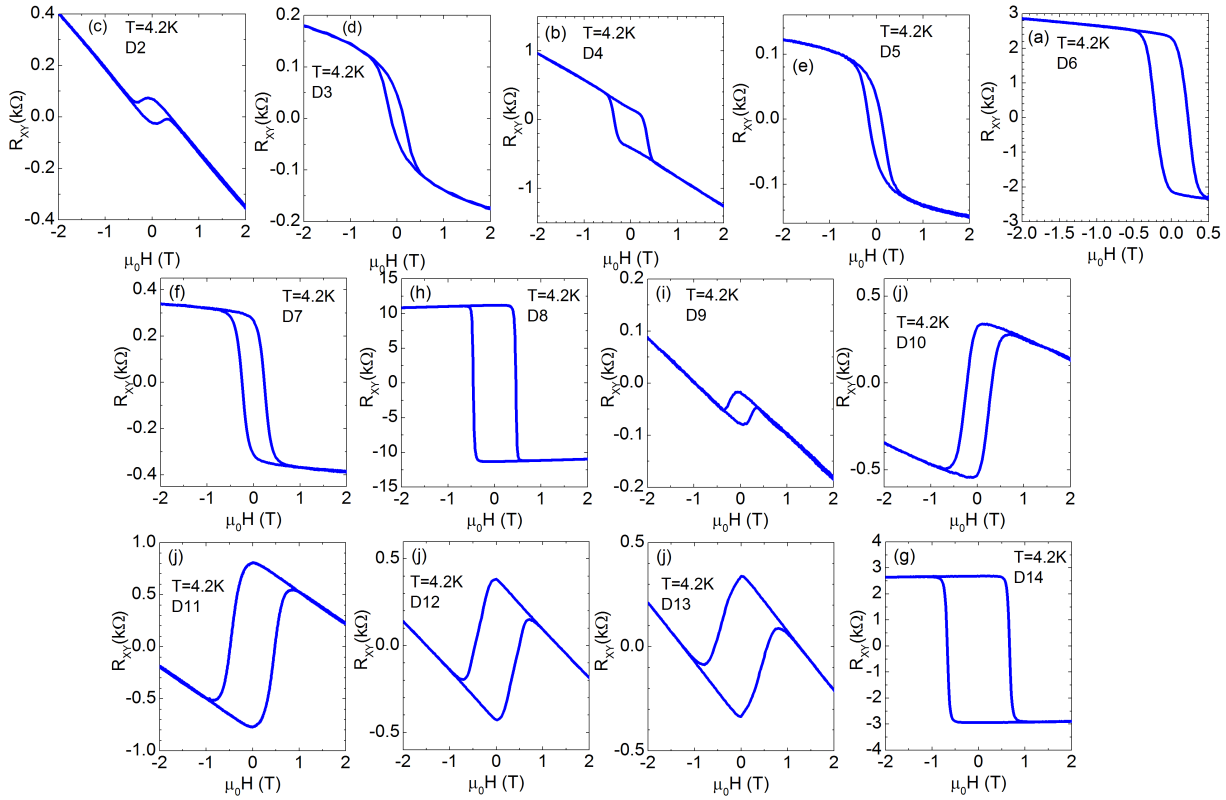

Figure 3.9: Hall magneto-resistance from devices D2-D14 collected at 4.2 K for the gate voltage providing the highest ρ_{xx} in each sample. Figure taken from [18].

First the devices D2-D8 are discussed where in a systematic way, the only two parameters varied between the samples are: the magnetic layer thickness, and magnetic doping level. For a clarity the layer stack for each of these devices is presented in the Fig. 3.10 on the top. Next, to analyze the AHE response, the data is corrected for an offset and the OHE background is removed. Fig. 3.10a shows the R'$_{xy}$ data for the devices D2-D4. It is clear that only some layers (for example the device D4) exhibit a clear "bump"-like AHE. This is likely a result of the fact that in order for this feature to be clearly visible, the AHE components need to be both: sufficiently strong, and have sufficiently different reversal fields. The amplitude and the reversal field of both components are likely affected by the layer interface conditions that can be different for different layer stacks. When any of these two criteria is violated, the total AHE response is either dominated by one of the two components, or the components are blurred together, resulting in a hysteresis loop that looks "normal". This affects the qualitative shape of the hysteresis loop for each of the samples, however the sum of both components (the value of a total AHE signal) remains a good indicator that can be further investigated.

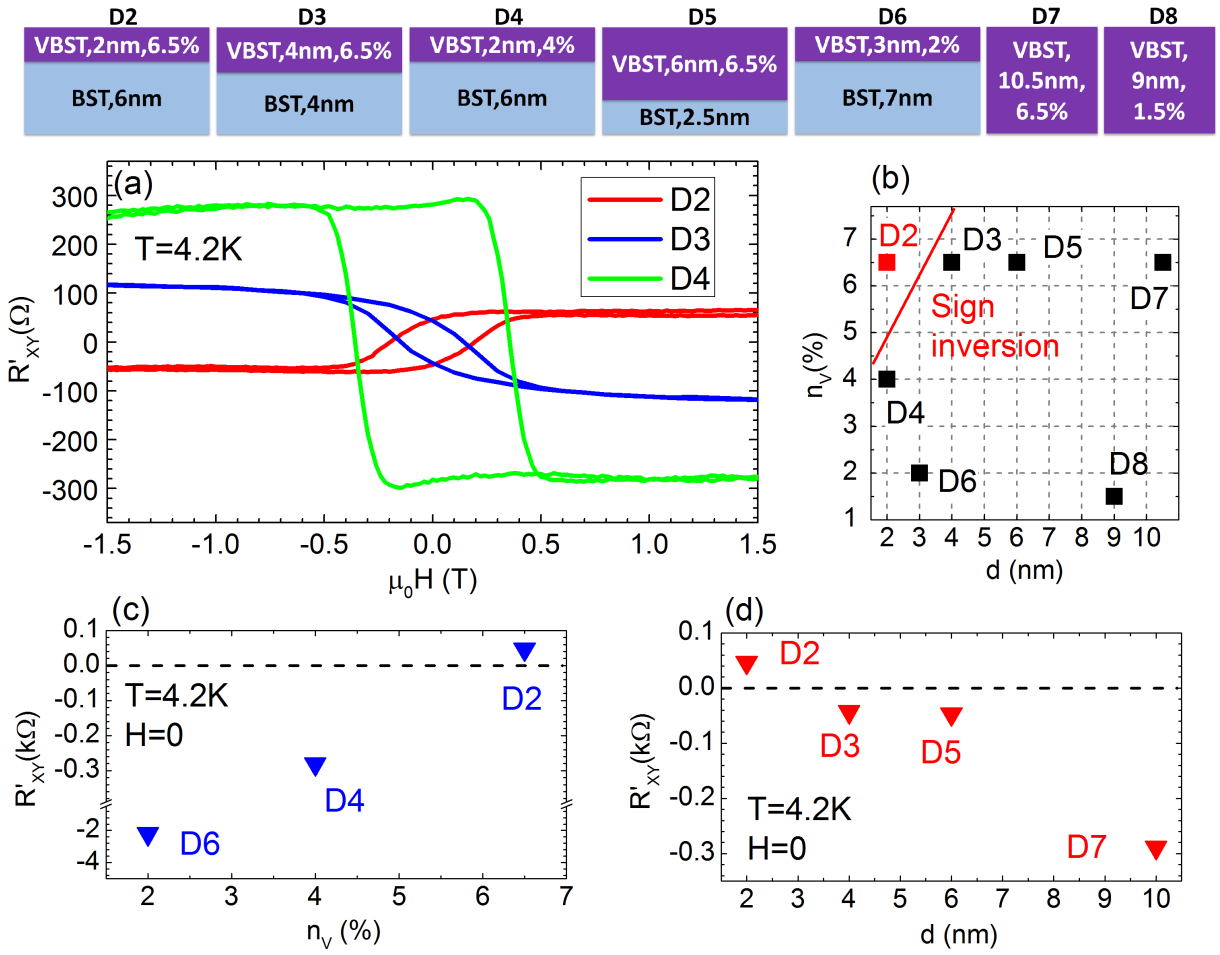

Figure 3.10: a) Magnetic field dependence of the offset corrected Hall resistance (R'$_{xy}$) for devices D2-D4. b) Magnetic doping / thickness phase space with position of the devices D2-D8. c)/d) Offset corrected zero field value of the Hall resistance as a function of magnetic doping level (c) and magnetic layer thickness (d) for the positively magnetized state. A schematic layer layout for devices D2-D8 is presented at the top of the figure. Figure taken from [18].

Interestingly when the magnetic doping level "n_V" (Fig. 3.10c), and magnetic layer thickness "d" (Fig. 3.10d) are varied, we observe the total AHE sign reversal, as a function of both of these parameters. For clarity the position of each of the devices (D2-D8) is plotted in the Fig. 3.10b as a thickness/doping space with a red line depicting where the sign reversal appears at 4.2 K. The device D8 represents where on this scale the material exhibiting the QAHE at lower temperatures is located.

For a fixed (high) magnetic doping level, when a magnetic layer thickness is increased (Fig. 3.10d), the total AHE signal goes from positive to negative. Based on that we

propose that the positive component originates on the surface of the TI film, whereas the negative in the bulk of the film. When for a fixed magnetic doping level the thickness is changed, the amount of magnetic dopants on the surface remains unaffected (as the two surfaces only shift with respect to each other), whereas the amount of the magnetic dopants in the bulk changes (as it scales with the volume), effectively tuning only one of the two components and leading to the total AHE sign change. This interpretation is still speculative at this point, and a deeper understanding with a microscopic model needs to be developed in the future.

The reproducibility of a (positively magnetized) positive value of the total AHE signal is visible in the data from the devices D9-D13 (Fig. 3.9i-j). Positive AHE sign is reproducible when the magnetic layer is "moved" from the top of the layer stack (D2), to the middle (D9), and to the bottom (D10), as well as when a magnetic tri-layer is formed with two magnetically doped layers separated by a non-magnetic layer (D11-D13).

3.4 Comments on the alternative interpretation in the literature tied to the magnetic skyrmion textures.

Phenomenology similar to those presented in this chapter involving the "bump" in the AHE signal was previously attributed in the literature to a topological Hall effect (magnetic skyrmion spin textures) [19, 42, 43, 44, 45, 46, 47, 48]. The main ambiguity surrounding the claims of magnetic skyrmions in these materials is the absence of direct imaging of the skyrmion spin textures. A complicated AHE response, which is not a direct way to probe the magnetic spin textures, is then potentially over interpreted as novel physics by means of unsubstantiated arguments. Moreover these reports are struggling to explain the complicated AHE sign reversal behavior, leading to even more speculative discussion. Our interpretation on the other hand provides an extremely simple explanation for every magneto-transport feature observed in transport experiments, including the dependence on magnetic field, temperature, gate voltage, as well as structural parameters such as layer thickness, and magnetic doping level [18], without the need to speculate about the new exotic physics.

Chapter 4

Quantum anomalous Hall effect in $(V,Bi,Sb)_2Te_3$.

In this chapter I present our results demonstrating a perfectly quantized QAHE transport in $(V,Bi,Sb)_2Te_3$ layers. Afterward I discuss the experimental evidence that quantum anomalous Hall chiral edge channels survive at temperature range vastly exceeding the regime where quantization is directly visible in the experiment. The development of a multi-terminal Corbino geometry allows to probe non-local signals that can only originate from the chiral edge channel transport, and such non-local signals exist as long as the bulk of the material remains ferromagnetic. The results from this chapter are published in the refs. [28, 39, 12, 49, 50, 51].

4.1 Perfect electronic transport quantization in the $(V,Bi,Sb)_2Te_3$ material.

4.1.1 Stoichiometry optimization of the $(V,Bi,Sb)_2Te_3$ material.

Electronic transport properties of the $V_y(Bi_{1-x}Sb_x)_{2-y}Te_3$ material are very sensitive to changes in the material composition. Both: group 5 elements ratio "x", and magnetic doping level "y" must be carefully optimized in order to maximize the AH response and achieve a perfect quantization at mK temperatures.

Fig. 4.1 shows magneto-transport analysis of $V_{0.1}(Bi_{1-x}Sb_x)_{1.9}Te_3$ films with fixed magnetic doping level (approx. 2 % of all atoms) and film thickness (approx. 9 nm). The varied parameter is Sb content "x". It is clear in Fig. 4.1c that there is a relatively

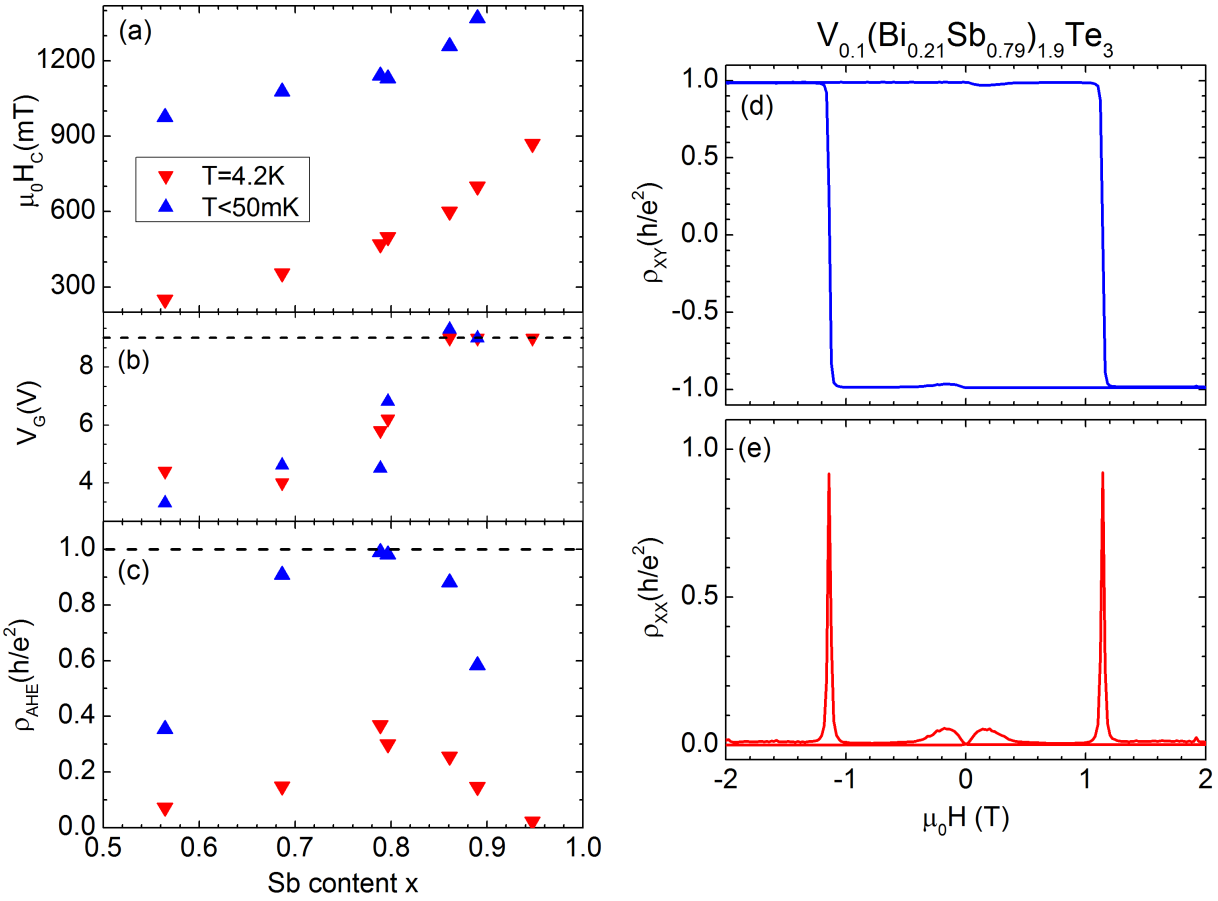

Figure 4.1: Sb content x dependence of: a) Coercive field, b) Gate voltage corresponding to a maximum Hall signal, and c) AHE amplitude. Blue color represents base temperature of the dilution refrigerator, and red color 4.2 K. Magneto-resistivity data demonstrating a perfect QAHE at 15 mK in an optimized 9 nm thick $V_{0.1}(Bi_{0.21}Sb_{0.79})_{1.9}Te_3$ film: d) Hall resistivity, and e) longitudinal resistivity.

narrow doping range where the AH resistance is large enough (around x=0.8) to reach a quantized value of h/e^2 at base temperature of the dilution refrigerator. Interestingly in Fig 4.1a one can see that the coercive field of the film is strongly dependent on the Sb content, reason for which remains an open question. Sb content dependence of the gate voltage corresponding to a maximum of Hall signal is plotted in Fig. 4.1b, and implies that increase of the Sb content makes the material electrically more p-type, as larger positive gate voltage needs to be applied to reach the charge neutrality. This gate voltage trend is consistent with Bi_2Te_3, and Sb_2Te_3 growing intrinsically n-type, and p-type respectively, and alloying both materials allows to smoothly transition between both limits [52].

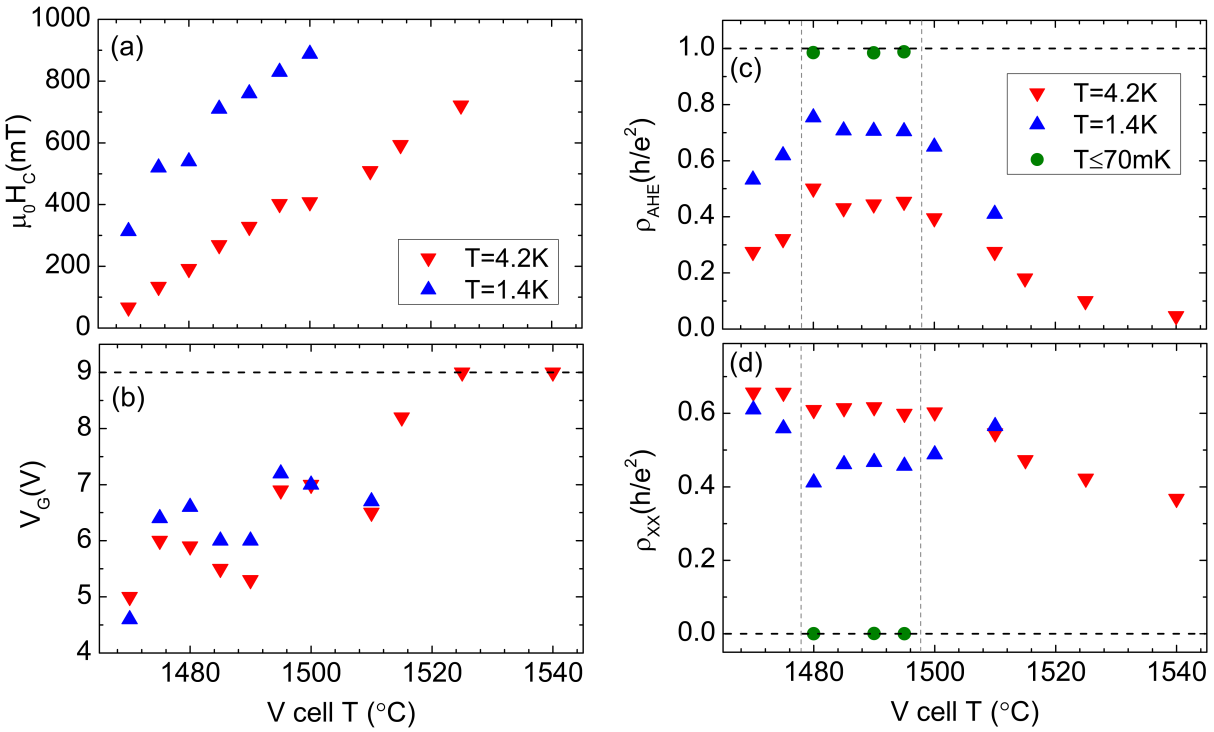

Figure 4.2: Variation of the V cell temperature during the MBE growth (and as a result the V doping level "y"). a) Coercive field, b) gate voltage for a maximum Hall signal, c) AHE amplitude, and d) longitudinal resistivity. Blue color represents the temperature 1.4 K, red color 4.2 K, and olive color a temperature below 70 mK. Horizontal dashed line in (b) represents the typical gate dielectric breakdown voltage in our samples, and vertical dashed lines in (c) and (d) represent the optimal growth window, where y is approx. 0.1. Three of the samples in the window were verified to exhibit the QAHE at base temperature of a dilution refrigerator.

Fig. 4.1d and 4.1e shows magneto-resistivity data for a $V_{0.1}(Bi_{0.21}Sb_{0.79})_{1.9}Te_3$ film at base temperature of the dilution refrigerator, and gate voltage corresponding to quantized AH resistance. The Hall resistivity (ρ_{XY}) follows a rectangular-shaped hysteresis loop with a well defined plateaus at +h/e^2 or -h/e^2 depending on the magnetization direction in the system (which determines the chirality in the system), whereas the longitudinal resistivity (ρ_{XX}) vanishes, with exception of the Schubnikow de Haas peaks at the coercivity. The "bump"-like features in ρ_{XX} (also visible in ρ_{XY}) around H=0 most likely result from superparamagnetism in the material [15].

Another free parameter relevant in the growth optimization of these films is the V doping level. Fig. 4.2 shows a summary of magneto-transport results from a series of $V_y(Bi_{0.2}Sb_{0.8})_{2-y}Te_3$ samples. A wide range of samples is investigated where the V cell

temperature during the MBE growth is systematically varied, determining the final magnetic doping level. The results are plotted as a function of the V cell temperature, where the marked region (vertical dashed lines in Fig. 4.2c and d) represents a regime where "y" value is estimated to be 0.1 and perfect electronic transport quantization is observed.

Similarly to the Sb doping level series, one can see that change in the V doping has a specific range where transport properties are optimal for electronic quantization at base temperature of a dilution refrigerator. Three of the samples in the dashed region were verified to exhibit the QAHE below 70 mK (olive color).

Interestingly the coercive field and optimal gate voltage values reveal similar trends to the Sb doping series. Larger V doping level results in an increase of the ferromagnet switching field. At the same time there is a clear shift in the charge neutrality point, gate voltage needed to tune the system to a point of maximum AHE signal increases with V doping, implying that incorporation of vanadium atoms is not electrically neutral, and dopes the system with holes.

4.1.2 Metrologically comprehensive precision measurement of the zero field quantization of AHE.

A possibility to achieve a perfect electronic transport quantization without any external magnetic field turns out to be potentially useful in the context of the recent redefinition of the SI unit system, where for the first time all 7 base units are defined based on fundamental constants of nature. This redefinition constitutes a realization of ideas envisioned by Maxwell, and Planck [53], of a truly universal system of units. To quote Max Planck (1900) [53] (translated from German): "with the help of fundamental constants we have the possibility of establishing units of length, time, mass and temperature, which necessarily retain their significance for all cultures, even unearthly and non-human ones."

The biggest change pertains to redefinition of the Kilogram, where people moved away from a physical Kilogram artifact (a platinum-iridium alloy cylinder) as a definition, and now the base unit of mass is defined based on the Planck constant, which as far as the modern physics tells us, is truly universal.

In order for this new definition to work in practice, one needs an experimental (and preferably an easily accessible) way to trace the definition of Kilogram to the Planck constant. One of the ideas to achieve that is the electro-mechanical Kibble (or Watt) balance [10, 11], where the Kilogram can be mechanically "weighed" in terms of an electric response, due to the clever balance design.

The experiment is based on a simultaneous access to the Planck constant (h) and the elementary charge (e). This is possible by combination of the quantum voltage standard and the quantum resistance standard into a single experiment. The fundamental constants associated with both quantum standards are related to the Planck constant and the elementary charge in the following way: $R_K=h/e^2$ and $K_J=2e/h$, where R_K is the von-Klitzing constant (the quantum resistance) and K_J is the Josephson constant (the quantum voltage). Therefore the simultaneous experimental determination of R_K and K_J gives simultaneous access to h and e.

The operation of both quantum standards as a single instrument turns out to pose a big challenge. The quantum voltage is based on the AC Josephson effect [8, 9], whereas traditionally the quantum resistance is based on the integer QHE [4]. This leads to a rather obvious complication, as the QHE requires high external magnetic fields to operate, fields that make the quantum voltage standard impossible to work. For that reason the QAHE sparked some interest in the metrological community, as potentially the same transport properties as that of the QHE standard could be realized in a magnetic TI, without any external magnetic field.

The biggest obstacle turns out to be a temperature at which one can observe perfectly quantized transport properties, which limits the perfect QAHE to base temperature of a dilution refrigerator [12, 13]. A reason behind such ultra-low temperature breakdown of transport quantization will be discussed later in the thesis, and is related to the thermally activated bulk conductance. In order for the standard to be commercially viable, one would have to elevate the operational temperature to at least 1.4 K (and ideally 4.2 K), which both: is easily experimentally achieved in a simple ^{4}He cryostat, and is a temperature at which the Josephson quantum voltage standard operates comfortably. Nevertheless an experimental demonstration of the metrological precision of zero field transport quantization using proper metrological tools at 25 mK is a great first step towards achieving that goal.

Fig. 4.3 shows schematically a setup used in collaboration with Physikalisch Technische Bundesanstalt (PTB), to metrologically determine the precision of quantization in our magnetic TI sample. A standard Hall bar device patterned from our 9 nm thick $V_{0.1}(Bi_{0.21}Sb_{0.79})_{1.9}Te_3$ film (the same device as the data plotted in Fig. 4.1d and e) was placed in a dilution refrigerator with base temperature of 25 mK. A traveling cryogenic current comparator (CCC) bridge custom designed by our partners from PTB [54, 55] was located right next to the dilution refrigerator in our lab in Würzburg, and submerged in a liquid ^{4}He devar, providing a temperature 4.2 K. A CCC probe allows for extremely precise

comparison of magnitude of two currents. This in turn allows one to precisely compare the value of Hall resistance of the sample to a standard calibrated resistance.

As visible schematically in the Fig. 4.3, in a CCC probe, the wiring carrying both currents is winded inside a superconducting (SC) shield. Winding numbers are depicted in the figure (N_1 and N_2), with a ratio R_k/R_{ref} (where R_k is a von-Klitzing constant, and R_{ref} is a calibrated reference 100 Ω resistance) providing a value that is intentionally between N_1/N_2 and $(N_1+N_A)/N_2$, where a value of N_A can be effectively tuned by changing the current flowing through the N_A coil. Both currents (from N_1+N_A and from N_2) flow in the opposite direction inside the SC shield, and a difference between both currents induces a screening current in the superconductor. This screening current in turn induces a magnetic flux that is measured with a superconducting quantum interference device (SQUID) magnetometer.

A traveling 100 Ω reference resistor was metrologically calibrated to a GaAs QH resistance standard in PTB Braunschweig before, as well as after the measurement campaign in Würzburg. A calibration before and after allows for interpolation of the reference resistance value during the time of experiment. Fig. 4.4 shows a calibration of the traveling resistor against a GaAs quantum resistance standard, performed at different dates in PTB facilities (as visible on the axis). A dashed line fit shows a linear drift in value of the resistor and allows for obtaining a value during the experiments on a magnetic TI sample. Grey regions represent the times when a standard resistor was transported between the facilities in Braunschweig and Würzburg.

We have placed a conservative estimate for the value of a relative uncertainty on the reference resistance value of 0.2 ppm, which is an order of magnitude higher than a typical uncertainty level (well below 0.05 ppm) when compared to a GaAs standard. A reference resistor is kept inside a thermostat for temperature stability at 23.1±0.05 degree centigrade (corresponding to a relative uncertainty of 0.02 ppm in this control range). The use of a traveling metrologically calibrated reference resistor is considered as a metrologically comprehensive method in the metrological community. A direct comparison between a magnetic TI sample and a GaAs quantum standard is in plans for the future experiments.

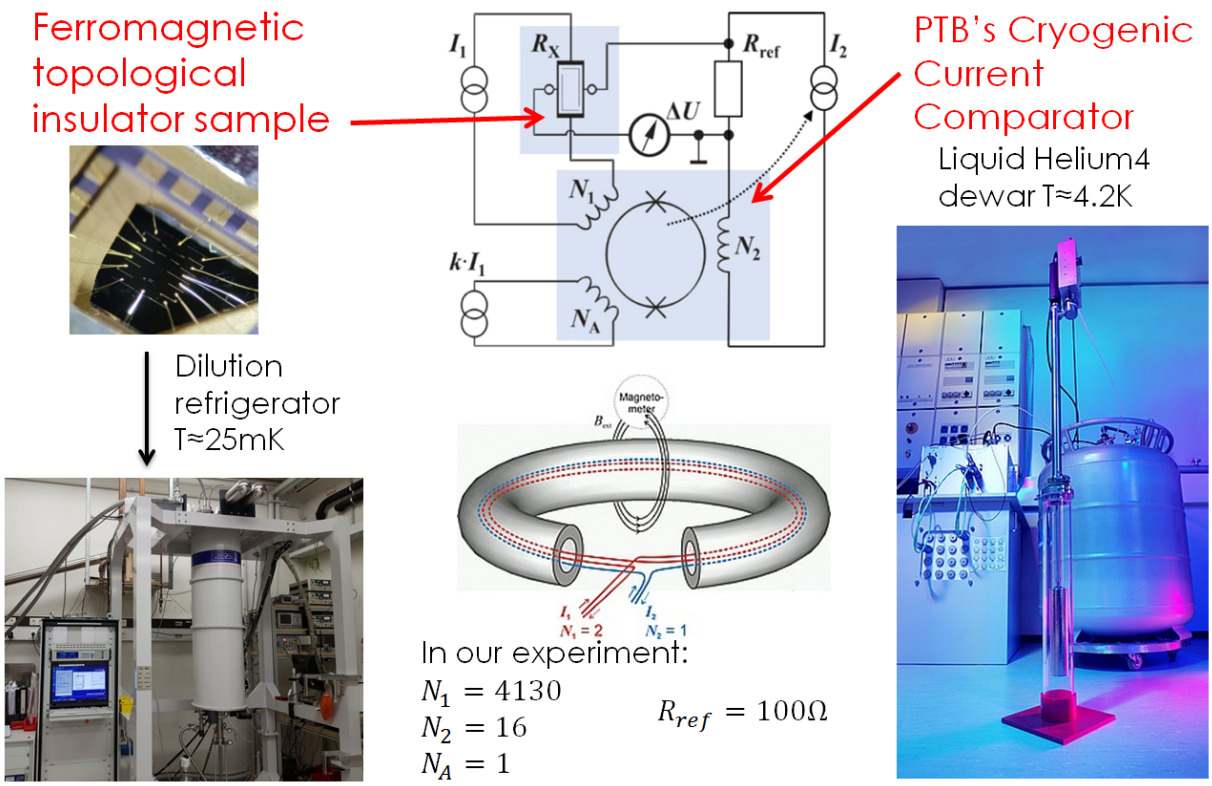

Figure 4.3: Schematic summarizing the experimental setup for a metrologically comprehensive precision measurement of the AH resistance quantization in our magnetic TI $V_{0.1}(Bi_{0.21}Sb_{0.79})_{1.9}Te_3$ sample. A ferromagnetic TI sample (left upper corner) is placed in a dilution refrigerator (left bottom corner). A Cryogenic Current Comparator probe is submerged in liquid ^{4}He in a devar located next to the dilution refrigerator (right).

Fig. 4.5 shows a resulting relative deviation of traverse resistance from quantization as a function of the applied current at 25 mK, zero external magnetic field (in the magnetized state), and gate voltage tuned into the quantized plateau. This allows for an extrapolation to zero current. A blue dashed line represents a power law fit in the form $a+b(I/nA)^c$, with a=(0.35±0.10)ppm and c=3.02±0.20. Interestingly the exponent "c" equal to 3 is consistent with similar experiments performed on the integer quantum Hall effect [56] and fractional quantum Hall effect [55]. The uncertainty of the zero field deviation a=(0.35±0.10)ppm obtained from fitting in the Fig.4.5 is the type-A uncertainty only, to which the remaining type-B uncertainty contributions from the uncertainty budget (see the ref. [12] for a full uncertainty budget) must be added, resulting in $\Delta R_H/R_K = (0.35 \pm 0.22)ppm$, where R_K is a von-Klitzing constant.

An estimated value of the longitudinal resistance can be obtained from the same kind of measurements with a CCC probe. In addition to the Hall signal, the diagonal signal

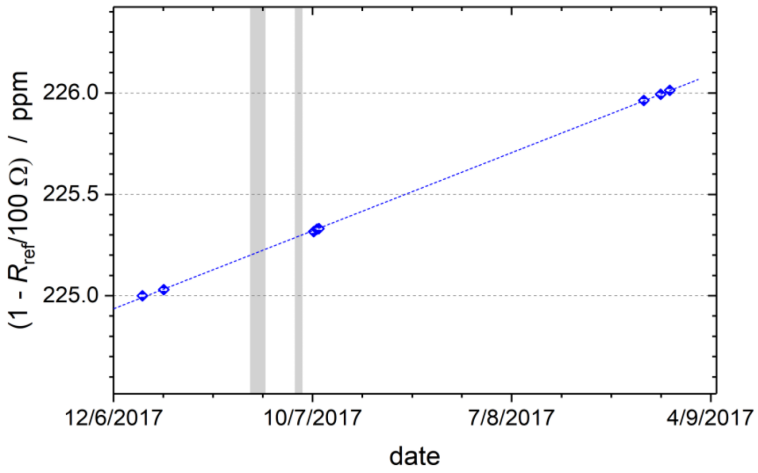

Figure 4.4: Drift behavior of the traveling resistance standard around the time of measurement. The calibration values have uncertainties smaller than the blue symbols. The grey areas depict the times when the resistor was traveling, before and after the measurement campaign. Figure taken from [12].

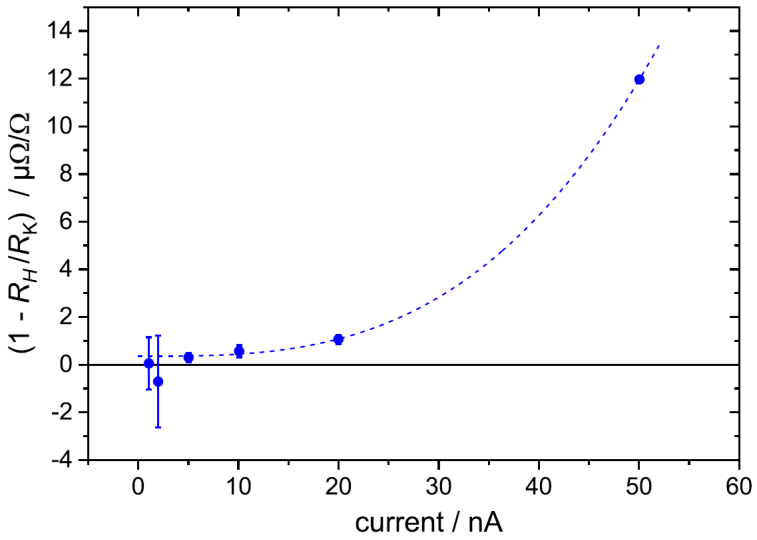

Figure 4.5: Relative deviation of the measured Hall resistance from the von-Klitzing constant (R_K) as a function of current. Measurements were performed with a sample at 25 mK, zero external magnetic field, and gate voltage tuned into the quantized plateu. A blue dashed line represents a power law fit in the form $a + b(I/nA)^c$, with a=(0.35±0.10)ppm and c=3.02±0.20. Figure adapted from [12].

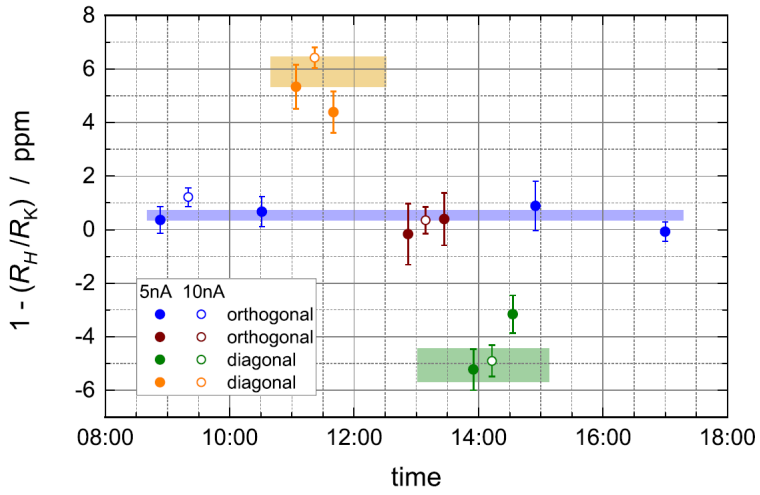

Figure 4.6: Series of measurements of traverse signal (1-R_H/R_K), as well as the diagonal signal (which is a sum of Hall and longitudinal signals). Measurements are performed at 25 mK, zero external magnetic field, gate voltage tuned into the quantized plateau, and with currents of 5 nA and 10 nA. Four different colors represent two diagonal and two traverse measurements (as a six-terminal Hall bar was investigated with two side contacts on each side). The colored rectangles represent the weighted average and standard deviation of the traverse and diagonal groups of data points. Figure taken from [12].

is measured, which provides a sum of Hall and longitudinal resistances (and therefore a difference between the two signals gives a measure of the longitudinal resistance). In Fig. 4.6 such measurements were performed at current values of 5 and 10 nA. Then a difference between the diagonal and traverse values was calculated. From that the longitudinal resistance was determined to be 5.5±1.5 ppm of R_K, which in turn results in the longitudinal resistivity (ρ_{XX}) of 1.83±0.5 ppm of R_K for the given (3/1) Hall bar aspect ratio.

In order to obtain the final relative deviation from quantization of Hall resistance, the geometrical factor resulting from finite voltage contact width needs to be included in the analysis. Due to the fact that Hall bar width is 200 μm and the voltage contact width is 20 μm, the geometrical factor is estimated to be s=-0.1. After assumption of a relative uncertainty for "s" to be 100 %, and including a factor of $-s\rho_{XX}$ to the earlier obtained $\Delta R_H/R_K$ value, a relative deviation from quantization of Hall resistance in our magnetic topological insulator layer at zero external magnetic field is $1 - R_{XY}/R_K = 1-(R_H - s\rho_{XX})/R_K = (0.17 \pm 0.25)ppm$, i.e., there is no deviation of R_{XY} from a perfectly quantized value within 0.7σ (standard measurement uncertainty). This value remains a world record for the precision of zero-field Hall resistance quantization to date.

For more technical details the reader is referred to the ref. [12] where the above results

are published and discussed in more detail.

4.2 Quantum anomalous Hall edge channels survive up to the Curie temperature in a magnetic topological insulator.

One of the requirements towards a commercially viable zero-field quantum resistance standard based on the QAHE is the increase of the operational temperature. So far the metrologically comprehensive experiments demonstrating a zero field quantization of Hall resistance in such magnetic TI layers remain limited to temperature of the order of 30 mK [12, 13]. The same layers have bulk ferromagnetism Curie temperature close to 20 K [7, 14].

When temperature is increased, the Hall resistance quickly deviates from a quantized value, and in the temperature range where one needs to achieve a perfect quantization at zero field for applications, around 4.2 K, it takes value clearly below h/e^2. Based on traditional measurements of Hall resistance in a Hall bar geometry it is not even clear if the chiral edge channel still exists in the sample, as due to a uniform current distribution in the device it is impossible to clearly separate the edge channel contribution from the ordinary bulk AHE.

This problem is resolved by implementation of a multi-terminal Corbino geometry, where non-local voltage signals allow for a clear separation of the edge channel and bulk current contributions, thus revealing a clear evidence for chiral edge channel transport up to Curie temperature (T_C) of bulk ferromagnetism.

4.2.1 The multi-terminal Corbino geometry.

Fig. 4.7 shows images from the lithography process, depicting the experimental geometry. The multi-terminal Corbino geometry contains 4 contacts on the inner edge and 4 contacts on the outer edge. This allows for four-terminal measurements along the same edge in the perfectly quantized state, as well as a traditional Corbino-like measurement between the two edges, giving a direct measurement of bulk resistivity. Most importantly however, this geometry allows for a non-local measurement scheme involving both edges, where the existence of quantum anomalous Hall chiral edge channel can indeed be verified well above the quantization temperature.

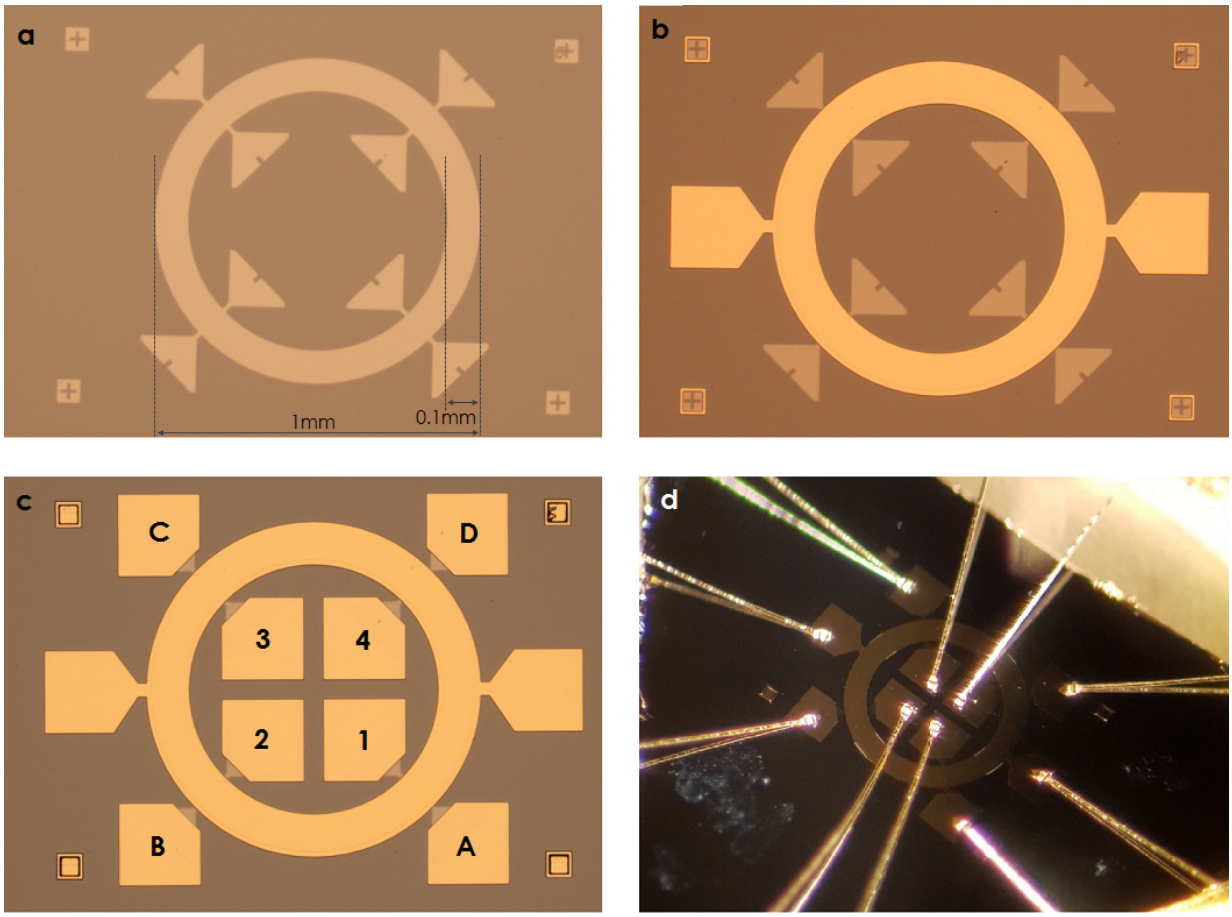

Figure 4.7: Optical microscope images from the lithographic process: a) patterned mesa with labeled relevant size scales, b) gate electrode, and c) ohmic contacts with labels on the inner edge (1-4) and the outer edge (A-D). d) Photograph of the device glued to a chip carrier with mechanically bonded contact wires.

4.2.2 Estimate of the bulk resistivity and perfect quantization at low temperatures.

First a two-terminal conductance between the two edges of the Corbino is analyzed as a function of gate voltage at temperature 25 mK and at zero field (in a magnetized state). This is presented in Fig. 4.8a. A bias voltage is applied to contact A, and contact 1 is grounded, and a current is measured with a series 10 kΩ reference resistor. When gate bias is tuned into the plateau regime (with a center around +5V), a flowing current measured on the series resistor vanishes, and therefore the conductance vanishes. As in this experimental setting there is no physical edge connecting contacts A and 1, an open circuit is indeed expected if the bulk between the two edge channels is truly insulating.

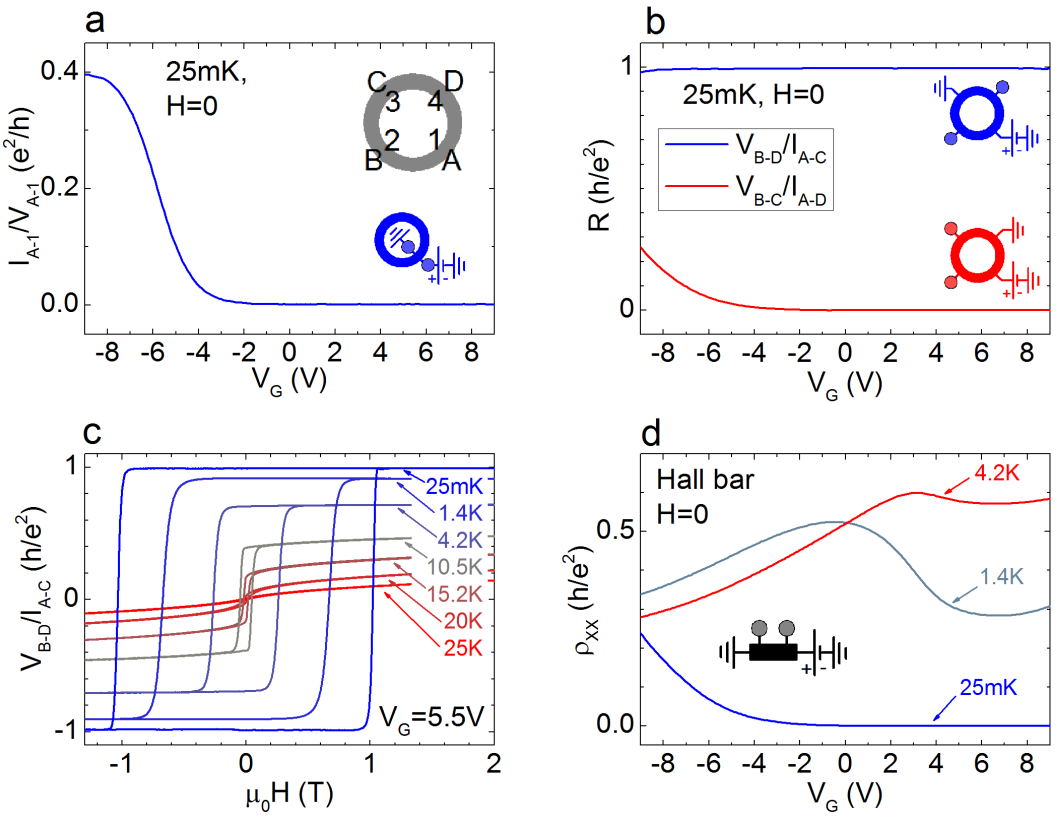

Figure 4.8: a) A base temperature two-terminal conductance gate sweep measurement between contacts A and 1 (between the two edges). b) Four terminal measurements on the outer edge, at base temperature, showing perfect dissipationless chiral edge channel transport. c) External magnetic field hysteresis loop of V_{B-D}/I_{A-C} for temperatures ranging from 25 mK to 25 K. d) Longitudinal resistivity measurements collected from an ordinary Hall bar device (with width of 200 μm and aspect ratio 3:1), patterned from the same MBE layer as the Corbino.

The existence of chiral edge channels is evident when four-terminal measurements are performed along a single edge of the Corbino. Fig. 4.8b shows the V_{B-D}/I_{A-C} (blue curve) and V_{B-C}/I_{A-D} (red curve) four-terminal signals as a function of gate voltage at zero magnetic field and 25 mK, where V_{B-D}/I_{A-C} reaches a quantized value of h/e^2, and V_{B-C}/I_{A-D} vanishes. These two configurations provide results equivalent to R_{XY} and R_{XX} in a traditional Hall bar exhibiting the QAHE.

When the out of plane external magnetic field is manipulated, the V_{B-D}/I_{A-C} signal (Fig. 4.8c) follows very well the behavior of R_{XY} in a Hall bar, where at 25 mK (blue curve) the data has a rectangular-shaped hysteresis loop demonstrating a switching between the two perfectly quantized states ($\pm h/e^2$). When the temperature is increased, the zero field

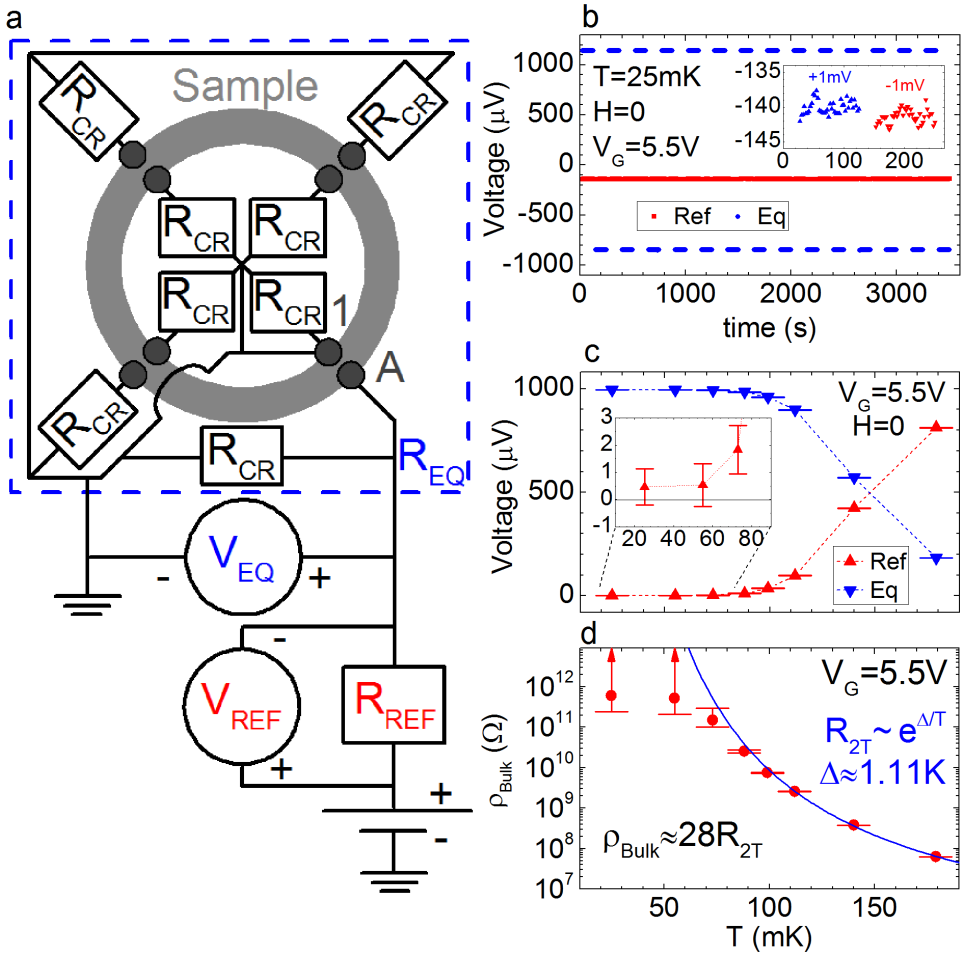

Figure 4.9: Quasi-DC measurement of the bulk resistance between the edges. a) Circuit schematic depicting the equivalent resistance measurement. R_{REF} is a reference 10 MΩ resistor, R_{CR} represents the unintentional shunt effects in the cryostat wiring, R_{EQ} shows equivalent resistance of the circuit (dashed box), V_{REF} and V_{EQ} represent voltage drops over the reference resistor and equivalent resistor. b) Measurement of the equivalent (V_{EQ}) and the reference (V_{REF}) voltages at 25 mK and gate voltage 5.5 V. Inset shows a zoomed in single period of the V_{REF} signal with two colors representing both bias directions. Scale of the inset corresponds to the figure. c) Mean values and standard errors of the equivalent and the reference voltages as a function of temperature obtained from the measurements analogous to (b), at gate voltage 5.5 V. Inset shows a zoomed in scale around zero depicting the noise limited reference voltage signal. Scale units of the inset corresponds to the figure. d) Calculated bulk resistivity with an Arrhenius fit.

AH signal decreases, and vanishes above 18 K which corresponds to a Curie temperature (T_C) of the film.

It is clear that a competition between two different effects is visible in the gate voltage dependence of ρ_{XX} plotted in Fig. 4.8d, collected from a Hall bar patterned from the same wafer. This is especially visible in the non-monotonic curve collected at 1.4 K. This shape is a result of the coexistence of the bulk resistivity and the chiral edge channel contributions. The bulk resistivity has a single maximum in gate bias in the bulk gap at around +5 V, and the chiral edge channel for this four-terminal configuration has a value of 0, acting to electrically short the two voltage leads. The total measured value of ρ_{XX} depends on the ratio between both contributions, and this ratio depends on both the temperature and the applied gate voltage.

The results in the low temperature limit indeed show that only the edges of the Corbino are conducting, and the bulk separating the edge channels is insulating. In order to better resolve how large the resistance between the two edge channels is, a quasi-DC method was implemented. Fig. 4.9 shows the measurement used to obtain the estimate of bulk resistivity in the low temperature limit. A quasi-DC (or reversed-DC) method allows to minimize the capacitive coupling in the cryostat wiring. A square wave voltage bias excitation with frequency of approx. 4 mHz and amplitude of 1 mV is applied to contact A, and contact 1 is grounded. A schematic of the circuit is depicted in Fig. 4.9a. A series 10 MΩ reference resistor (R_{REF}) is used to measure the total current (by measuring the voltage drop V_{REF}), and a voltage drop between the biased contact A and the ground is measured (V_{EQ}).

If the cryostat wiring resistance (or impedance) to the ground (in the schematic depicted as resistors R_{CR}, for our cryostat this DC resistance is of the order of 100 GΩ) is significantly larger than the sample resistance, then the measured equivalent resistance R_{EQ} (a blue colored box in the schematic) equals the two-terminal resistance V_{A-1}/I_{A-1} between both biased contacts. In general it is clear that all the parasitic current paths from the cryostat wiring to the ground (through the R_{CR} resistors in the schematic) are in parallel with the main current path, therefore a measured R_{EQ} value must always be smaller than the real resistance V_{A-1}/I_{A-1}. Therefore a measurement of R_{EQ} provides a lower bound on the real sample resistance.

Fig. 4.9b shows collected V_{EQ} (blue color) and V_{REF} (red color) signals, as a function of time. The measurement is performed at gate voltage 5.5 V and zero external magnetic field. The inset shows a zoomed in section of the V_{REF} signal for a single excitation

period. A visible shift from 0 in both signals is primarily a result of the leakage current through the gate dielectric (the offset nearly vanishes when the gate voltage is set to 0 V, not shown here). Another possible offset source stems from the thermal voltages in the cryostat wiring. Nevertheless a square wave measurement allows to correct for these offsets by calculating the signal amplitude.

In order to obtain a measure of the resistance, this amplitude is calculated. The measurement points directly following the bias direction reversal are removed to minimize the capacitive effects (a sharp bias voltage switch from +1 mV to -1 mV creates an evanescent high frequency component with a lower impedance). Then the amplitude is averaged over the entire measurement collection time, and a mean value with a standard uncertainty is calculated. The same kind of measurement is then performed at different temperatures, and the resulting voltage signals are plotted in Fig. 4.9c as a function of temperature.

As visible in the inset in Fig. 4.9c, the reference signal is noise limited (the mean value is smaller then the signal standard deviation) at 55 mK and below. Therefore as a conservative upper bound on the real voltage signal we take a standard deviation of the distribution, which as a result gives a lower bound on the R_{EQ} (and therefore a lower bound on the resistance V_{A-1}/I_{A-1}) of 11.2 GΩ at 55 mK.

Since the bulk is insulating and both edges of the device have conducting chiral edge channels, one gets two equipotential rings on both edges of the device. Then effectively a traditional Corbino geometry is formed with a single inner and a single outer contact, and an aspect ratio that enters the calculation is given by the width between the edges divided by the ring circumference. This ratio is approx. 1/28, which in turn results in a lower bound on the bulk resistivity of 310 GΩ per square. If a mean value of the reference signal at 55 mK is taken to be exact, the resistance goes as high as 18.5 GΩ, and a bulk sheet resistance as high as 520 GΩ per square.

Above 55 mK a signal on the reference resistor can be properly resolved. The obtained resistance as a function of temperature in Fig. 4.9d follows an Arrhenius thermal activation ($e^{\Delta/T}$), with a characteristic temperature Δ of 1.11 K.

4.2.3 A non-local measurement scheme and the edge channel chirality.

The multi-terminal setting on a Corbino ring allows one to investigate a role of chiral edge channel transport when the quantization is no longer observable in the experiment. For that purpose, a bias voltage (AC 2 Hz) is applied to contact A and contact 1 is grounded,

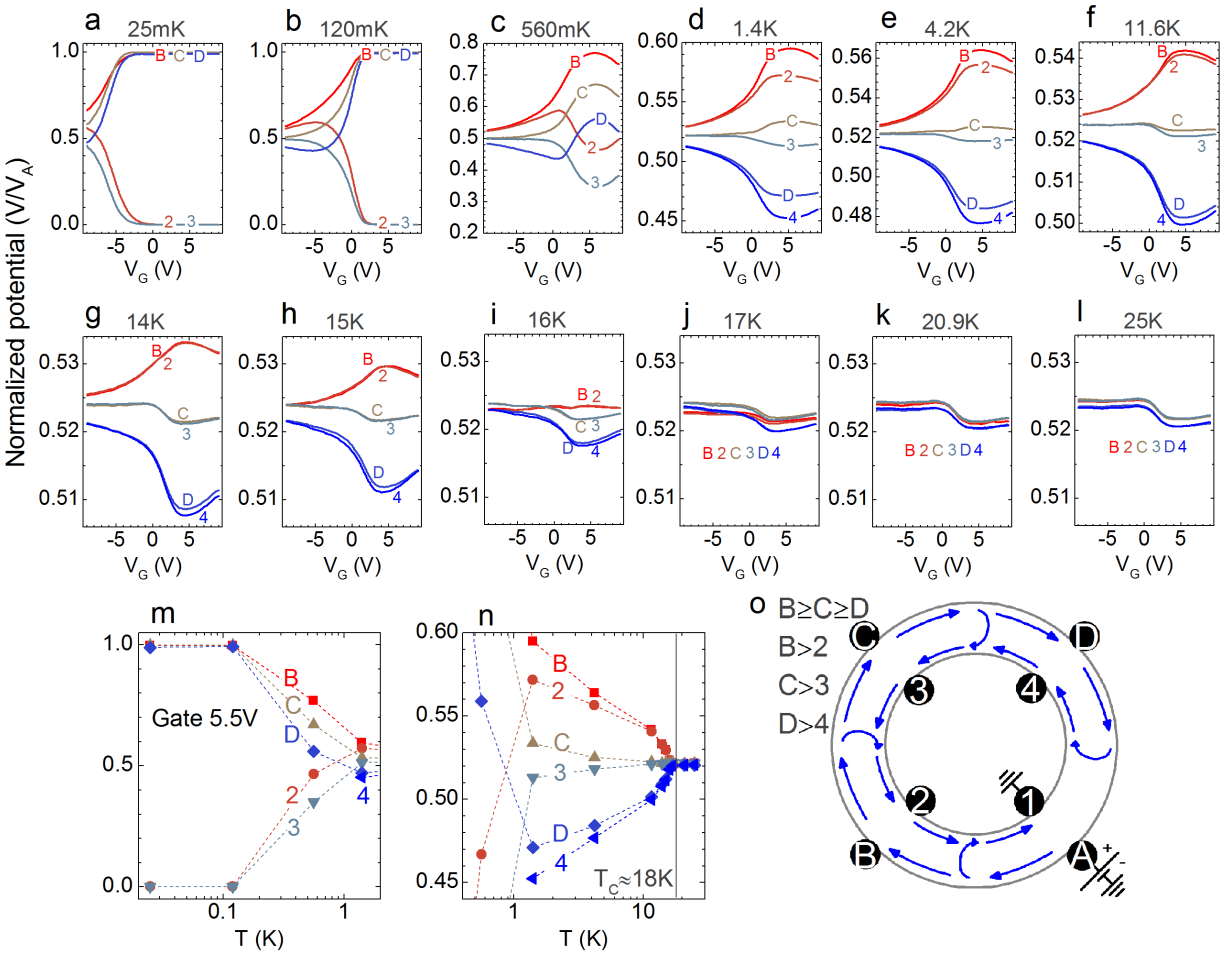

Figure 4.10: Zero field non-local potential mapping for a wide range of temperatures, ranging from 25 mK to 25 K. Contact A is biased, and contact 1 is grounded. All potentials are normalized to the bias voltage. At 1.4 K and above, the measurements of contacts B and 2 were multiplied by a factor of 1.00357, and contacts C and 3 by a factor of 0.9943, to correct for the amplifier gain differences between the different instruments in the experiment. For clarity, in (m) and (n) a temperature dependence of all potentials at gate 5.5 V is plotted with a marked 18 K Curie temperature of the material. o) A schematic depicting the current flow direction for chiral edge channels with bulk dissipation.

and the individual potentials of the remaining contacts are measured with reference to the ground.

Such measurements are presented in Fig. 4.10. Gate sweeps are measured at various temperatures ranging from 25 mK to 25 K. All potentials are normalized to a voltage applied to contact A, which below 1 K is 100 μV, and above 1 K is typically 5 mV. The data is collected at zero external magnetic field in a magnetized state.

In order to properly resolve the signals at higher temperatures (1.4 K and higher), the voltage drops were measured utilizing additional high input impedance differential amplifiers (with an input impedance of the order of 1 TΩ), placed between the sample and the lock-in amplifiers. In order to correct for the amplifier gain errors, a ratio of the gains between the different lock-ins (paired with the differential amplifiers) was measured on a standalone resistor outside of the cryostat. Afterwords the collected measurements from the sample were multiplied by the obtained scaling factors (contacts B/2 by a factor of 1.00357, and C/3 by 0.9943).

At 25 mK and 120 mK, when the gate bias is tuned into the QAHE plateau (center at approx. +5 V), the contacts along the outer edge are equipotential to the biased contact A, whereas the contacts along the inner edge are equipotential to the grounded contact 1. This behavior is consistent with the chiral edge channel conductance being significantly larger than the conductance between the edges.

Interesting behavior is observed when the system is tuned outside of the quantized regime, either by changing the gate voltage, or by increasing the temperature. When the gate voltage is set to -9 V, a Fermi level is in the valence band, and therefore the bulk is conducting. In such scenario the equipotentials are no longer visible in the experiment, and all measured contact potentials tend towards the value of 0.5, an average potential between the two biased contacts. Interestingly however, a clear chirality is visible in the data with potentials $V_B > V_C > V_D$ and $V_2 > V_3 > V_4$, for a temperature range vastly exceeding the temperature regime where QAHE is visible. This shows that a contribution from the chiral edge channels is clearly detectable despite the appearance of conducting bulk channels.

Now focusing on the gate voltage of +5.5 V, where the Fermi level is located in the gap, and at low temperature a perfect QAHE is observable. By changing the temperature, a contribution from the bulk conductivity can be switched on gradually. When the temperature is increased, the measured potentials again tend towards an average value between the source and drain potential of 0.5.

Our qualitative interpretation of the data is based on Fig. 4.10o where schematically a

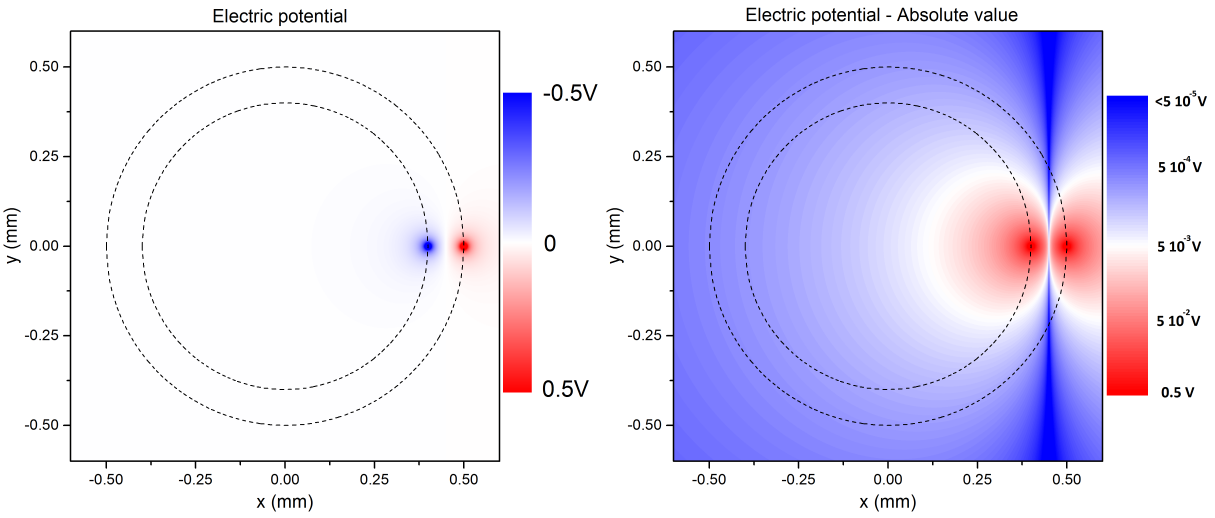

Figure 4.11: A normalized electric potential distribution of an electric dipole in two dimensions, with overlaid real dimensions of our Corbino ring (dashed circles represent both edges). For clarity on the right hand side an absolute value of the potential is plotted in the log scale.

current flow in the Corbino ring is depicted, with a chiral edge channel transport and bulk mediated scattering between the two edges. As a current escapes the biased contact A, it moves clockwise (for the depicted magnetization direction) following the edge channel chirality on the outer edge producing the potential profile $V_B > V_C > V_D$, and it can also partially scatter to the opposite edge and move counter-clockwise along the inner chiral edge channel. This therefore also produces a potential difference between the outer and the inner edge at every point around the ring, leading to $V_B > V_2$, $V_C > V_3$, and $V_D > V_4$.

We find that such criteria are satisfied up to approx. 18 K Curie temperature of bulk ferromagnetism. Above T_C we find that all contact potentials are at an equipotential (close to 0.5) within the experimental uncertainty. A gate voltage dependent value close to 0.52, rather then a constant value of 0.5, is a result of small difference between the contact/lead resistances of the biased contacts A and 1, as well as a gate voltage influence on those two resistances.

In the absence of chiral edge channels, one would expect an electric potential to drop directly from contact A to contact 1. Indeed to a first approximation, the electric potential would follow that of an electric dipole. This is plotted in Fig. 4.11, where an electric potential distribution for an electric dipole is plotted, normalized so that at a source contact width the potential is +0.5 V, and drain contact width -0.5 V. Dashed lines represent the overlaid real dimensions of the Corbino ring.

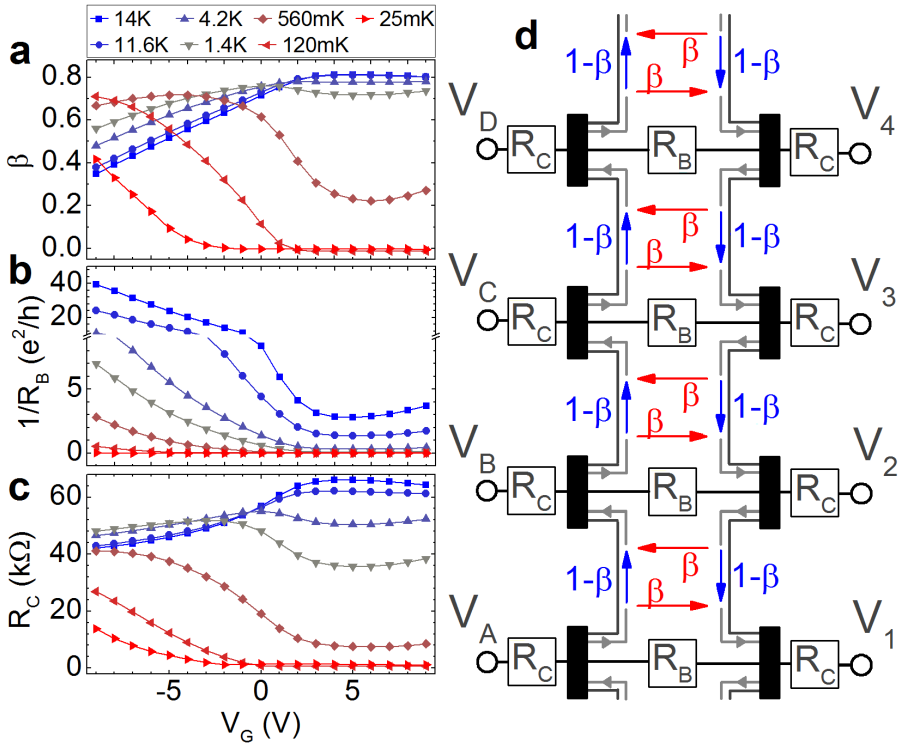

Figure 4.12: Gate voltage and temperature evolution of: a) β, b) $1/R_B$, and c) R_C. d) Schematic of the device layout describing the model. Colored arrows represent the transmission probabilities dependent on β. Schematic includes the resistors simulating the lead resistance R_C in series with every contact, and resistors R_B. Parameters in a-c were fitted to the data points plotted in Fig. 4.13. Figure taken from [51].

It is clear from the figure that the potential (as well as an electric field) is very close to zero around the ring at the positions where all of the detection contacts are located. Specifically all potentials are contained within 0.001 V. In addition V_B=V_D and V_2=V_4 must be satisfied due to symmetry.

Given such small potentials and electric fields, there is no current flowing far from the biased contacts A and 1, and therefore any corrections stemming from the magnetism and an ordinary AHE (which results from asymmetric scattering of current carrying electrons) from the bulk states must be negligible, and therefore the large non-local signals that we observe can originate only from the chiral edge channels.

4.2.4 The Landauer-Büttiker modeling.

In order to quantify the analysis, a model is developed based on the Landauer-Büttiker formalism [57]. Application of this formalism to our 8-terminal Corbino geometry leads

to a system of 8 linear equations relating the flowing currents with the contact potentials. A schematic is presented in Fig. 4.12d. The bulk conductance channels are simulated using two parameters: i) R_B that provides a current path bypassing the edge state and simulating the bulk conductance, directly connecting the nearest contacts on the opposite edges, and ii) β provides a scattering probability between the chiral edge states on both edges (see Fig. 4.12d). Due to large distances involved, a bulk conductivity between the non-adjacent contacts can be safely neglected.

System of 8 linear equations for a positively magnetized state can be written in a matrix form as:

$$\begin{bmatrix} I_A \\ I_B \\ I_C \\ I_D \\ I_1 \\ I_2 \\ I_3 \\ I_4 \end{bmatrix} = \frac{e^2}{h} \begin{bmatrix} T_1 & T_2 & 0 & 0 & T_3 & 0 & 0 & 0 \\ 0 & T_1 & T_2 & 0 & 0 & T_3 & 0 & 0 \\ 0 & 0 & T_1 & T_2 & 0 & 0 & T_3 & 0 \\ T_2 & 0 & 0 & T_1 & 0 & 0 & 0 & T_3 \\ T_3 & 0 & 0 & 0 & T_1 & 0 & 0 & T_2 \\ 0 & T_3 & 0 & 0 & T_2 & T_1 & 0 & 0 \\ 0 & 0 & T_3 & 0 & 0 & T_2 & T_1 & 0 \\ 0 & 0 & 0 & T_3 & 0 & 0 & T_2 & T_1 \end{bmatrix} \begin{bmatrix} V_A \\ V_B \\ V_C \\ V_D \\ V_1 \\ V_2 \\ V_3 \\ V_4 \end{bmatrix} \tag{4.1}$$

and for a negatively magnetized state as:

$$\begin{bmatrix} I_A \\ I_B \\ I_C \\ I_D \\ I_1 \\ I_2 \\ I_3 \\ I_4 \end{bmatrix} = \frac{e^2}{h} \begin{bmatrix} T_1 & 0 & 0 & T_2 & T_3 & 0 & 0 & 0 \\ T_2 & T_1 & 0 & 0 & 0 & T_3 & 0 & 0 \\ 0 & T_2 & T_1 & 0 & 0 & 0 & T_3 & 0 \\ 0 & 0 & T_2 & T_1 & 0 & 0 & 0 & T_3 \\ T_3 & 0 & 0 & 0 & T_1 & T_2 & 0 & 0 \\ 0 & T_3 & 0 & 0 & 0 & T_1 & T_2 & 0 \\ 0 & 0 & T_3 & 0 & 0 & 0 & T_1 & T_2 \\ 0 & 0 & 0 & T_3 & T_2 & 0 & 0 & T_1 \end{bmatrix} \begin{bmatrix} V_A \\ V_B \\ V_C \\ V_D \\ V_1 \\ V_2 \\ V_3 \\ V_4 \end{bmatrix} \tag{4.2}$$

where T_1=1+1/R_B (R_B is a unitless quantity normalized to h/e^2), T_2=-(1-β), and T_3=-(β+1/R_B).

It is clear from (4.1) and (4.2), that when 1/R_B=β=0 the system reduces to two independent systems of 4 linear equations, each describing separately the two edges of the device and giving a result equivalent to an ordinary integer quantum Hall effect with a single chiral edge state.

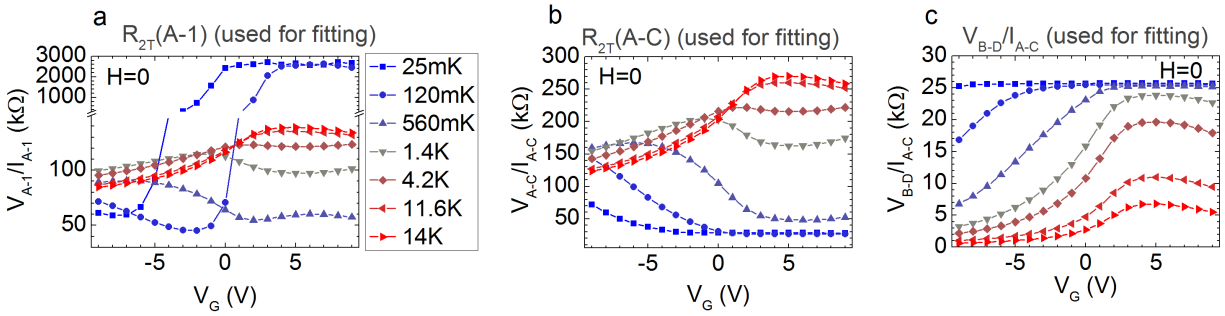

Figure 4.13: The measurement data points used for the fitting of the three model parameters: a) Two terminal resistance V_{A-1}/I_{A-1}, b) Two terminal resistance V_{A-C}/I_{A-C}, and c) Four terminal resistance V_{B-D}/I_{A-C}. The V_{A-1}/I_{A-1} value of approx. 3 MΩ at low temperature is a limit resulting from the capacitive shunt between the leads in the cryostat and input impedance of the voltage reading instruments. An accurate measurement of V_{A-1}/I_{A-1} in the insulating regime is analyzed in the Fig. 4.9.

The choice of source and drain current leads allows for an exact solution of the model for all of the potentials on the remaining contacts. All of the calculated formulas used for the different simulations presented throughout this chapter are presented in the Appendix.

All three fitting parameters (R_B,β,R_C) can be obtained by fitting the model to the measurements plotted in the Fig. 4.13. This includes the following three resistance measurements: the two-terminal resistance $R_{A1,A1}=V_{A-1}/I_{A-1}$, the two terminal resistance $R_{AC,AC}=V_{A-C}/I_{A-C}$, and the four terminal resistance $R_{BD,AC}=V_{B-D}/I_{A-C}$. After solving the Landauer-Büttiker network for the resistance configurations, the three resulting equations relating the three resistances with the three model parameters are:

$$R_{A1,A1} = \frac{h}{e^2}\frac{3\beta + 1 + 4/R_B}{4(\beta + 1/R_B)(1 + 1/R_B)} + 2R_C \tag{4.3}$$

$$R_{AC,AC} = \frac{h}{e^2}\frac{1}{1-\beta} + 2R_C \tag{4.4}$$

$$R_{BD,AC} = \frac{h}{e^2}\frac{1}{1 + 1/R_B} \tag{4.5}$$

The parameter values obtained this way are plotted in Fig. 4.12a-c. The model is already fully determined by the three above resistances, and no fitting to any other analyzed configuration is performed.

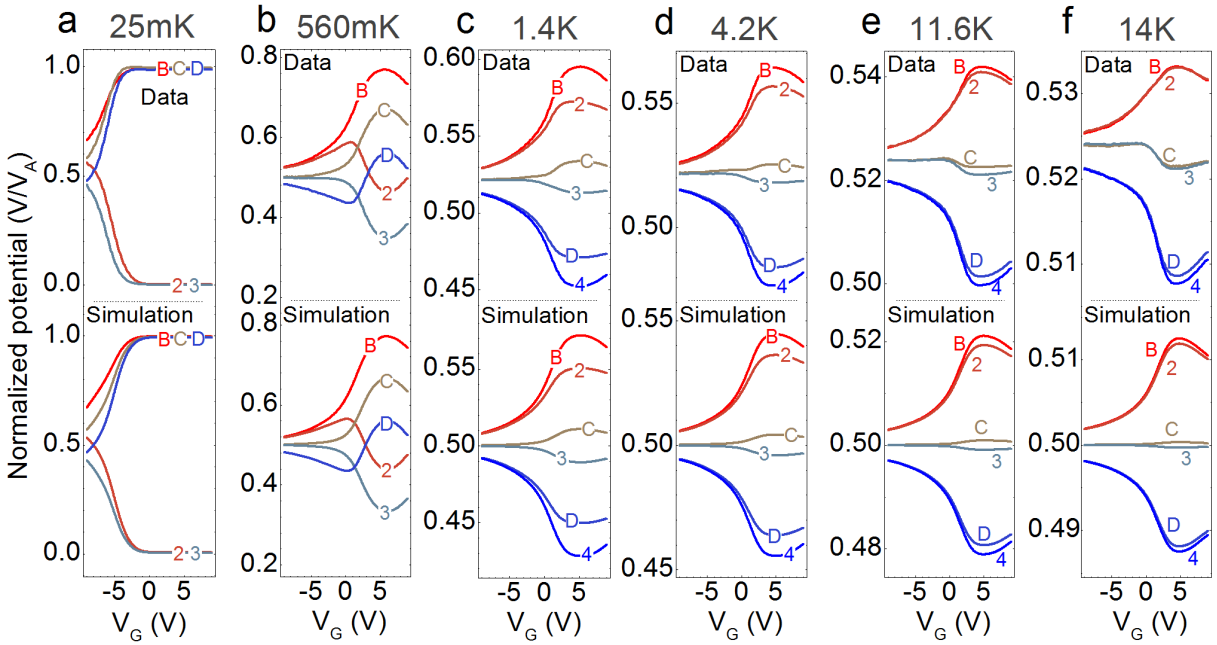

Figure 4.14: Individual contact potentials in the magnetized state at zero external magnetic field, normalized to the bias voltage. The bias voltage is applied to contact A with contact 1 grounded. The temperature of the measurement is: 25 mK (a), 560 mK (b), 1.4 K (c), 4.2 K (d), 11.6 K (e), and 14 K (f). Below the data, the corresponding simulated curves are plotted. (Contact 4 was not accessible during the measurement run below 1.4 K). At 1.4 K and above, the measurements of contacts B and 2 were multiplied by a factor of 1.00357, and contacts C and 3 by a factor of 0.9943, to correct for the amplifier gain differences between the different instruments in the experiment. Figure adapted from [51].

The contact/lead resistance R_C (Fig. 4.12c) qualitatively follows resistivity obtained from a traditional Hall bar geometry (plotted in Fig. 4.8d), which stems from a joint effect of both bulk resistivity and edge channel contributions.

Similarities between R_C (Fig. 4.12c) and ρ_{XX} (Fig. 4.8d) suggest that the resistance R_C is fully determined by the resistivity of a mesa constriction connecting each ohmic contact with the mesa ring. This is further validated when a second sample is measured where this constriction width is increased from 15 to 50 μm, and otherwise the shape of the device remains the same. Summary of the same analysis performed on the wide contacts sample is presented in Fig. 4.15. Indeed when the same Landauer-Büttiker analysis are performed, the obtained value for R_C is significantly reduced in a wider contacts sample, while both β and R_B remain nearly identical (parameters for a wide contacts sample are plotted in Fig. 4.15f, and can be compared to the narrow contacts sample plotted in Fig. 4.12a-c).

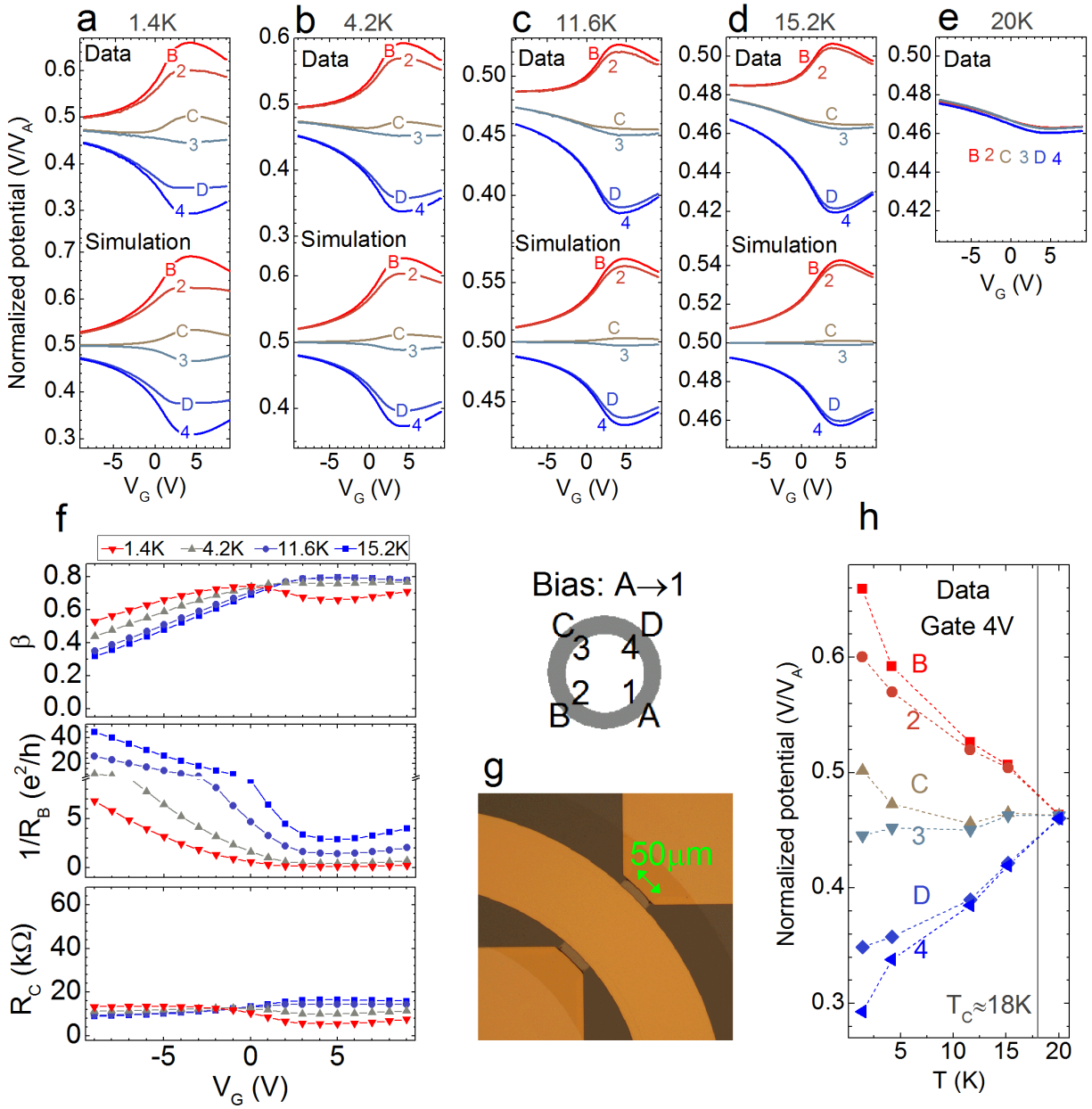

Figure 4.15: Non-local potential mapping measurements collected from a second sample with wider contacts, a photo is visible in (g). Contact A is biased, and contact 1 is grounded. All potentials are normalized to the bias voltage. The measurements of contacts B and 2 were multiplied by a factor of 1.00357, and contacts C and 3 by a factor of 0.9943, to correct for the amplifier gain differences between the different instruments in the experiment. For clarity, in (h) we plot a temperature dependence of all potentials at gate 4 V. f) Corresponding parameters obtained for this sample, plotted with the same scale as Fig. 4.12 for clarity of comparison. Figure adapted from [51].

As expected, the gate voltage and temperature evolution of bulk conductance $1/R_B$ (Fig. 4.12b) shows a clear minimum when the gate is tuned into the bulk gap close to the gate voltage of +5 V, and at sufficiently small temperatures vanishes.

The evolution of inter-edge scattering rate β (Fig. 4.12a) roughly correlates with the bulk conductance $1/R_B$, consistent with a bulk mediated scattering between the edges. A drop in the value of β observed at large temperatures and large negative gate voltages could result from the scattered carriers finding pure bulk paths to other contacts (when bulk conductance gets large in comparison to the edge channel conductance), which are not accounted for in our simple model.

Without performing any additional fitting, the parameters from Fig. 4.12a-c are used to generate the main non-local configuration of potentials (the same configuration as analyzed in Fig. 4.10), with a bias voltage applied to contact A and contact 1 grounded. Fig. 4.14 shows a direct comparison between the simulation and the experiment, and a good agreement is found in all cases.

4.2.5 Robustness of the analysis - other measurement configurations.

A multi-terminal Corbino geometry offers a possibility to rigorously test the model analysis against the experiment, as 8 ohmic contacts allow for a large amount of independent measurement source-drain configurations. Most of the different biased contact pairs create a unique potential profile along the device, that can be probed and directly compared to the values as expected from the modeling.

Fig. 4.16 shows analysis of 5 independent source-drain contact pairs for both magnetization directions (both chiralities). All measurements are performed at 1.4 K and at zero magnetic field in the magnetized state. Bias voltage is applied to contact A, and grounded contact changes between different configurations. All remaining measured potentials are normalized to a voltage applied at contact A.

All configurations in Fig. 4.16 show a very good agreement with the simulated curves, without introducing any new fitting parameters. This shows robustness of the model.

When the different bias configurations are compared at lower temperatures, a similarly good agreement with the modeling is found. Fig. 4.17 shows such data with simulations collected at 25 mK, 120 mK, and 560 mK.

An interesting behavior is observed when the bulk is insulating, and both biased contacts are located along the same edge. This is the case at 25 mK when the system in tuned

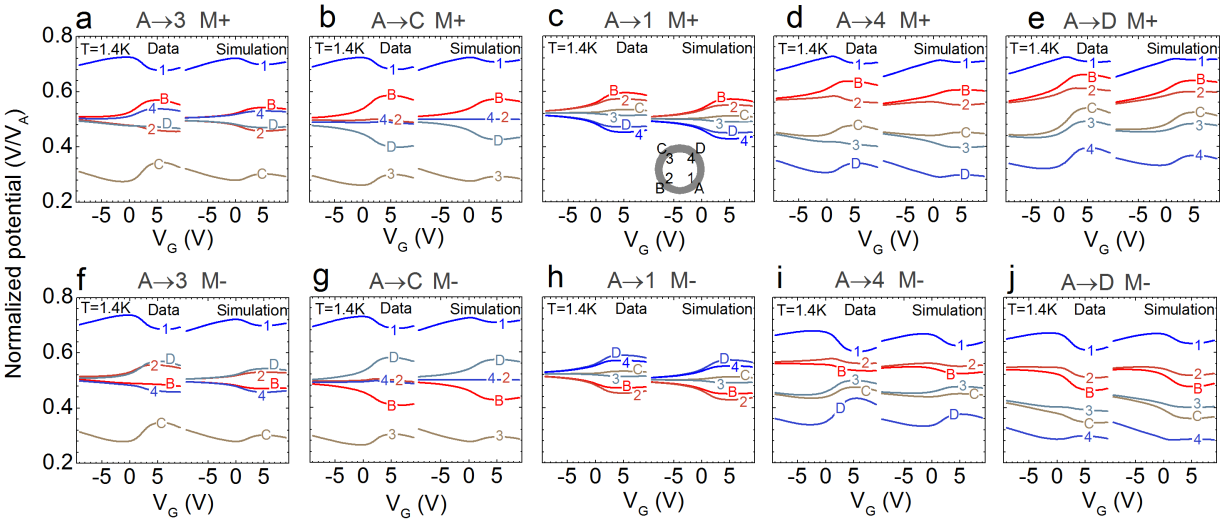

Figure 4.16: 10 independent potential mapping measurements compared side by side with the model simulation, using the same set of parameters in all 10 simulations. Data was collected at 1.4 K at zero external magnetic field in a magnetized state. Data corresponds to the biased contacts and magnetization: a) A-3 M+, b) A-C M+, c) A-1 M+, d) A-4 M+, e) A-D M+, f) A-3 M-, g) A-C M-, h) A-1 M-, i) A-4 M-, and j) A-D M-. Here "M+" and "M-" represent the positively and negatively magnetized state.

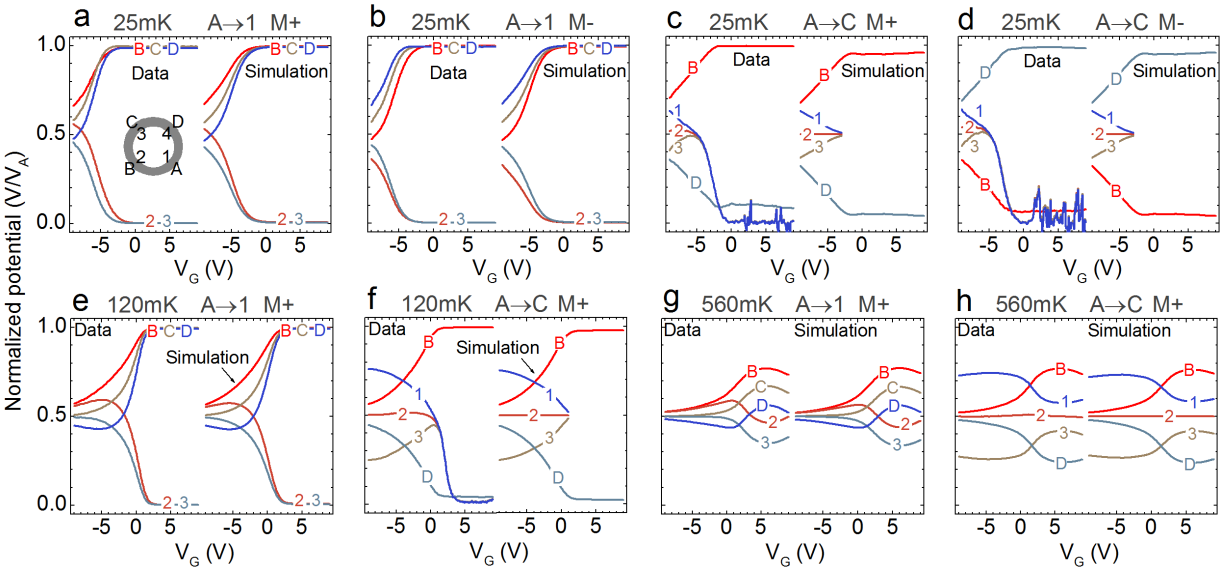

Figure 4.17: Potential mapping measurements compared side by side with the curves simulated by the model. Data was collected at zero external magnetic field in a magnetized state. Data corresponds to the temperature, biased contacts, and magnetization: a) 25mK A-1 M+, b) 25mK A-1 M-, c) 25mK A-C M+ d) 25mK A-C M-, e) 120mK A-1 M+, f) 120mK A-C M+, g) 560mK A-1 M+, and h) 560mK A-C M+. Here "M+" and "M-" represent the positively and negatively magnetized state.

into a quantized plateau regime (around +5 V gate bias). As both source and drain are located along the same edge, the other edge has no defined reference potential, and indeed is electrically floating.

This is visible in the Fig. 4.17c and 4.17d, where all signals along the outer (biased) edge are well defined, and all signals along the inner edge fluctuate randomly around 0. This is an experimental artifact resulting from the AC measurement of the randomly drifting DC potential. The actual potential value was verified to be floating when a separate DC measurement was performed (not shown). At the same time an equipotential is observed along the inner edge, as all potentials read by the lock-ins have the same value, including the fluctuations.

This is also consistent with the Landauer-Büttiker modeling. In such scenario, when both β and $1/\mathrm{R}_B$ are set to 0 (no coupling between the edges) and both current leads are located on the outer edge, potentials for the inner edge contacts yield explicitly an equipotential V_1=V_2=V_3=V_4, with an undefined value.

4.2.6 Estimate of the upper limit on deviation from quantization based on the modeling.

Based on the introduced Landauer-Büttiker modeling, it is possible to obtain an upper bound on the relative deviation from quantization of the $\mathrm{V}_{B-D}/\mathrm{I}_{A-C}$ signal (a four-terminal configuration that yields a quantized value of $\mathrm{h/e}^2$ for an isolated chiral edge channel) at zero external magnetic field.

The two terminal resistance $\mathrm{V}_{A-1}/\mathrm{I}_{A-1}$, for small β and $1/\mathrm{R}_B$ values (β,$1/\mathrm{R}_B$<<1) can be approximated as:

$$\frac{V_{A-1}}{I_{A-1}} = \frac{h}{e^2}\frac{3\beta + 1 + 4/R_B}{4(\beta + 1/R_B)(1 + 1/R_B)} + 2R_C \approx \frac{h}{e^2}\frac{1}{4(\beta + 1/R_B)} \tag{4.6}$$

and therefore:

$$1/R_B \approx \frac{h}{e^2}\frac{1}{4(V_{A-1}/I_{A-1})} - \beta \tag{4.7}$$

Since β must be larger than (or equal to) 0, the quantity $\frac{h}{e^2}\ 1/(4(\mathrm{V}_{A-1}/\mathrm{I}_{A-1}))$ is itself an upper bound on the value of $1/R_B$.

The four-terminal resistance $\mathrm{V}_{B-D}/\mathrm{I}_{A-C}$ (effectively an R_{xy}), for a small value of $1/\mathrm{R}_B$

($1/\mathrm{R}_B << 1$) can be approximated as:

$$\frac{V_{B-D}}{I_{A-C}} = \frac{h}{e^2}\frac{1}{1+1/R_B} \approx \frac{h}{e^2}(1-1/R_B) \tag{4.8}$$

Therefore following (4.7) and (4.8), in the regime of β,$1/\mathrm{R}_B << 1$, the $1/\mathrm{R}_B$ is a relative deviation from quantization of $\mathrm{V}_{B-D}/\mathrm{I}_{A-C}$, and the upper limit on that deviation is given by the quantity $\frac{h}{e^2}$ $1/(4(\mathrm{V}_{A-1}/\mathrm{I}_{A-1}))$.

From the analysis in Fig. 4.9 we know that the resistance $\mathrm{V}_{A-1}/\mathrm{I}_{A-1}$ must be larger than 11.2 GΩ at 55 mK and below. This results in an upper bound on the relative deviation from quantization of $\mathrm{V}_{B-D}/\mathrm{I}_{A-C}$ of about 0.6 ppm. This number is comparable to a current most precise metrologically comprehensive experiment on our Hall bar sample [12], as analyzed earlier in this chapter.

Interestingly if an Arrhenius activation fit from Fig. 4.9d is taken and extrapolated down to 50 mK instead, A value of the two-terminal resistance $\mathrm{V}_{A-1}/\mathrm{I}_{A-1}$ goes as high as $2\ 10^{13}$ Ω, and the corresponding upper bound on the relative deviation from quantization of $\mathrm{V}_{B-D}/\mathrm{I}_{A-C}$ goes as low as 3 parts per 10^{10}. This, if measured directly using a metrologically traceable method would place the quantum standard in the same regime as the precision of Hall resistance quantization in graphene at high external magnetic fields [56].

Chapter 5

Scaling of the quantum anomalous Hall effect and axion electrodynamics.

In this chapter I present results obtained from our $(V,Bi,Sb)_2Te_3$ films optimized for perfect transport quantization. Specifically I focus on analysis of the scaling behavior of the conductivity tensor components, and the potential implications of this observations are discussed. The results from this chapter are published in the refs. [28, 49, 58].

5.1 Concept of a single-parameter conductivity tensor scaling in the quantum Hall state.

Following the experimental discovery of the integer QHE [4], a good understanding of the underlying physics was achieved relatively quickly, describing what happens in the quantum Hall system when a quantized Hall plateau is observed in the experiment [59, 60]. Soon after, the conductivity tensor components scaling behavior analysis was developed for 2D electron systems [61, 62, 63, 64]. The universality of such scaling was recognized as a useful tool in investigations into underlying physics in the 2D systems.

Specifically, in the analysis first the experimentally obtained resistivity tensor elements ρ_{xx} and ρ_{xy} are converted into the conductivity tensor elements σ_{xx} and σ_{xy}, following the

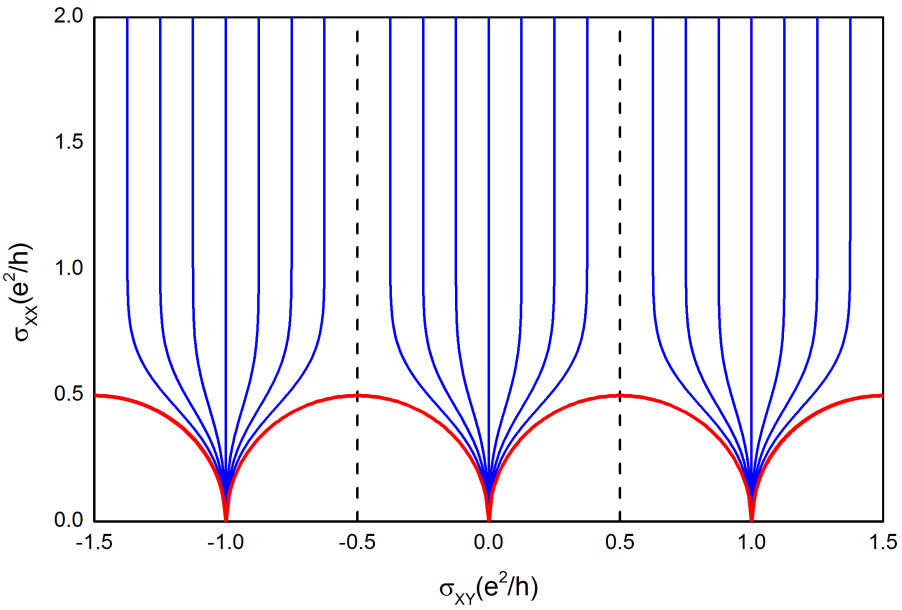

Figure 5.1: A schematic of the global conductivity tensor flow diagram for a 2D electron system. Red color represents the semicircular trajectories connecting the fixed (quantum Hall plateau) points, and blue color the temperature or size driven trajectories.

matrix inversion relations:

$$\sigma_{xx} = \frac{\rho_{xx}}{\rho_{xx}^2 + \rho_{xy}^2} \tag{5.1}$$

$$\sigma_{xy} = \frac{-\rho_{xy}}{\rho_{xx}^2 + \rho_{xy}^2} \tag{5.2}$$

Then the resulting conductivity tensor elements are analyzed in the form of a parametric plot, where a driving parameter can be the temperature, magnetic field, gate voltage bias, or in principle a system size (as this is virtually impossible to properly analyze in an experiment, but is frequently done in theoretical considerations).

When the system is in the integer quantum Hall plateau regime with (σ_{xy},σ_{xx})=(ne^2/h,0), where n is an integer (including the n=0 state where there is no edge channel, and both conductivity components drop to 0, and the entire system is insulating), it turns out that the trajectories connecting such (stable, or fixed) points follow semicircles with centers located at (σ_{xy},σ_{xx})=((n+1/2)e^2/h,0) and a radius e^2/2h. This is known as "the universal semicircle relation", and it turns out to be a universal feature of the quantum Hall transitions [65, 66]. Similar relation turns out to hold for the fractional QHE, where the plateau to

plateau transitions also follow semicircles, with properly rescaled radii and center positions [67].

In the conductivity (σ_{xy},σ_{xx}) plane, such semicircles provide the only possible trajectories directly connecting the different quantum Hall plateaus. A schematic of such (σ_{xy},σ_{xx}) flow diagram is depicted in the Fig. 5.1. Another possible trajectories (blue color in Fig. 5.1) can experimentally be explored by changing the sample temperature [64] (in theoretical considerations typically a system size is manipulated instead, where increase in the system size leads to localization and decrease in σ_{xx}). This means that when the sample is conducting with large σ_{xx}, regardless where in the (σ_{xy},σ_{xx}) plane the system state is located, any trajectory where the σ_{xx} is reduced (such as when the temperature is decreased) will eventually lead to a quantized Hall plateau regime with a fixed point (σ_{xy},σ_{xx})=(ne^2/h,0).

5.2 Conductivity tensor scaling behavior analysis in a 3D topological insulator regime.

The ordinary integer (and fractional) QHE is a fundamentally 2D effect, therefore any samples exhibiting these effects can be effectively treated as 2D objects. As it turns out, when similar scaling analysis are performed on sufficiently thin magnetic TI layers exhibiting the QAHE, precisely the same (σ_{xy},σ_{xx}) scaling can be observed, with the fixed points located at (-e^2/h,0), (0,0), and (e^2/h,0), and the semicircle centers at ($\pm$e^2/2h,0) [68, 36, 69]. Indeed the initial idea behind the QAHE was based on a 2D TI exhibiting the QSHE, with two counter-propagating helical edge channels, and the magnetic exchange interaction reinverting the band structure for one of the two spin species, effectively removing one of the helical edge channels, and as a result giving the QAHE [35].

The scaling behavior in the 3D limit, and specifically when the topological surface state of a 3D TI supporting axion electrodynamics within its volume is analyzed, turns out to be clearly distinct from the 2D case. Thus, by experimentally changing the thickness of the film, it is possible to transition between both fundamentally distinct regimes.

5.2.1 Universal conductivity tensor scaling on a topological surface state with axion electrodynamics in the topologically nontrivial bulk.

Nomura and Nagaosa in 2011 theoretically analyzed the (σ_{xy},σ_{xx}) scaling behavior signature for a magnetic 3D TI [25]. They considered an isolated topological surface state in the shape of a cylinder with a magnetization normal to its surface, enclosing a volume of a 3D TI supporting axion electrodynamics. The flow diagram they theoretically obtained is fundamentally distinct from an ordinary 2D case, and the difference is a fractional shift of the entire flow diagram by $e^2/2h$ along the σ_{xy} axis. The resulting scaling behavior contains a single semicircle with a center located at the origin (0,0) and a radius $e^2/2h$, directly connecting the half-integer quantized Hall plateaus with $\sigma_{xy} = \pm e^2/2h$. Any experimental manifestations of such half-integer quantization $e^2/2h$ can be considered as a direct evidence for an axion insulator state, i. e. an insulating state supporting axion electrodynamics within its volume.

It appears experimentally impossible to probe an isolated topological surface state in shape of a cylinder as envisioned by Nomura and Nagaosa, and therefore directly detect a half-integer quantized Hall conductivity $\sigma_{xy} = \pm e^2/2h$. However, a center of the semicircle in the 3D TI axion limit is located at the origin (0,0), therefore even if an experiment probes the topological contribution from the surface state twice, the center will still be placed at (0,0). This implies that regardless of the amount of parallel topological channels in the experiment, there will be no insulating state when σ_{xy}=0, in a sharp contrast to the ordinary QHE where a point (0,0) is a stable/fixed point in the flow diagram. It is this fundamental difference when the system crosses σ_{xy}=0, between the 2D limit, and 3D limit with axion electrodynamics, that makes both types of scaling diagram possible to access as an experimental observable.

In an experimentally realistic flat film geometry, a flat surface can be mathematically treated as an infinite radius limit of the Nomura-Nagaosa cylinder. Since a uniformly magnetically doped topological insulator layer has a magnetization pointing uniformly in the same direction in space withing its entire volume, the magnetization points outwards on one topological interface, and inwards on the other. Both topological interfaces are therefore flat limits of the Nomura-Nagaosa cylinder, resulting in the doubling of the expected conductivities, and therefore doubling the entire expected flow diagram values. This is schematically depicted in Fig. 5.2, where a difference expected in the experiment between

the 2D and 3D limits is visible. Therefore despite the inability to resolve the individual surface components, such experiment is directly traceable to the half-integer quantized topological surface state response and axion electrodynamics.

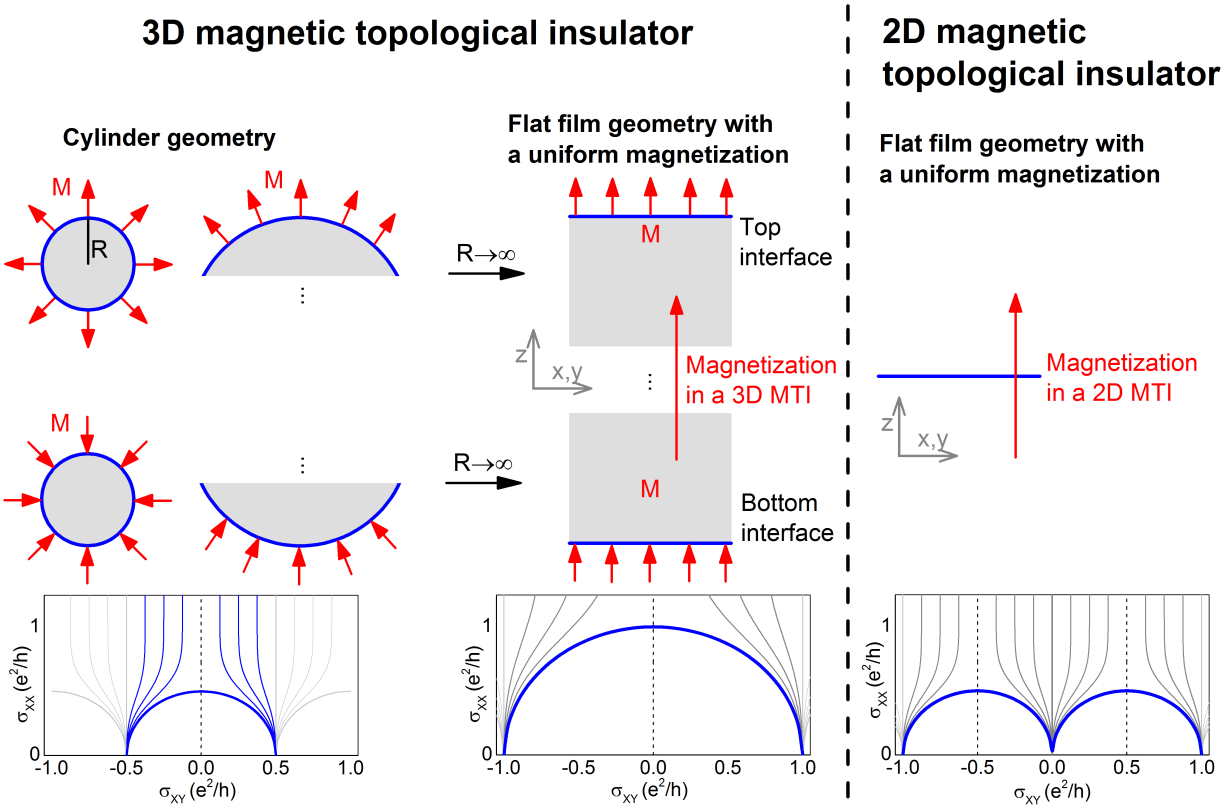

Figure 5.2: Schematic explanation of the conductivity scaling behavior in a flat 3D film geometry with a uniform magnetization. Both "top" and "bottom" interfaces are individually infinite radius limits of the Nomura-Nagaosa cylinder, doubling the expected conductivity values as a result. The expected scaling for both limits is presented on the bottom.

Fig. 5.3a-b depicts magneto-resistivity data collected from two independently grown layers of thickness around 9 nm, optimized for perfect AH resistance quantization. Conductivity tensor elements are calculated from this data, and resulting scaling diagrams are depicted in Fig. 5.3c. The scaling clearly reveals a robust single semicircular trajectory connecting the quantized plateaus, with a center located at the origin (0,0).

The external magnetic field is chosen as a driving parameter in this analysis, as this external parameter (in opposition to the gate voltage or temperature) can reverse the magnetization direction in the film, and thus reveal a full conductivity tensor scaling diagram of the QAHE (a full semicircle). The external magnetic field is the only experimentally

accessible parameter that can induce a plateau to plateau transition. Scaling plots using the temperature or gate voltage as a driving parameter can be found in the appendix.

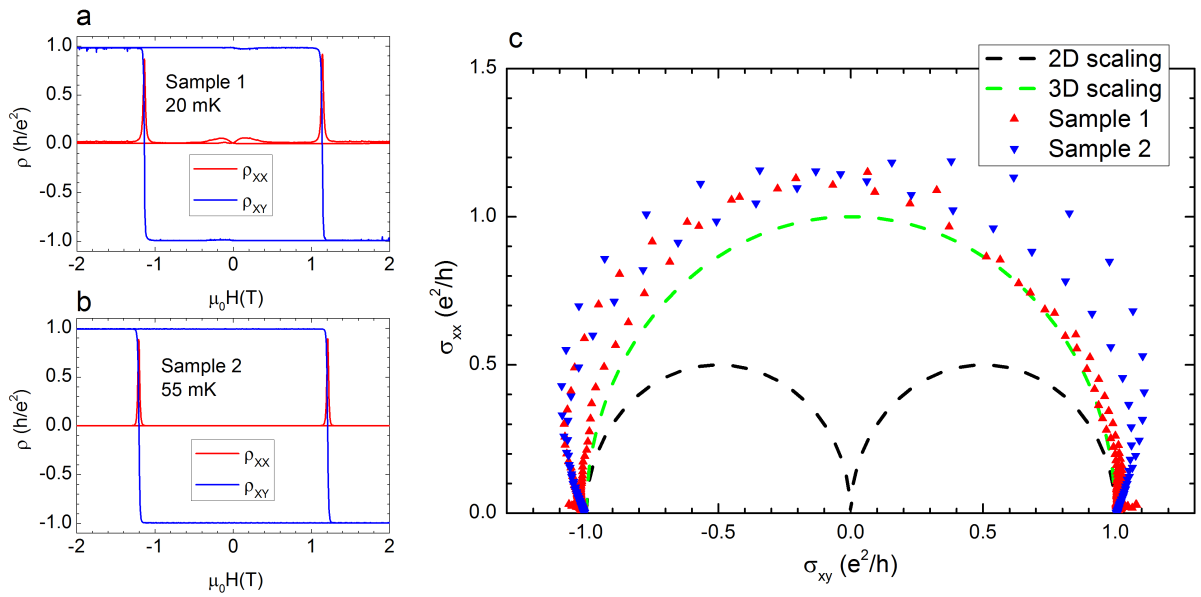

Figure 5.3: a-b) Magneto-resistivity data collected at base temperature of the dilution refrigerator and gate voltage tuned into the QAHE plateau, from two independent MBE layers optimized for perfect quantization. Sample 1 is a 30 μm / 10 μm Hall bar and the sample 2 is a 600 μm / 200 μm Hall bar. c) Calculated conductivity scaling behavior, with dashed lines depicting the expected scaling in a 2D limit (black dashed line), and in a 3D limit (green dashed line) for two parallel interfaces.

5.2.2 Robustness of the axion response - the influence of different parameters.

The conductivity scaling that we observe in our 9 nm thick films is reproducible and robust against a variety of parameters. Fig. 5.4 shows the base temperature magneto-resistivity data and respective scaling behavior for a series of $V_{0.1}(Bi_{1-x}Sb_x)_{1.9}Te_3$ layers grown with a different Bi/Sb composition x on Si(111) substrates, as well as one layer grown on an InP(111) substrate. The samples grown on Si(111) which are away from the Sb content x=0.8, as well as the single layer grown on InP(111), are clearly detuned from the optimal quantized AH resistance regime, and despite that they all follow the same semicircular scaling diagram centered at (0,0). This shows that the axion scaling properties observed in our layers are robust against changes in the material composition.

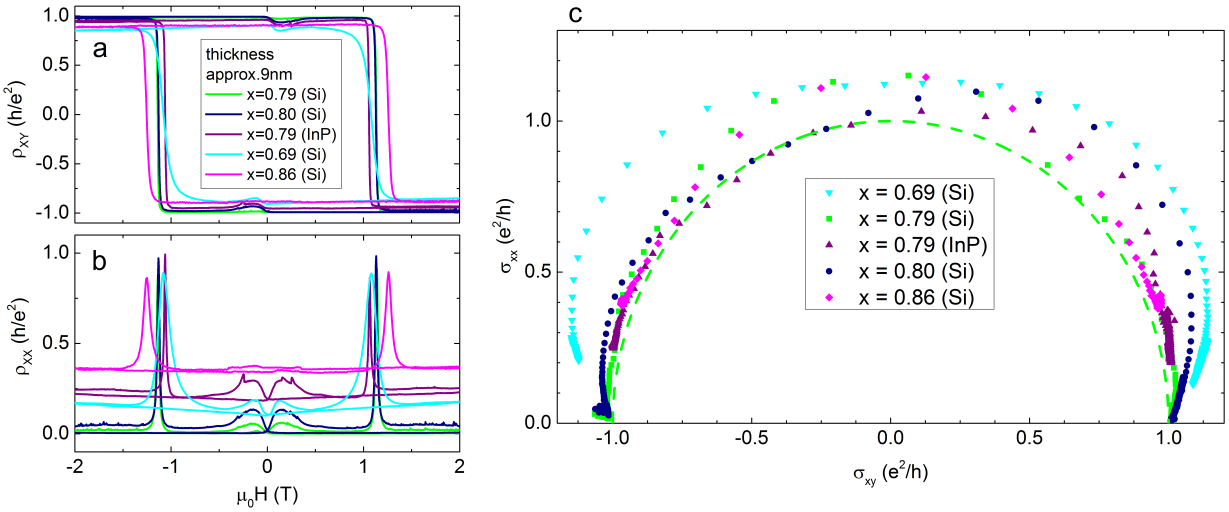

Figure 5.4: a-b) Magneto-resistivity data collected at base temperature of the dilution refrigerator and gate voltage tuned to maximize the AH resistance, from a series of MBE layers of different Sb/Bi composition grown on Si(111) substrate, as well as one layer grown on InP(111). c) Calculated conductivity scaling behavior with a green dashed line depicting the expected scaling in a 3D axion limit for two parallel topological interfaces.

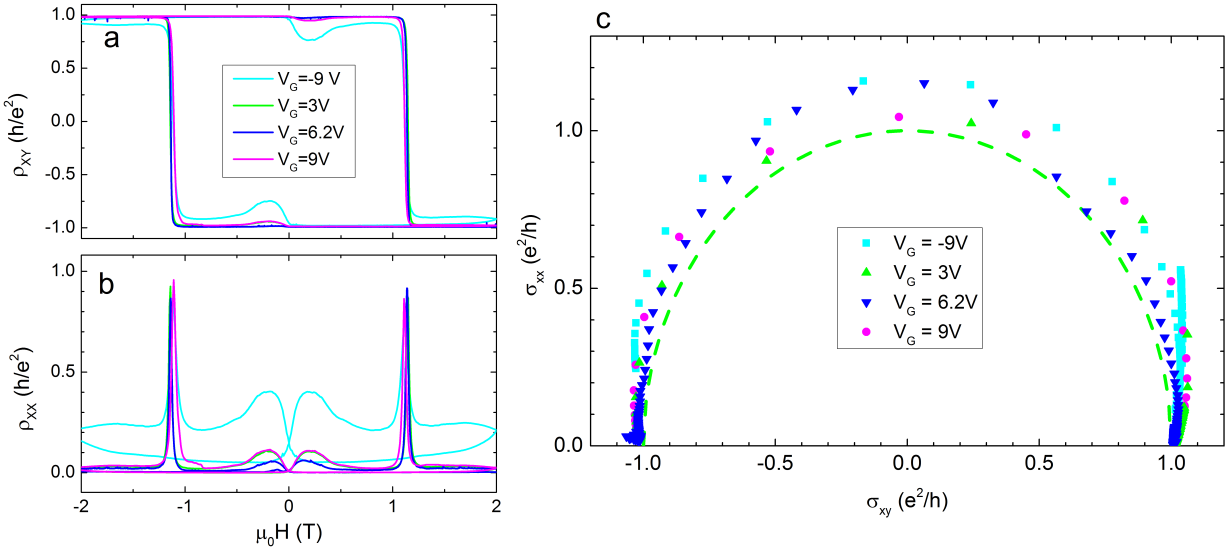

Figure 5.5: a-b) Magneto-resistivity data collected at base temperature of the dilution refrigerator from a perfectly quantized sample, at different gate voltage values. Gate 6.2 V corresponds to the charge neutrality point. c) Calculated conductivity scaling behavior for all gate voltages with a green dashed line depicting the expected scaling in a 3D limit for two parallel topological interfaces.

Similarly, the scaling is robust against the position of the Fermi level in the band

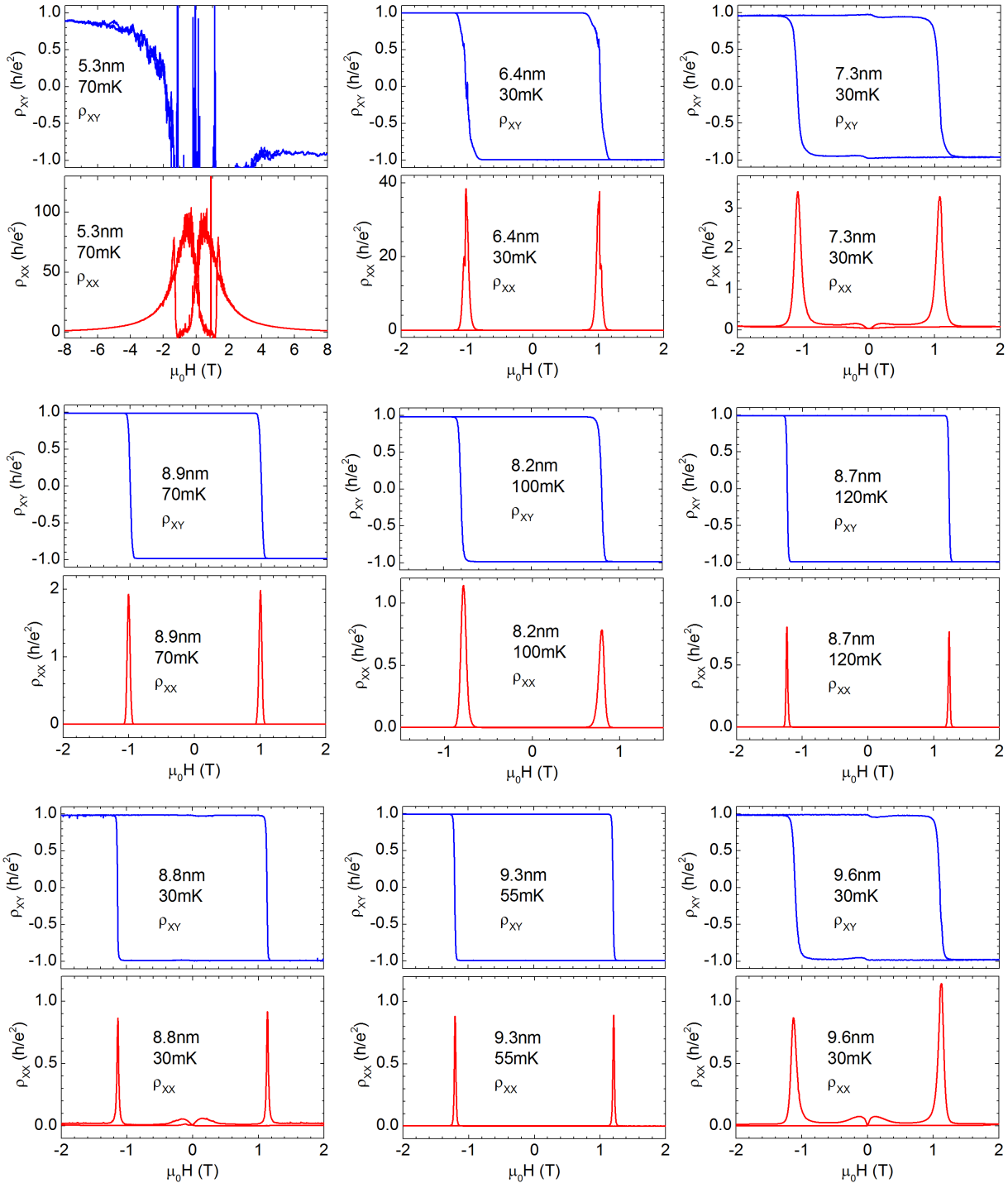

Figure 5.6: Magneto-resistivity measurements collected from a series of 9 samples of various thicknesses, at experimental base temperature. Every curve is labeled accordingly in the figure. Figure adapted from [58].

structure. Fig. 5.5 shows the magnetic field driven scaling behavior for one of the perfectly quantized samples, collected at base temperature and different gate voltage values. In all cases the scaling is consistent with axion electrodynamics.

5.3 Evolution with magnetic layer thickness - crossover between 3D and 2D regime.

The effect of another experimental parameter that can be investigated is the magnetic TI layer thickness. As we observe the 3D scaling behavior in our 9 nm thick layers, it should be possible to reproduce the ordinary integer QHE scaling when the thickness is reduced and the two topological interfaces are no longer decoupled, resulting in a transition to the 2D limit.

Fig. 5.6 shows base temperature magneto-resistivity measurements for a series of samples where the film thickness is varied from 5.3 nm to 9.6 nm. All measurements are collected at an optimal gate voltage maximizing the AH resistance. A good quality QAHE is observed in all layers, with exception of the thinnest of the films. A resistance of the 5.3 nm thick layer during the magnetization reversal gets too large to resolve the resistivity components probed using a four terminal setting. In order to obtain an estimate of the sheet resistance of this film, a two terminal setting with a quasi-DC method is used, equivalent to the measurements on the multi-terminal Corbino analyzed in Fig. 4.9. The magnetic field is slowly swept (5 mT per minute) through the magnetization reversal and the measurement is collected while the field is ramped. This magnetic field sweep is analyzed in Fig. 5.7, and the obtained lower bound on the two-terminal resistance is about 10.7 GΩ. Since the Hall bar has an aspect ratio 3:1, this gives an estimated lower bound on the ρ_{XX} during the magnetization reversal of about 3.6 GΩ per square, or equivalently about 140000 h/e^2.

The conductivity tensor elements are analyzed for the layers of different thicknesses. Both σ_{XX} and σ_{XY} are plotted for 6.4 nm and 9.3 nm thick layers in Fig 5.8a and 5.8b. The magneto-conductivity collected from a 9.3 nm sample shows a single sharp transition in σ_{XY} directly switching between e^2/h to $-e^2/h$ at the coercive field of the ferromagnet, with a single accompanying peak in σ_{XX}. The corresponding curves for a 6.4 nm thick layer reveal a clearly different behavior. σ_{XY} develops a well pronounced zero Hall plateau at the coercivity, and σ_{XX} shows a double-peak behavior during the magnetization reversal.

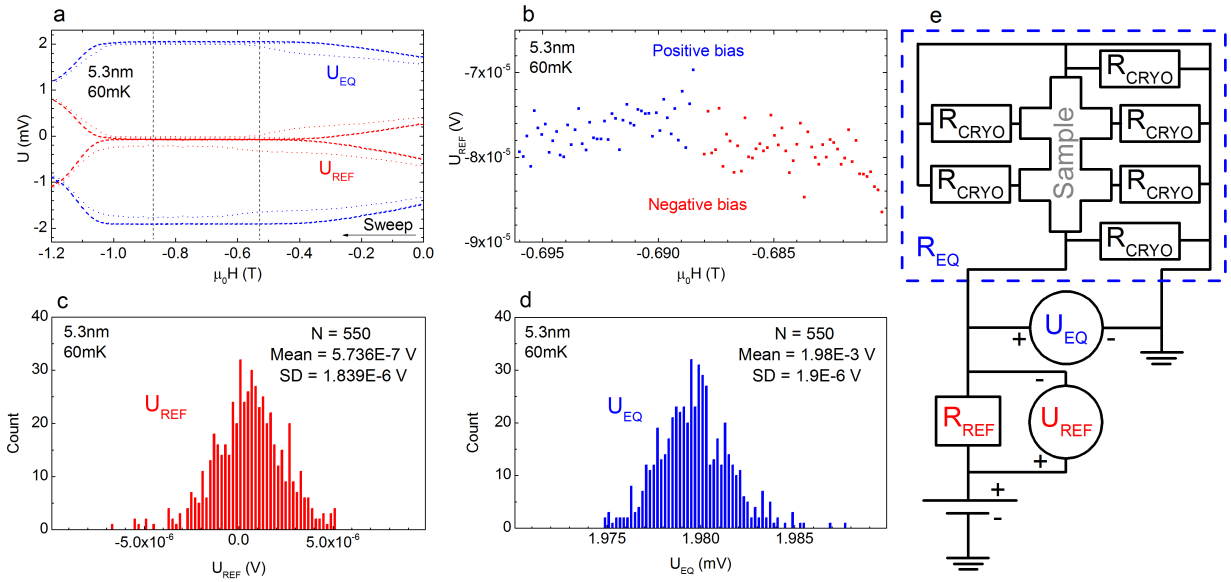

Figure 5.7: Estimate of the lower bound of resistance of a sample patterned from a 5.3nm thick film. The measurement was performed at temperature 60 mK, with a square wave excitation of 5 mHz frequency and 2 mV amplitude. a) Equivalent voltage of the circuit (blue points), and voltage drop over the series 10 MΩ reference resistor (red points). Dashed lines represent the insulating range used for counting statistics. b) Zoomed in section of the reference voltage covering a single period in the insulating regime, blue and red points correspond to the two bias directions. c) and d) Histogram counting of the obtained voltage drop over the reference resistor (c) and equivalent voltage (d). Counting statistics covered 550 data points, and obtained mean values and standard deviations are labeled accordingly in the figures. (e) Schematic of a circuit diagram. R_{REF} is a reference 10 MΩ resistor, R_{CRYO} represents the unintentional shunt effects in the cryostat wiring, R_{EQ} shows equivalent resistance of the circuit (dashed box), U_{REF} and U_{EQ} represent voltage drops over the reference resistor and equivalent resistor. Figure taken from [58].

A zero Hall plateau in σ_{XY} with a double-peak in σ_{XX}, and specifically both conductivity components dropping to 0, are a consequence of the sample being highly resistive during the plateau to plateau transition. The peak value of sheet resistance during the magnetization reversal for all 9 layers is plotted in Fig. 5.8c, and a resistivity here changes by at least (as the resistivity value for the thinnest layer is a lower bound) 5 orders of magnitude at this thickness range. The saturated value close to h/e^2 in the thicker limit is consistent with the 3D scaling behavior, where there is no insulating state when σ_{XY}=0 and σ_{XX} takes a peak value close to e^2/h.

A sampling of corresponding conductivity scaling plots for layers of different thicknesses is depicted in Fig. 5.8d, and a very clear smooth evolution between the two distinct regimes is observed. Indeed when the thickness is reduced, we observe a transition of the

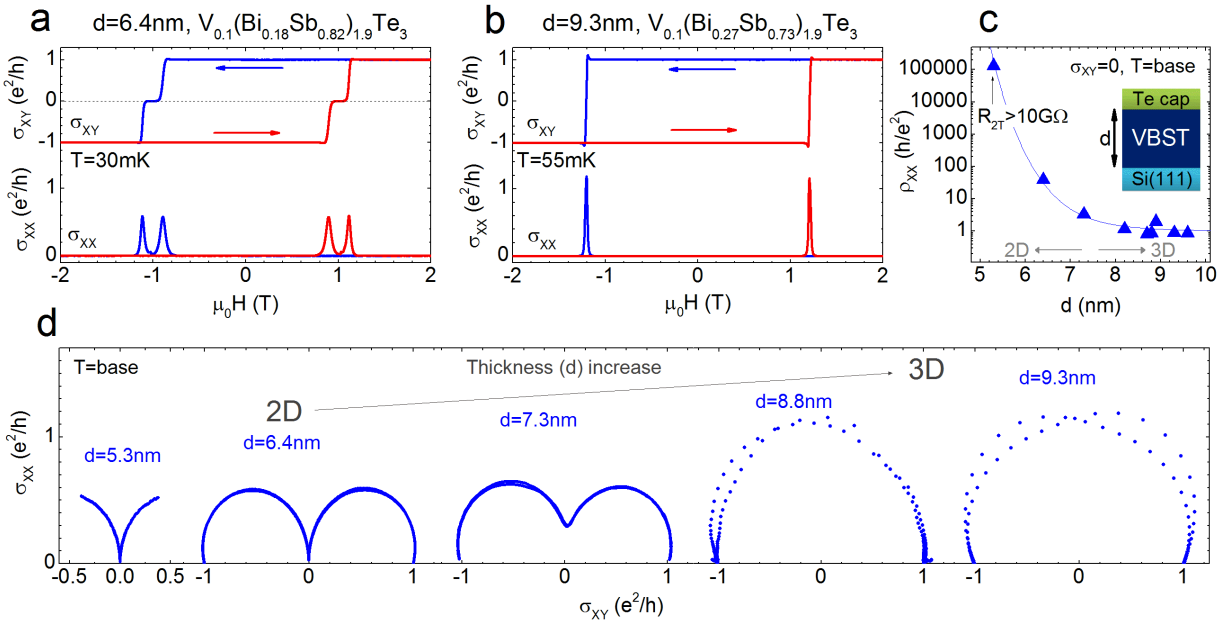

Figure 5.8: a) External magnetic field dependence of the conductivity tensor elements for a device patterned from a 6.4 nm thick $V_{0.1}(Bi_{0.18}Sb_{0.82})_{1.9}Te_3$ film at temperature 30 mK. b) same, for a 9.3nm thick $V_{0.1}(Bi_{0.27}Sb_{0.73})_{1.9}Te_3$ film at temperature 55 mK. c) Base temperature thickness dependence of the sheet resistance during the magnetization reversal at σ_{xy}=0 for all samples. VBST stands for $(V,Bi,Sb)_2Te_3$, and the solid line is a guide to the eye. The sheet resistance for the 5.3 nm thick film is an estimated lower boundary. d) Thickness evolution of the scaling behavior for samples ranging in thickness from the 2D integer quantum Hall to the 3D limit. Figure taken from [58].

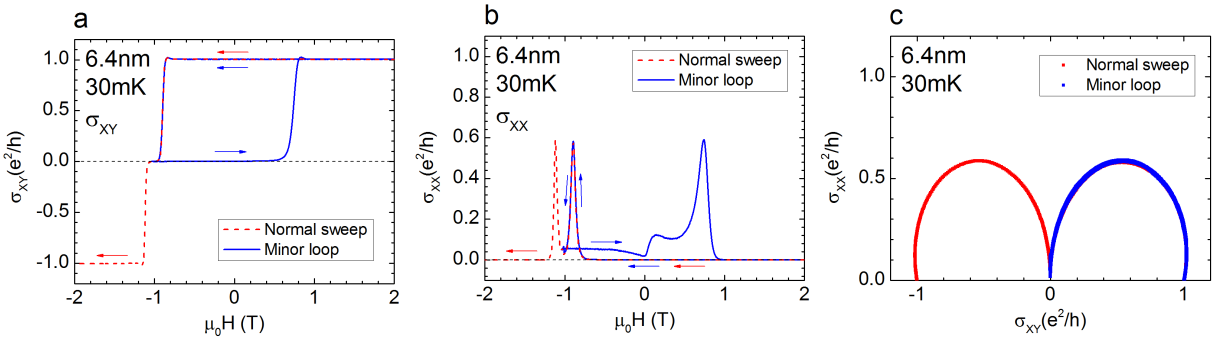

Figure 5.9: Minor loop transport data for a 6.4 nm thick film. a) Hall conductivity data representing a full magnetic field sweep in one direction (red color), and a minor loop (blue color). b) Longitudinal conductivity representing a full magnetic field sweep in one direction (red color), and a minor loop (blue color). c) Scaling behavior calculated from the data in (a) and (b). Colored arrows show the sweep direction. Figure taken from [58].

scaling diagram into a regime with two semicircles with radii $e^2/2h$ and centers located at ($\pm e^2/2h$,0), consistent with a behavior expected from an ordinary integer QHE, in the absence of axion electrodynamics.

Interestingly a 2D sample (6.4 nm thick) exhibiting a zero Hall plateau, reveals clear minor loop properties. This is plotted in Fig. 5.9. This mimics very well a minor loop behavior that was reported in magnetic hetero-structures, and claimed to provide evidence for selective magnetization reversal of the top and bottom surface components [27, 70, 29]. Here an identical behavior is observed in a uniformly doped thin film without any axion physics.

We also found that protective capping of the film affects the results of such conductivity scaling analysis. When a nominally 3D layer is grown without the protective Te cap, the scaling behavior tends to transition towards a 2D regime, the longer the surface is exposed to ambient conditions. All of this suggests that the layer surface is degrading, thus effectively reducing the thickness, pushing the film towards the 2D limit. Scaling plots from a couple of such uncapped nominally 3D films can be found in the appendix.

5.4 Detailed temperature analysis in 2D and 3D regime.

In order to map a larger part of the conductivity scaling phase diagram, the same magnetic field driven scaling analysis are performed at a wide range of temperatures from the base temperature of the dilution refrigerator to about 1 K. Fig 5.10 shows magneto-resistivity data collected at a variety of temperatures and at the optimal gate voltage (for charge neutrality) from 6 of the samples from the thickness series, 3 samples in the 2D limit and 3 samples in the 3D limit. In the case of the thinnest film (5.3 nm thick) a two-terminal resistance is analyzed instead, due to film resistance being too high for proper four-terminal measurements.

A fundamental difference in the temperature evolution of the scaling behavior between the layers in both 2D and 3D limits is visible in Fig. 5.11a-b, where magnetic-field driven scaling diagrams are plotted for a 2D 6.4 nm thick film (Fig. 5.11a), and a 3D 9.3 nm thick film (Fig. 5.11b).

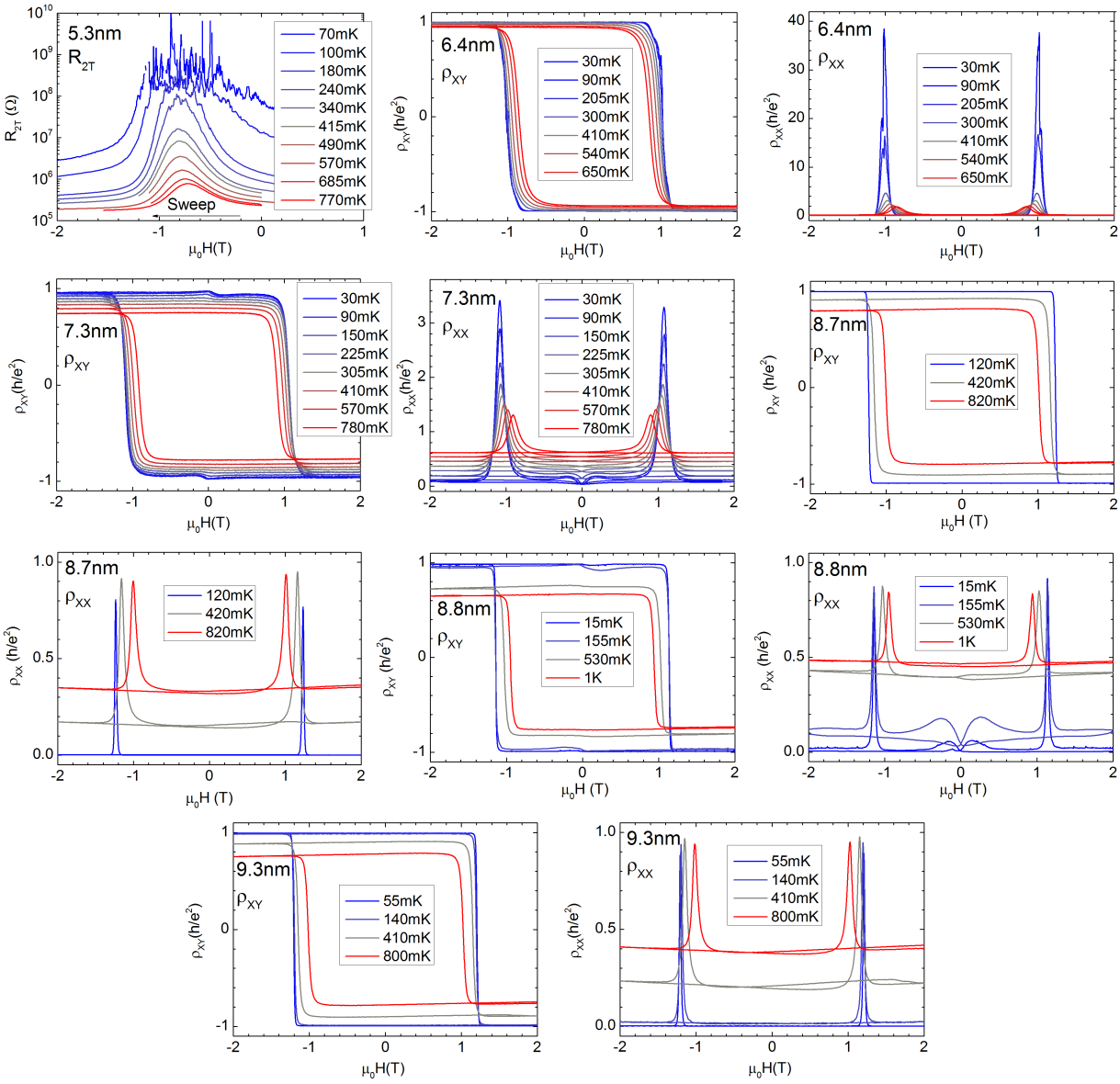

Figure 5.10: Magneto-resistivity data for a wide range of temperature values, for 6 of the samples from the thickness series. For the most insulating 5.3 nm thick films two-terminal resistance is analyzed. Figure adapted from [58].

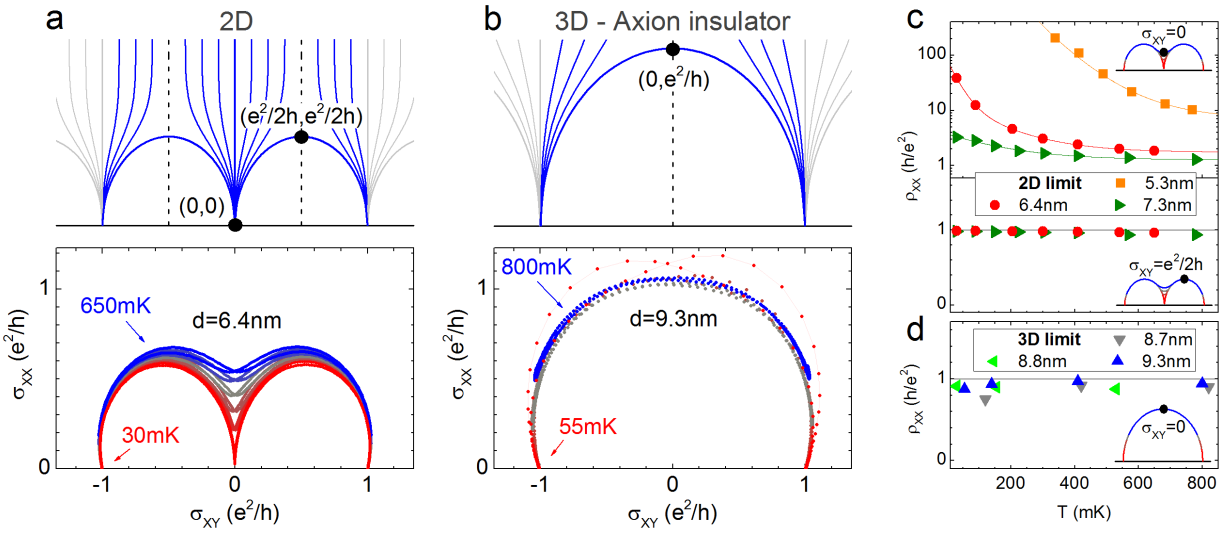

Figure 5.11: a) (top) Schematic of a global conductivity tensor flow diagram for the integer quantum Hall effect with dots marking the points used in the temperature dependence analysis. The scale on the axes matches the data panel below, (bottom) experimental magnetic field driven scaling diagram for a 6.4 nm thick film. The red color corresponds to a temperature of 30 mK and blue to 650 mK, with the intermediate values being 205 mK, 300 mK, 410 mK, and 540 mK. b) (top) Schematic of a global conductivity tensor flow diagram for Dirac fermions on two parallel topological interfaces, (bottom) experimental magnetic field driven scaling diagram for a 9.3 nm thick film. The red color corresponds to temperature 55 mK and blue to 800 mK, with intermediate values being 140 mK and 410 mK. c) Temperature dependence of film resistivity at σ_{xy}=0 and σ_{xy}=e^2/2h for the layers in the 2D limit. The data for the 5.3 nm thick film is extracted from a two-terminal resistance measurement. d) Temperature dependence of film resistivity when σ_{xy}=0 for the layers in the 3D axion limit. Solid lines in (c) and (d) are guides to the eye. The schematics inset to panel c) and d) indicate with a dot the point in the scaling diagram that is being plotted in the main figure. Figure taken from [58].

These differences are best appreciated when analyzing the longitudinal resistivity values for all 6 films in the vicinity of the characteristic points depicted in the flow diagram schematics in Fig. 5.11a-b on top. In a 2D limit (Fig. 5.11c) the trajectory towards the point (0,0) is exemplified by a clear thermally activated evolution of ρ_{XX} when σ_{xy}=0. A completely different temperature dependence is visible in the same layers when σ_{xy}=e^2/2h. Then the value is nearly temperature independent and always close to h/e^2, implying a critically delocalized electron state, or a singular point in the diagram [63].

When the evolution of ρ_{XX} is investigated when σ_{xy}=0 in the 3D limit, the value of longitudinal resistivity is temperature independent, and always close to h/e^2. This implies that the observed singular point in the scaling diagram (which here coincides with the

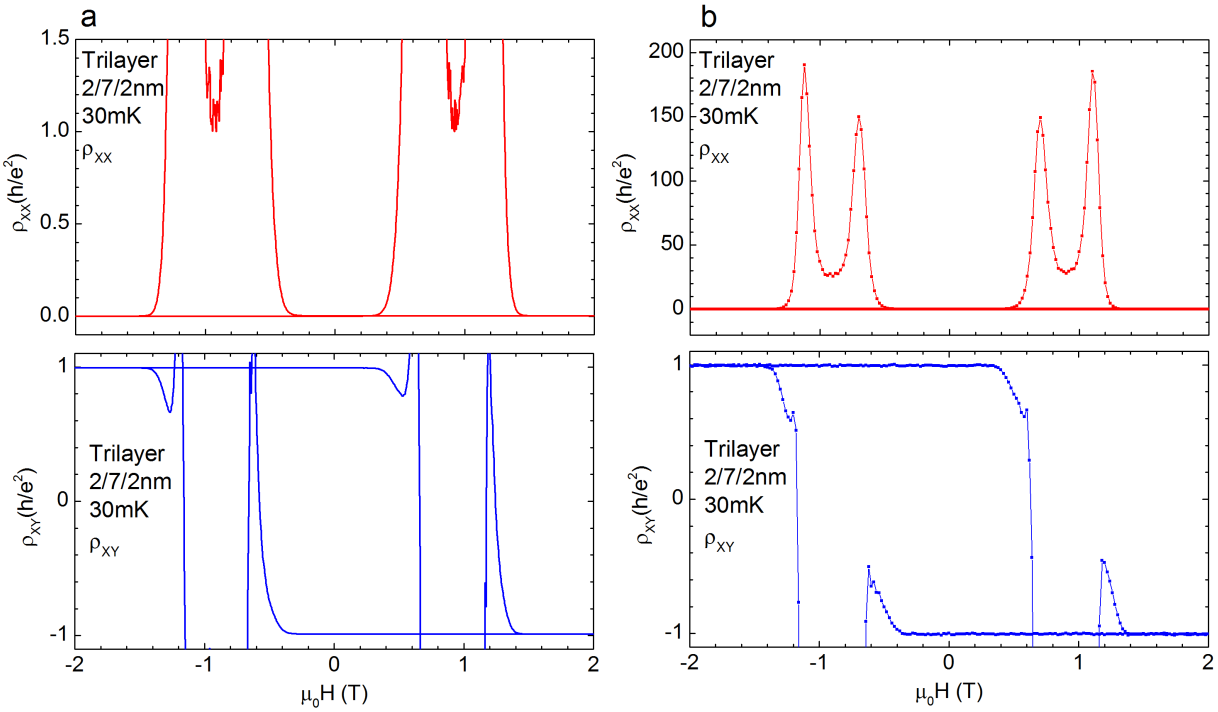

Figure 5.12: Magneto-resistivity values for a magnetic trilayer at base temperature. Total excitation voltage is 100 μV for each measurement. The measurement in (a) is at 13.7 Hz excitation voltage frequency with a series 9.9 kΩ reference resistor, in order to capture the quantum anomalous Hall plateau regime. Measurement in (b) is at a frequency of 2 Hz with a series 997 kΩ reference resistor, in order to better resolve the high resistance regime during the plateau to plateau transition. Figure adapted from [58].

σ_{xy} coordinate of the semicircle center) is shifted from ($e^2/2h$,$e^2/2h$) to (0,e^2/h) upon the 2D-3D transition, consistent with our interpretation. This clearly implies that the two regimes belong to fundamentally different quantum anomalous Hall classes.

5.5 Magneto-transport data from magnetic hetero-structures of topological insulators - behavior equivalent to a 2D system.

Another proposed approach to achieve the topological half-integer σ_{xy}=$e^2/2h$ quantization uses magnetic hetero-structures of topological insulators. Initial proposal involved interfacing a 3D TI layer with two (out of plane) ferromagnetic insulators, which have different coercive fields. Then by sweeping external magnetic field, both ferromagnetic

layers are aimed to be aligned antiparallel, resulting in the topological contribution from both surfaces canceling out, and resulting in a σ_{xy} plateau with a value 0 [26]. This has been dubbed the "zero Hall plateau" (ZHP), and recently has been a subject of extensive experimental efforts [27, 70, 29, 71].

The attempts to experimentally realize such ideas involve the manipulation of a magnetic doping profile within a single TI layer. A so called trilayer structure is grown, where the two magnetically doped TI layers sandwich a non-magnetic TI layer, and an attempt to selectively manipulate the two magnetic layers is made. A ZHP in such hetero-structures was observed by a couple of groups, with a claim of realization of an axion insulator [27, 70, 29].

Fig. 5.12 shows measurements of longitudinal and Hall resistivities collected at 30 mK from a magnetic trilayer consisting of two 2 nm thick layers of $V_{0.1}(Bi_{0.31}Sb_{0.69})_{1.9}Te_3$ separated by a 7 nm thick $(Bi_{0.31}Sb_{0.69})_2Te_3$ layer. The sample exhibits a perfect AH resistance quantization at zero external magnetic field.

A first major problem with measurements of magneto-transport in such systems becomes apparent when ρ_{xy} and ρ_{xx} are attempted to be measured during the magnetization reversal, in the regime where an antiparallel magnetization alignment should occur. The sample resistance goes to extremely high values, to the point that any four-terminal measurements become invalid. This is exemplified by the resulting measurement during the magnetization reversal in Fig. 5.12, where in a voltage biased scheme the current vanishes, resulting in a division by 0 in resistivity calculation. In a practical scenario the resulting value of four-terminal resistance is fully determined by the circuit considerations and experimental artifacts. This highlights a fundamental issue with this approach, as in an insulator only a two-terminal measurement is properly defined, and a two-terminal measurement of extremely high resistance can't differentiate the result from a trivial insulator without any axion physics.

Fig. 5.13a shows the calculated magneto-conductivity data, where four-terminal measurements where the sample resistance exceeded 10 MΩ were omitted. A clear ZHP-like feature is visible in σ_{xy} and a double peak shape in σ_{xx}. Importantly when such data is directly plotted in form of the scaling diagram (Fig. 5.13b), it follows a fundamental scaling identical to that of a 2D system and the overall appearance of the conductivity data is extremely similar to regular 2D layers (such as in Fig. 5.8).

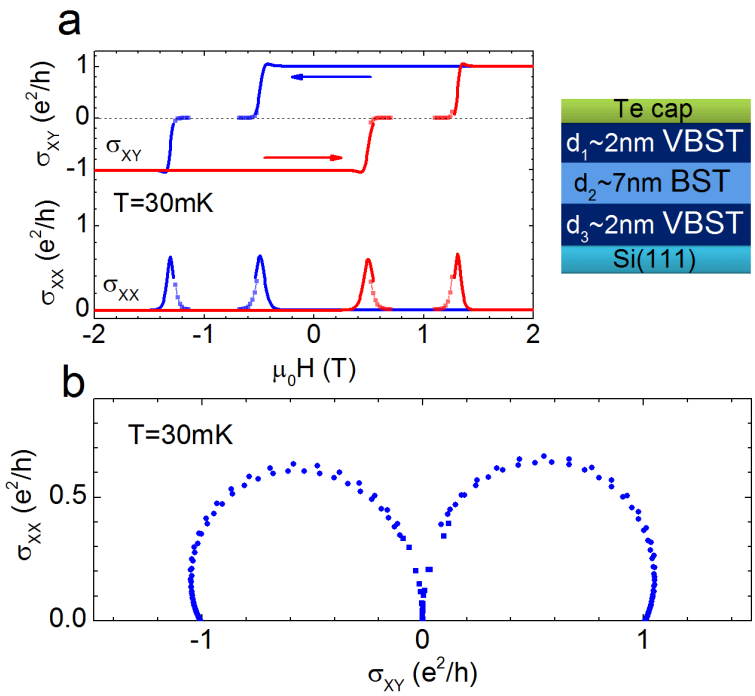

Figure 5.13: a) Hall and longitudinal magneto-conductivity data collected at a temperature of 30 mK for a sample patterned from a magnetic trilayer. A schematic of the hetero-structure is given on the right. VBST stands for $V_{0.1}(Bi_{0.31}Sb_{0.69})_{1.9}Te_3$, and BST stands for $(Bi_{0.31}Sb_{0.69})_2Te_3$. The plateau region where the sample resistance exceeds 10 MΩ cannot be resolved in this measurement configuration. b) The conductivity tensor scaling behavior of the data in (a). Figure taken from [58].

This implies that in terms of the experimental observables, it is impossible to distinguish the ZHP that may result from an antiparallel allignment of "top"-"bottom" magnetizations, from the ZHP observed in a 2D system that has a single magnetic component and no axion physics. Therefore an observation of the zero Hall plateau itself does not provide evidence for axion physics, and those earlier claims [27, 70, 29] require a revision.

Chapter 6

Outlook.

Despite already 8 years of extensive worldwide experimental and theoretical effort put into investigations of the QAHE, there are still open questions surrounding the underlying physics, both pertaining to the effect itself and to the materials that exhibit it. This should fuel the continuation of this research topic for the foreseeable future.

Further investigations into induced superconductivity in the QAHE materials need to be performed. So far the chiral Majorana fermion quasiparticle likely remains elusive [21, 22], and no direct evidence of supercurrent in quantum anomalous Hall edge channels have been reported. Fabrication and investigation of the hybrid devices such as Josephson junctions on a material exhibiting the QAHE is also planned for the near future.

Significant attention in the community has been recently put into attempts to increase the operational temperature of the QAHE. While our results obtained on the multi-terminal Corbino geometry [51] pinpoint a specific parameter that needs to be improved, the bulk resistivity, so far there seems to be no reliable way to achieve that in experiment. There have been reports of anomalous Hall resistance close to quantization at temperatures approaching 1 K, but being close is not enough to obtain a practical quantum resistance standard. These attempts involved both manipulation of structural parameters in Cr/V-doped $(Bi,Sb)_2Te_3$ class of materials [72, 73], and investigations of new material systems such as twisted bilayer graphene [74], and $MnBi_2Te_4$ [75]. While the improvements in temperature stability of the quatization is an obvious long term goal, there is still room for improvements in the precision measurement of quantization in our $(V,Bi,Sb)_2Te_3$ at base temperature of the dilution refrigerator, which is one of the topics we aim to focus on in the near future, continuing our collaboration with PTB.

Finally the influence of finite size effects on the QAHE, and related questions pertaining

to the "size" of the chiral edge channel remain mostly unknown. So far primarily macroscopic size devices (at least 10 μm in size) have been explored in the community, with only a handful of first results published recently on sub-μm size QAHE samples [76, 77, 78]. It turns out that the samples with size approaching the size of individual magnetic domains in the material, open a way to access transport properties of such individual domains. This has already revealed some interesting unexpected physics, such as macroscopic quantum tunneling of magnetization [77]. Indeed more detailed exploration of QAHE nanostructures is one of the topics that should be further explored in the near future.

Summary.

The subject of this thesis is the investigation of electronic transport properties of samples based on the magnetically doped topological insulator $(V,Bi,Sb)_2Te_3$ layers. Specifically, the main focus is on the anomalous Hall effect and the quantum anomalous Hall effect observed in this material system.

First a detailed analysis of the anomalous Hall effect is performed in a variety of heterostructures based on the V-doped $(Bi,Sb)_2Te_3$ material system, where the influence of a variety of parameters is investigated, such as gate voltage, temperature, magnetic layer thickness and magnetic doping level. The overall anomalous Hall response is found to reveal a phenomenology identical to the one previously attributed to magnetic skyrmion textures (topological Hall effect) in the literature. Our analysis however reveals that the origin of the observed signals is fundamentally different, and ties to the joint effect of two coexisting independent ferromagnetic components, each producing an anomalous Hall component of opposite sign.

The total anomalous Hall signal is found to change sign as a function of gate voltage, temperature, magnetic layer thickness and magnetic doping level. A rather complicated sign reversal with the temperature and gate voltage is quite easily explained, when the existence of two magnetic components is invoked. Specifically the sign change with gate voltage is a result of each component having a different dependence on the carrier density. The first anomalous Hall conductivity component is independent on the gate voltage, and the second component is significantly suppressed when electron conductivity turns on. This results in the overall signal sign change when both components are summed together.

Moreover both components are found to depend differently on temperature, with the first component vanishing with temperature faster than the second component (and therefore also producing a sign inversion when summed together), further indicating the coexistence of two ferromagnetic components with different Curie temperatures.

Based on the anomalous Hall sign inversion with the magnetic layer thickness, we

suggest that the first component originates in the bulk, and the second component at the surface of the material. A change in thickness of the magnetic layer changes the volume, while maintaining the surface area nearly unchanged (the Hall bar samples are laterally 3-4 orders of magnitude larger than the film thickness). Therefore based on this hypothesis, only one of the components (the bulk one) scales with the layer thickness, resulting in a sign inversion when the volume becomes sufficiently large and the bulk component amplitude exceeds that of the surface component. This remains a speculation at this stage, and a microscopic model will have to be developed to gain more understanding into the physical mechanism behind each component.

Next the quantum anomalous Hall effect in V-doped $(Bi,Sb)_2Te_3$ is investigated. A detailed material stoichiometry study is performed where both the Bi/Sb ratio and the V doping level are changed. A narrow parameter space is found where a perfect quantum anomalous Hall effect is observed.

The quality of quantum anomalous Hall effect in our samples is further validated by performing metrologically comprehensive precision measurements in collaboration with our partners from Physikalisch-Technische Bundesanstalt (PTB) Braunschweig. A portable cryogenic current comparator is transported from PTB to Würzburg and used on site in our lab. An optimized $(V,Bi,Sb)_2Te_3$ sample is placed in a dilution refrigerator and cooled down to 25 mK. Our experiments reveal a relative deviation from anomalous Hall resistance quantization at zero external magnetic field of 0.17 ± 0.25 ppm in our sample, still the most precise value obtained worldwide at the time of this publication. This proof of concept experiment may prove important in the context of recent redefinition of the SI unit system, where the unit of kilogram is defined based on the Planck constant. One of the experiments tracing the Kilogram to the Planck constant is the so called "Kibble balance", where an operational zero field quantum resistance standard would be useful in simplifying the Kibble experiment, due to a possibility to combine the quantum voltage and resistance standards into a single reference instrument.

Further investigations into the quantum anomalous Hall effect reveal that the chiral quantum anomalous Hall edge channels survive up to the Curie temperature of bulk ferromagnetism, and the quantization breakdown observed above 100 mK is solely a result of thermally activated parallel bulk conductance electrically shorting the edge channels. This result is achieved by means of careful non-local measurements on a specially developed multi-terminal Corbino geometry. This allows for a clear separation of current paths taken by charge carriers in the bulk and the chiral edge channel, resulting in non-local signals

that can be produced only by the chiral edge channels. We observe the edge channel contribution up to bulk Curie temperature of approx. 18 K. This sheds light on topological nature of the protection of those edge channels, and directly addresses a long standing open question in the community, namely why is the quantization limited to temperatures below 100 mK, and whether the anomalous Hall effect observed at higher temperatures is a result of ordinary anomalous Hall effect from the bulk states or the edge channel. Our analysis also establish the multi-terminal Corbino geometry as a powerful tool in investigations of the edge channels in topological materials, even in the presence of parallel bulk conducting channels.

Finally the electrodynamic properties of the quantum anomalous Hall state are investigated in great detail. Based on the universal conductivity tensor scaling analysis, we find the existence of two fundamentally distinct regimes of the quantum anomalous Hall state. Both limits can be accessed by tuning the magnetic topological insulator layer thickness.

When analysis is performed in the quantized transport regime (at base temperature of the dilution refrigerator), the thinner films (approx. 6 nm thick) reveal conductivity tensor element scaling consistent with that of an ordinary 2D electron gas. A plateau to plateau transition follows two semicircles with a radius of $e^2/2h$ and centers at ($\pm e^2/2h$,0). This behavior is well established in a variety of ordinary quantum Hall systems, and was previously observed in thin films of magnetic topological insulator exhibiting the quantum anomalous Hall effect.

In the same temperature regime, when the film thickness is increased, a smooth evolution towards a fundamentally different limit is observed. Thicker samples (at approx. 9 nm) follow scaling that is consistent with that predicted for a so called "axion insulator". Nomura and Nagaosa predicted a scaling signature for an axion insulator where the position of the semicircle center is located at the conductivity plane origin (0,0). In their analysis the radius of the semicircle is $e^2/2h$, as a single isolated surface of a cylinder is considered, with a magnetization normal along the entire surface. When the same idea is adapted to a flat film geometry, we argue that "top" and "bottom" topological interfaces are each infinite radius limits of this theoretical cylinder, thus doubling the conductivity values expected in experiment. The data we observe follows a single semicircle centered at (0,0) and a radius e^2/h, consistent with this prediction.

The temperature evolution of layers in 2D and 3D limits also reveals fundamentally distinct behavior. In a 2D limit the point (0,0) is found to be attractive, in opposition to the 3D limit where a singular point is observed when σ_{xy}=0, with σ_{xx} taking on values close

to e^2/h. In addition, in the 2D limit a singular point is found when σ_{xy}=$e^2/2h$, further indicating that upon the 2D-3D transition the singular point acquires a fractional shift, and along with it the semicircle scaling diagram center, from σ_{xy}=$e^2/2h$ to σ_{xy}=0. All of this provides a solid case for a solid state realization of axion electrodynamics.

Zusammenfassung.

Gegenstand dieser Arbeit ist die Untersuchung der elektronischen Transporteigenschafen magnetisch dotierter topologischer Insulator Proben basierend auf $(V,Bi,Sb)_2Te_3$ Schichten. Dabei liegt der Hauptfokus auf dem Anomalen-Hall-Effekt und dem Quanten-Anomalen-Hall-Effekt, die in diesem Materialsystem mit einer bemerkswerten Klarheit beobachtet werden.

Hierzu wurde zunächst eine detaillierte Analyse des Anomalen-Hall-Effekts an einer Vielzahl von Heterostrukturen, basierend auf dem V-dotierten $(Bi,Sb)_2Te_3$ Materialsystem, durchgeführt. Dabei wurde der Einfluss verschiedener Parameter, wie zum Beispiel Gatespannung, Temperatur, magnetische Schichtdicke und magnetischer Dotierungsgrad untersucht. Phämonemologisch ist das Verhalten der gemessenen Hall Kurven identisch mit dem in der Literatur beschriebenen topogischen Hall-Effekt magnetischer Skyrmion Texturen. Allerdings zeigt unsere Analyse, dass der Ursprung der beobachteten Signale grundlegend unterschiedlich und auf die Existenz zweier gemeinsam auftretender, unabhängiger ferromagnetischer Komponenten zurückzuführen ist, welche jeweils eine anomale Hall-Komponente mit entgegengesetztem Vorzeichen erzeugen.

Es zeigt sich, dass das Hall-Signal das Vorzeichen als eine Funktion der Gatespannung, der Temperatur, der magnetischen Schichtdicke und des magnetischen Dotierungsgrads ändert. Die komplexe Umkehr des Vorzeichens in Abhängigkeit von der Temperatur und Gatespannung kann unter Annahme der Existenz zweier unabhängiger magnetischer Phasen auf einfache Art und Weise erklärt werden. Der Voreichenwechsel in Abhängigkeit von der Gatespannung resultiert aus den unterschiedlichen Ladungsträgerdichten der einzelnen Komponenten. Während die erste Komponente des Hall Leitfähigkeit gatespannungsunabhängig ist, wird die zweite bei Zunahme der Elektronenleitfähigkeit signifikant unterdrückt. Dies führt zu einem Vorzeichenwechsel des Gesamtsignals.

Zusätzlich zeigt sich ein unterschiedliches Temperaturverhalten beider Komponenten, wobei mit steigender Temperatur die erste Komponente schneller verschwindet als die

zweite Komponente was wiederum zu einem Vorzeichenwechsel führt. Dieses Verhalten weist auf die Koexistenz zweier ferromagnetischer Komponenten mit unterschiedlichen Curie-Temperaturen hin.

Beim Vorzeichenwechsel des (anomalen) Hall-Effekt in Abhängigkeit der magnetischen Schichtdicke, vermuten wir, dass die erste Komponente ihren Ursprung im Volumen und die zweite Komponente an der Oberfläche des Materials hat. Eine Änderung der Dicke der magnetischen Schicht ändert das Volumen, während die Oberfläche nahezu unverändert beibehalten bleibt. (Die Hallbar-Proben sind lateral um 3-4 Größenordnungen größer als die Schichtdicke). Ausgehend von dieser Hypothese, kommt es zu einem Vorzeichenwechsel, wenn die Änderung des Volumens ausreichend großist und die Amplitude der Volumenkomponente die der Oberflächenkomponente übersteigt. Allerdings bleibt dies eine reine Spekulation, bis ein mikroskopisches Modell entwickelt wird, das es ermöglicht, ein besseres Verständnis der physikalischen Mechanismen der jeweiligen Komponenten zu entwickeln.

Einen weiteren Forschungsschwerpunkt stellt die Untersuchung des Quanten-Anomale-Hall-Effekt in $(V,Bi,Sb)_2Te_3$. Eine detaillierte Studie der Materialzusammensetzung wurde durchgeführt, bei welcher sowohl das Bi/Sb-Verhältnis, als auch die V-Dotierkonzentration geändert werden. Dabei zeigt sich ein schmaler Parameterraum in dem ein perfekter Quanten-Anomaler-Hall-Effekt beobachtet werden kann.

Die Qualität des Quanten-Anomalen-Hall-Effekts in unseren Proben wurde durch umfassende metrologische Präzisionsmessungen in Zusammenarbeit mit unseren Partnern der Pysikalisch-Technischen Bundesanstalt (PTB) bestätigt. Ein tragbarer Kryostromkomparator wurde dafür von der PTB nach Würzburg transportiert und in unserem Labor vor Ort eingesetzt. Eine optimierte $(V,Bi,Sb)_2Te_3$ Probe wurde in einem Mischungskryostaten eingebaut und auf 25 mK abgekühlt. Unsere Experimente zeigen eine relative Abweichung von der anomalen Hallwiderstandsquantisierung bei Null Magnetfeld von 0.17 ± 0.25 ppm, was zum Zeitpunkt der Veröffentlichung der weltweit genaueste, gemessene Wert war und noch immer ist. Dieses Experiment beweist die Machbarkeit, d.h., die Erzeugung eines präzise quantisierten Hall-Zustands ohne externes Magnetfeld, und kann sich im Zusammenhang mit der aktuellen Neudefinition des SI-Einheitensystems, bei dem die Einheit des Kilograms auf Grundlage der Planck-Konstante definiert wird, als wichtig herausstellen. Eines der Experimente die das Kilogramm auf die Planck Konstante zurückführen soll, ist die sogenannte "Kibble-Waage", bei der ein funktionsfähiger Nullfeld-Quantenwiderstandsstandard nützlich wäre, um das Kibbleexperiment, durch die Kombination des quan-

tisierten Spannungs- und Widerstandsstandard in einem einzigen Referenzinstrument zu vereinfachen.

Weitere Untersuchungen zum anomalen Quanten-Hall-Effekt zeigen, dass die chiralen Quanten anomalen Hall Randkanäle bis zur Curie-Temperatur des Volumen- Ferromagnetismus bestehen bleiben, wobei der oberhalb von 100 mK beobachtete Zusammenbruch der Quantisierung allein durch thermisch aktivierte parallele Volumenleitfähigkeit verursacht wird, die die Randkanäle elektrisch kurzschließt. Dieses Ergebnis wurde durch sorgfältige nicht-lokale Messungen, mit einer speziell dafür entwickelten multi-terminalen Corbino-Geometrie erzielt. Dies ermöglicht eine klare Trennung der Strompfade, die von den Ladungsträgern des Volumens und den chiralen Randkanälen verwendet werden und ermöglicht die Identifikation von des nicht-lokalen Signals durch Rändkanäle. Wir können den Beitrag der Randkanäle bis zur Curie-Temperatur von ca. 18 K beobachten. Dies gibt Aufschluss über die topologische Natur dem Schutz dieser Zustände und adressiert direkt eine in diesem Themengebiet lange diskutierte Fragen nach der Beschränkung der beobachteten Quantisierung auf Temperaturen, warum die Quantisierung auf Temperaturen unter 100 mK und der Zuordnung des anomalen Hall-Effekts bei höheren Temperaturen bezüglcih Rand- oder Volumenzustände. Zudem etabliert unsere Analyse die multiterminale Corbino-Geometrie als ein leistungsfähiges Werkzeug bei der Untersuchung von Randkanälen in topologischen Materialien, sogar in Gegenwart von Kanälen paralleler Volumenleitfähigkeit.

Abschließend werden die elektrodynamischen Eigenschaften des Quanten-Anomalen-Hall-Effekts eingehend untersucht. Basierend auf der universellen Leitfähigkeitstensorskalierungsanalyse fanden wir die Existenz zweier fundamental unterschiedlichen Regime des Quanten-Hall-Anomalen-Effekts. Beide Grenzen können durch die Regelung der Schichtdicke des magnetischen topologischen Isolators erreicht werden. Wenn die Analyse im quantisierten Transportregime durchgeführt wird (bei der Basistemperatur eines Mischungskryostaten) zeigen die dünneren ca. 6 nm dicken Filme eine Leitfähigkeitstensorelementskalierung, die mit der eines gewöhnlichen 2D-Elekronengases konsistent ist. Ein Plateau zu Plateauübergang folgt zwei Halbkreise mit dem Radius $e^2/2h$ und den Mittelpunkten bei $(\pm e^2/2h,0)$. Dieses Verhalten tritt in unterschiedlichen gewöhnlichen Quanten-Hall-Systemen auf und wurde bereits in dünnen Filmen magnetischer topologischer Isolatoren beobachtet, die den anomalen Quanten-Hall-Effekt aufweisen.

Im selben Temperaturbereich, bei erhöhter Schichtdicke, kann eine kontinuierliche Entwicklung zu einem fundamental unterschiedlichen Verhalten hin beobachtet werden. Dickere

Proben (ca. 9 nm) folgen einer Skalierung, die konsistent mit der ist, die für einen so genannten "Axion Isolator" vorhergesagt wurde. Nomura und Nagaosa [25] haben eine Skalierungssignatur für einen Axion Isolator vorhergesagt, bei der die Position des Mittelpunktes des Halbkreises im Ursprung der Leitfähigkeitsebene (0,0) liegt. In deren Analyse ist der Radius des Halbkreises $e^2/2h$, wobei eine einzelne isolierte Oberfläche eines Zylinders in Betracht gezogen wird, welche eine senkrechte Magnetisierung entlang der gesamten Oberfläche aufweist. Bei der Adaptieren dieser Idee für die Geometrie eines flachen Films, bei der wir die obere und unter topologische Grenzschicht jeweils als Zylinder mit theoretisch unendlichen Radius betrachten, wäre eine Verdopplung der Leitfähigkeitswerde in einem Experiment zu erwarten. Die Daten, die von uns gemessen wurden, zeigen einen einzelnen Halbkreis mit Mittelpunkt bei (0,0) und einem Radius von e^2/h und sind daher konsistent mit dieser Vorhersage.

Bemerkenswert ist, dass 2D und 3D Schichten ein fundamental unterschiedliches Temperaturverhalten zeigen. Im 2D Limit erscheint der Punkt (0,0) anziehend, während er im 3D Fall singulär ist und σ_{xy} und σ_{xx} die Werte 0 und e^2/h annehmen. Zudem wird für σ_{xy}=$e^2/2h$ ein singulärer Punkt im 2D Limit beobachtet, der im Fall des Übergang von 2D nach 3D eine Verschiebung erfährt, wobei sich das Zentrum des Halbkreises von σ_{xy}=$e^2/2h$ nach σ_{xy}=0 ändert. All dies ist eine handfester Nachweis der Realisierung von Axion-Elektrodynamik in einem Festkörpersystem.

Appendices.

A Appendix 1 - Results of the Landauer-Büttiker modeling on the Corbino.

Here I provide the equations obtained from Landauer-Büttiker modelling performed in chapter 4 for the multi-terminal Corbino geometry. The equations describe evolution of potential on each contact as a function of the model parameters, normalized to the bias voltage, for a variety of source-drain configurations.

A.1 Bias A-1

Bias voltage applied to contact A, and contact 1 grounded. Potentials normalized to a voltage applied to contact A. Positive magnetization direction M+ (matrix 4.1) with the contact/lead resistance. Both β and $1/R_B$ larger than 0.

$$R_{A1,A1} = \frac{h}{e^2}\frac{3\beta + 1 + 4/R_B}{4(\beta + 1/R_B)(1 + 1/R_B)} + 2R_C \tag{6.1}$$

$$V_{A,A1(M+)} = 1 \tag{6.2}$$

$$V_{B,A1(M+)} = \frac{1}{R_{A1,A1}}\left(\frac{h}{e^2}\frac{2\beta + 3/R_B + 1}{4(\beta + 1/R_B)(1 + 1/R_B)} + R_C\right) \tag{6.3}$$

$$V_{C,A1(M+)} = \frac{1}{R_{A1,A1}}\left(\frac{h}{e^2}\frac{\beta + 2/R_B + 1}{4(\beta + 1/R_B)(1 + 1/R_B)} + R_C\right) \tag{6.4}$$

$$V_{D,A1(M+)} = \frac{1}{R_{A1,A1}} \left(\frac{h}{e^2} \frac{1}{4(\beta + 1/R_B)} + R_C \right) \tag{6.5}$$

$$V_{1,A1(M+)} = 0 \tag{6.6}$$

$$V_{2,A1(M+)} = \frac{1}{R_{A1,A1}} \left(\frac{h}{e^2} \frac{3}{4(1 + 1/R_B)} + R_C \right) \tag{6.7}$$

$$V_{3,A1(M+)} = \frac{1}{R_{A1,A1}} \left(\frac{h}{e^2} \frac{1}{2(1 + 1/R_B)} + R_C \right) \tag{6.8}$$

$$V_{4,A1(M+)} = \frac{1}{R_{A1,A1}} \left(\frac{h}{e^2} \frac{1}{4(1 + 1/R_B)} + R_C \right) \tag{6.9}$$

Bias voltage applied to contact A, and contact 1 grounded. Potentials normalized to a voltage applied to contact A. Negative magnetization M- (matrix 4.2) with the contact/lead resistance. Both β and $1/R_B$ larger than 0.

$$V_{A,A1(M-)} = 1 \tag{6.10}$$

$$V_{B,A1(M-)} = \frac{1}{R_{A1,A1}} \left(\frac{h}{e^2} \frac{1}{4(\beta + 1/R_B)} + R_C \right) \tag{6.11}$$

$$V_{C,A1(M-)} = \frac{1}{R_{A1,A1}} \left(\frac{h}{e^2} \frac{\beta + 2/R_B + 1}{4(\beta + 1/R_B)(1 + 1/R_B)} + R_C \right) \tag{6.12}$$

$$V_{D,A1(M-)} = \frac{1}{R_{A1,A1}} \left(\frac{h}{e^2} \frac{2\beta + 3/R_B + 1}{4(\beta + 1/R_B)(1 + 1/R_B)} + R_C \right) \tag{6.13}$$

$$V_{1,A1(M-)} = 0 \tag{6.14}$$

$$V_{2,A1(M-)} = \frac{1}{R_{A1,A1}} \left(\frac{h}{e^2} \frac{1}{4(1+1/R_B)} + R_C \right) \tag{6.15}$$

$$V_{3,A1(M-)} = \frac{1}{R_{A1,A1}} \left(\frac{h}{e^2} \frac{1}{2(1+1/R_B)} + R_C \right) \tag{6.16}$$

$$V_{4,A1(M-)} = \frac{1}{R_{A1,A1}} \left(\frac{h}{e^2} \frac{3}{4(1+1/R_B)} + R_C \right) \tag{6.17}$$

A.2 Bias A-C

Bias voltage applied to contact A, and contact C grounded. Potentials normalized to a voltage applied to contact A. Positive magnetization direction M+ (matrix 4.1) with the contact/lead resistance. Both β and $1/R_B$ larger than 0.

$$R_{AC,AC} = \frac{h}{e^2} \frac{1}{1-\beta} + 2R_C \tag{6.18}$$

$$V_{A,AC(M+)} = 1 \tag{6.19}$$

$$V_{B,AC(M+)} = \frac{1}{R_{AC,AC}} \left(\frac{h}{e^2} \frac{1/R_B + 2 - \beta}{2(1-\beta)(1+1/R_B)} + R_C \right) \tag{6.20}$$

$$V_{C,AC(M+)} = 0 \tag{6.21}$$

$$V_{D,AC(M+)} = \frac{1}{R_{AC,AC}} \left(\frac{h}{e^2} \frac{\beta + 1/R_B}{2(1-\beta)(1+1/R_B)} + R_C \right) \tag{6.22}$$

$$V_{1,AC(M+)} = \frac{1}{R_{AC,AC}} \left(\frac{h}{e^2} \frac{\beta + 2/R_B + 1}{2(1-\beta)(1+1/R_B)} + R_C \right) \tag{6.23}$$

$$V_{2,AC(M+)} = \frac{1}{2} \tag{6.24}$$

$$V_{3,AC(M+)} = \frac{1}{R_{AC,AC}} \left(\frac{h}{e^2} \frac{1}{2(1+1/R_B)} + R_C \right) \tag{6.25}$$

$$V_{4,AC(M+)} = \frac{1}{2} \tag{6.26}$$

Bias voltage applied to contact A, and contact C grounded. Potentials normalized to a voltage applied to contact A. Negative magnetization M- (matrix 4.2) with the contact/lead resistance. Both β and $1/R_B$ larger than 0.

$$V_{A,AC(M-)} = 1 \tag{6.27}$$

$$V_{B,AC(M-)} = \frac{1}{R_{AC,AC}} \left(\frac{h}{e^2} \frac{\beta + 1/R_B}{2(1-\beta)(1+1/R_B)} + R_C \right) \tag{6.28}$$

$$V_{C,AC(M-)} = 0 \tag{6.29}$$

$$V_{D,AC(M-)} = \frac{1}{R_{AC,AC}} \left(\frac{h}{e^2} \frac{1/R_B + 2 - \beta}{2(1-\beta)(1+1/R_B)} + R_C \right) \tag{6.30}$$

$$V_{1,AC(M-)} = \frac{1}{R_{AC,AC}} \left(\frac{h}{e^2} \frac{\beta + 2/R_B + 1}{2(1-\beta)(1+1/R_B)} + R_C \right) \tag{6.31}$$

$$V_{2,AC(M-)} = \frac{1}{2} \tag{6.32}$$

$$V_{3,AC(M-)} = \frac{1}{R_{AC,AC}} \left(\frac{h}{e^2} \frac{1}{2(1+1/R_B)} + R_C \right) \tag{6.33}$$

$$V_{4,AC(M-)} = \frac{1}{2} \tag{6.34}$$

A.3 Bias A-3

Bias voltage applied to contact A, and contact 3 grounded. Potentials normalized to a voltage applied to contact A. Positive magnetization direction M+ (matrix 4.1) with the contact/lead resistance. Both β and $1/R_B$ larger than 0.

$$R_{A3,A3} = \frac{h}{e^2}\frac{(2/R_B + 1 + \beta)^2}{4(1-\beta)(\beta + 1/R_B)(1 + 1/R_B)} + 2R_C \tag{6.35}$$

$$V_{A,A3(M+)} = 1 \tag{6.36}$$

$$V_{B,A3(M+)} = \frac{1}{R_{A3,A3}}\left(\frac{h}{e^2}\frac{2/R_B + 1 + \beta}{4(1-\beta)(\beta + 1/R_B)} + R_C\right) \tag{6.37}$$

$$V_{C,A3(M+)} = \frac{1}{R_{A3,A3}}\left(\frac{h}{e^2}\frac{2/R_B + 1 + \beta}{4(1 + 1/R_B)(\beta + 1/R_B)} + R_C\right) \tag{6.38}$$

$$V_{D,A3(M+)} = \frac{1}{R_{A3,A3}}\left(\frac{h}{e^2}\frac{2/R_B^2 + 3\beta/R_B + 1/R_B + 2\beta^2 + 1 - \beta}{4(1-\beta)(\beta + 1/R_B)(1 + 1/R_B)} + R_C\right) \tag{6.39}$$

$$V_{1,A3(M+)} = \frac{1}{R_{A3,A3}}\left(\frac{h}{e^2}\frac{2/R_B + 1 + \beta}{2(1-\beta)(1 + 1/R_B)} + R_C\right) \tag{6.40}$$

$$V_{2,A3(M+)} = \frac{1}{R_{A3,A3}}\left(\frac{h}{e^2}\frac{2/R_B + 1 + \beta}{4(1-\beta)(1 + 1/R_B)} + R_C\right) \tag{6.41}$$

$$V_{3,A3(M+)} = 0 \tag{6.42}$$

$$V_{4,A3(M+)} = \frac{1}{R_{A3,A3}}\left(\frac{h}{e^2}\frac{2/R_B - \beta + 3}{4(1-\beta)(1 + 1/R_B)} + R_C\right) \tag{6.43}$$

Bias voltage applied to contact A, and contact 3 grounded. Potentials normalized to a

voltage applied to contact A. Negative magnetization M- (matrix 4.2) with the contact/lead resistance. Both β and $1/R_B$ larger than 0.

$$V_{A,A3(M-)} = 1 \tag{6.44}$$

$$V_{B,A3(M-)} = \frac{1}{R_{A3,A3}}\left(\frac{h}{e^2}\frac{2/R_B^2 + 3\beta/R_B + 1/R_B + 2\beta^2 + 1 - \beta}{4(1-\beta)(\beta + 1/R_B)(1 + 1/R_B)} + R_C\right) \tag{6.45}$$

$$V_{C,A3(M-)} = \frac{1}{R_{A3,A3}}\left(\frac{h}{e^2}\frac{2/R_B + 1 + \beta}{4(1 + 1/R_B)(\beta + 1/R_B)} + R_C\right) \tag{6.46}$$

$$V_{D,A3(M-)} = \frac{1}{R_{A3,A3}}\left(\frac{h}{e^2}\frac{2/R_B + 1 + \beta}{4(1-\beta)(\beta + 1/R_B)} + R_C\right) \tag{6.47}$$

$$V_{1,A3(M-)} = \frac{1}{R_{A3,A3}}\left(\frac{h}{e^2}\frac{2/R_B + 1 + \beta}{2(1-\beta)(1 + 1/R_B)} + R_C\right) \tag{6.48}$$

$$V_{2,A3(M-)} = \frac{1}{R_{A3,A3}}\left(\frac{h}{e^2}\frac{2/R_B - \beta + 3}{4(1-\beta)(1 + 1/R_B)} + R_C\right) \tag{6.49}$$

$$V_{3,A3(M-)} = 0 \tag{6.50}$$

$$V_{4,A3(M-)} = \frac{1}{R_{A3,A3}}\left(\frac{h}{e^2}\frac{2/R_B + 1 + \beta}{4(1-\beta)(1 + 1/R_B)} + R_C\right) \tag{6.51}$$

A.4 Bias A-4

Bias voltage applied to contact A, and contact 4 grounded. Potentials normalized to a voltage applied to contact A. Positive magnetization direction M+ (matrix 4.1) with the

contact/lead resistance. Both β and $1/R_B$ larger than 0.

$$R_{A4,A4} = \frac{h}{e^2}\frac{2\beta + 1 + 3/R_B}{4(1-\beta)(\beta + 1/R_B)} + 2R_C \tag{6.52}$$

$$V_{A,A4(M+)} = 1 \tag{6.53}$$

$$V_{B,A4(M+)} = \frac{1}{R_{A4,A4}}\left(\frac{h}{e^2}\frac{\beta + 2/R_B + 1}{4(1-\beta)(\beta + 1/R_B)} + R_C\right) \tag{6.54}$$

$$V_{C,A4(M+)} = \frac{1}{R_{A4,A4}}\left(\frac{h}{e^2}\frac{1 + 1/R_B}{4(1-\beta)(\beta + 1/R_B)} + R_C\right) \tag{6.55}$$

$$V_{D,A4(M+)} = \frac{1}{R_{A4,A4}}\left(\frac{h}{e^2}\frac{1}{4(\beta + 1/R_B)} + R_C\right) \tag{6.56}$$

$$V_{1,A4(M+)} = \frac{1}{R_{A4,A4}}\left(\frac{h}{e^2}\frac{3}{4(1-\beta)} + R_C\right) \tag{6.57}$$

$$V_{2,A4(M+)} = \frac{1}{R_{A4,A4}}\left(\frac{h}{e^2}\frac{1}{2(1-\beta)} + R_C\right) \tag{6.58}$$

$$V_{3,A4(M+)} = \frac{1}{R_{A4,A4}}\left(\frac{h}{e^2}\frac{1}{4(1-\beta)} + R_C\right) \tag{6.59}$$

$$V_{4,A4(M+)} = 0 \tag{6.60}$$

Bias voltage applied to contact A, and contact 4 grounded. Potentials normalized to a voltage applied to contact A. Negative magnetization M- (matrix 4.2) with the contact/lead resistance. Both β and $1/R_B$ larger than 0.

$$V_{A,A4(M-)} = 1 \tag{6.61}$$

$$V_{B,A4(M-)} = \frac{1}{R_{A4,A4}}\left(\frac{h}{e^2}\frac{2\beta^2 + 3\beta/R_B - \beta + 1 + 1/R_B + 2/R_B^2}{4(1-\beta)(1+1/R_B)(\beta+1/R_B)} + R_C\right) \tag{6.62}$$

$$V_{C,A4(M-)} = \frac{1}{R_{A4,A4}}\left(\frac{h}{e^2}\frac{1+1/R_B}{4(1-\beta)(\beta+1/R_B)} + R_C\right) \tag{6.63}$$

$$V_{D,A4(M-)} = \frac{1}{R_{A4,A4}}\left(\frac{h}{e^2}\frac{2\beta+1+3/R_B}{4(\beta+1/R_B)(1+1/R_B)} + R_C\right) \tag{6.64}$$

$$V_{1,A4(M-)} = \frac{1}{R_{A4,A4}}\left(\frac{h}{e^2}\frac{2\beta+1+3/R_B}{4(1-\beta)(1+1/R_B)} + R_C\right) \tag{6.65}$$

$$V_{2,A4(M-)} = \frac{1}{R_{A4,A4}}\left(\frac{h}{e^2}\frac{1}{2(1-\beta)} + R_C\right) \tag{6.66}$$

$$V_{3,A4(M-)} = \frac{1}{R_{A4,A4}}\left(\frac{h}{e^2}\frac{1/R_B+3-2\beta}{4(1+1/R_B)(1-\beta)} + R_C\right) \tag{6.67}$$

$$V_{4,A4(M-)} = 0 \tag{6.68}$$

A.5 Bias A-D

Bias voltage applied to contact A, and contact D grounded. Potentials normalized to a voltage applied to contact A. Positive magnetization direction M+ (matrix 4.1) with the contact/lead resistance. Both β and $1/R_B$ larger than 0.

$$R_{AD,AD} = \frac{h}{e^2}\frac{3/R_B+4-\beta}{4(1-\beta)(1+1/R_B)} + 2R_C \tag{6.69}$$

$$V_{A,AD(M+)} = 1 \tag{6.70}$$

$$V_{B,AD(M+)} = \frac{1}{R_{AD,AD}} \left(\frac{h}{e^2} \frac{1/R_B + 2 - \beta}{2(1-\beta)(1+1/R_B)} + R_C \right) \tag{6.71}$$

$$V_{C,AD(M+)} = \frac{1}{R_{AD,AD}} \left(\frac{h}{e^2} \frac{1/R_B + 4 - 3\beta}{4(1-\beta)(1+1/R_B)} + R_C \right) \tag{6.72}$$

$$V_{D,AD(M+)} = 0 \tag{6.73}$$

$$V_{1,AD(M+)} = \frac{1}{R_{AD,AD}} \left(\frac{h}{e^2} \frac{3}{4(1-\beta)} + R_C \right) \tag{6.74}$$

$$V_{2,AD(M+)} = \frac{1}{R_{AD,AD}} \left(\frac{h}{e^2} \frac{2/R_B + 3 - \beta}{4(1-\beta)(1+1/R_B)} + R_C \right) \tag{6.75}$$

$$V_{3,AD(M+)} = \frac{1}{R_{AD,AD}} \left(\frac{h}{e^2} \frac{1/R_B + 3 - 2\beta}{4(1-\beta)(1+1/R_B)} + R_C \right) \tag{6.76}$$

$$V_{4,AD(M+)} = \frac{1}{R_{AD,AD}} \left(\frac{h}{e^2} \frac{3}{4(1+1/R_B)} + R_C \right) \tag{6.77}$$

Bias voltage applied to contact A, and contact D grounded. Potentials normalized to a voltage applied to contact A. Negative magnetization M- (matrix 4.2) with the contact/lead resistance. Both β and $1/R_B$ larger than 0.

$$V_{A,AD(M-)} = 1 \tag{6.78}$$

$$V_{B,AD(M-)} = \frac{1}{R_{AD,AD}} \left(\frac{h}{e^2} \frac{\beta + 1/R_B}{2(1-\beta)(1+1/R_B)} + R_C \right) \tag{6.79}$$

$$V_{C,AD(M-)} = \frac{1}{R_{AD,AD}} \left(\frac{h}{e^2} \frac{\beta + 1/R_B}{4(1-\beta)(1+1/R_B)} + R_C \right) \tag{6.80}$$

$$V_{D,AD(M-)} = 0 \tag{6.81}$$

$$V_{1,AD(M-)} = \frac{1}{R_{AD,AD}} \left(\frac{h}{e^2} \frac{2\beta + 1 + 3/R_B}{4(1-\beta)(1+1/R_B)} + R_C \right) \tag{6.82}$$

$$V_{2,AD(M-)} = \frac{1}{R_{AD,AD}} \left(\frac{h}{e^2} \frac{\beta + 2/R_B + 1}{4(1-\beta)(1+1/R_B)} + R_C \right) \tag{6.83}$$

$$V_{3,AD(M-)} = \frac{1}{R_{AD,AD}} \left(\frac{h}{e^2} \frac{1}{4(1-\beta)} + R_C \right) \tag{6.84}$$

$$V_{4,AD(M-)} = \frac{1}{R_{AD,AD}} \left(\frac{h}{e^2} \frac{1}{4(1+1/R_B)} + R_C \right) \tag{6.85}$$

B Appendix 2 - Magnetic field driven scaling diagrams from the uncapped layers.

Here I provide the magnetic field driven conductivity scaling diagrams obtained from samples grown without the protective Te cap.

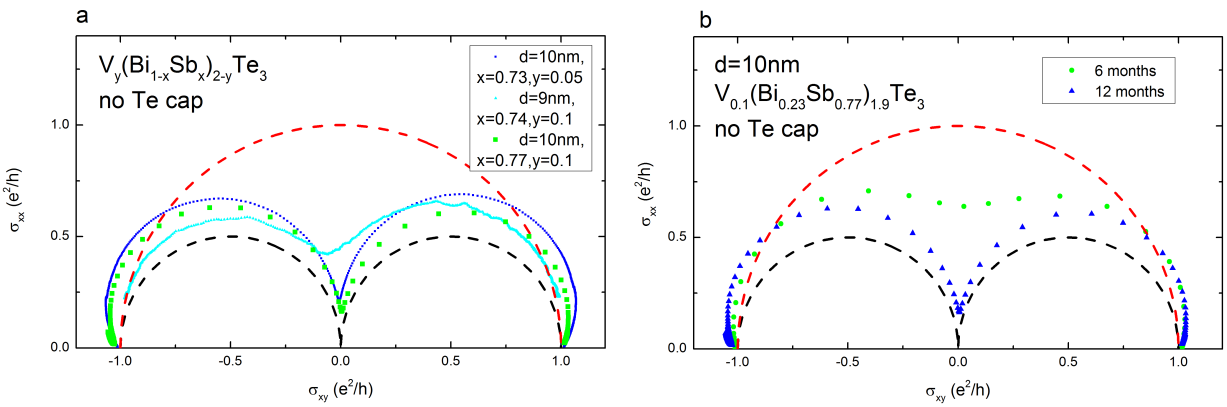

Figure B.1: a) Magnetic field driven scaling diagram collected at base temperature and optimal gate voltage from three MBE layers without the protective Te cap. b) The same kind of plots from two samples patterned from the same uncapped MBE layer, with one sample patterned 6 months and the other 12 months after the growth. The dashed lines represent the 2D (black) and 3D scaling (red).

C Appendix 3 - Temperature and gate voltage driven scaling diagrams.

Here I provide the temperature and gate voltage driven conductivity scaling diagrams obtained from a variety of samples.

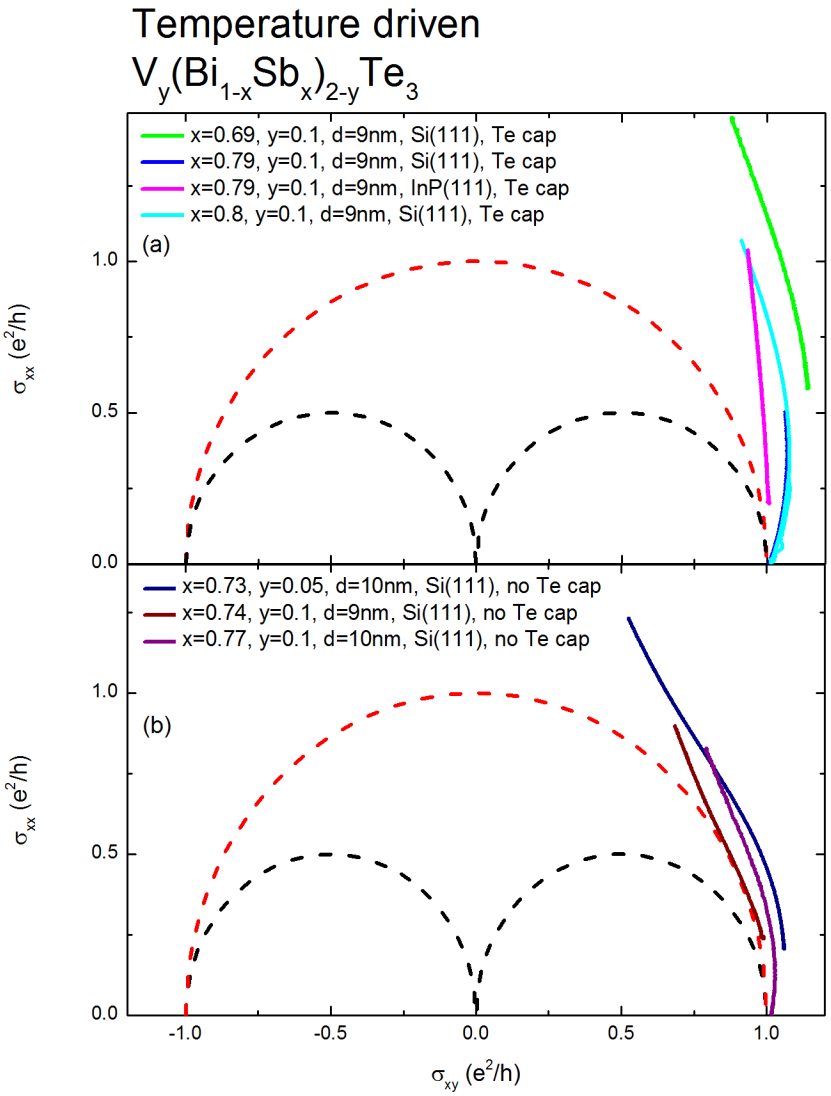

Figure C.1: Temperature driven conductivity scaling collected at zero external magnetic field and at an optimal gate voltage for quantized (or maximal) Hall resistance, obtained from samples with Te cap (a), and without Te cap (b). The dashed lines represent the 2D (black) and 3D scaling (red). Figure adapted from [28].

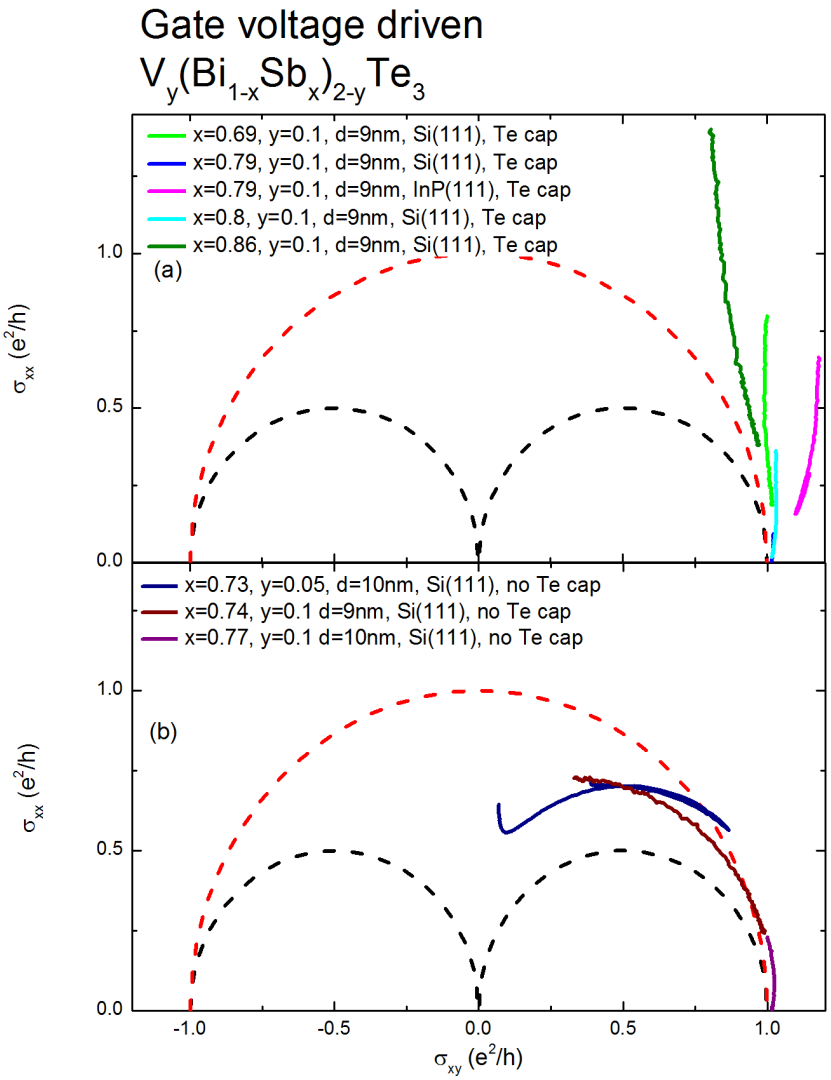

Figure C.2: Gate voltage driven conductivity scaling collected at zero external magnetic field in the magnetized state and at base temperature of the dilution refrigerator, obtained from samples with Te cap (a), and without Te cap (b). The dashed lines represent the 2D (black) and 3D scaling (red). Figure adapted from [28].

List of publications.

1. M. Winnerlein, S. Schreyeck, S. Grauer, S. Rosenberger, K. M. Fijalkowski, C. Gould, K. Brunner, and L. W. Molenkamp,
Physical Review Materials **1**, 011201(R) (2017),
DOI:10.1103/PhysRevMaterials.1.011201,
"Epitaxy and Structural Properties of $(V,Bi,Sb)_2Te_3$ Layers Exhibiting the Quantum Anomalous Hall Effect".

2. S. Grauer, K. M. Fijalkowski, S. Schreyeck, M. Winnerlein, K. Brunner, R. Thomale, C. Gould, and L. W. Molenkamp,
Physical Review Letters **118**, 246801 (2017),
DOI:10.1103/PhysRevLett.118.246801,
"Scaling of the Quantum Anomalous Hall Effect as an Indicator of Axion Electrodynamics".

3. M. Götz, K. M. Fijalkowski, E. Pesel, M. Hartl, S. Schreyeck, M. Winnerlein, S. Grauer, H. Scherer, K. Brunner, C. Gould, F. J. Ahlers, and L. W. Molenkamp,
Applied Physics Letters **112**, 072102 (2018),
DOI:10.1063/1.5009718,
"Precision Measurement of the Quantized Anomalous Hall Resistance at Zero Magnetic Field".

4. K. M. Fijalkowski, S. Grauer, S. Schreyeck, M. Winnerlein, K. Brunner, R. Thomale, C. Gould, and L. W. Molenkamp,
Proceedings: 2018 Conference on Precision Electromagnetic Measurements (CPEM 2018) (2018),
DOI:10.1109/CPEM.2018.8500974,
"On the Nature of the Quantum Anomalous Hall Effect".

5. M. Götz, K. M. Fijalkowski, E. Pesel, M. Hartl, S. Schreyeck, M. Winnerlein, S. Grauer, H. Scherer, K. Brunner, C. Gould, F. J. Ahlers, and L. W. Molenkamp,
Proceedings: 2018 Conference on Precision Electromagnetic Measurements (CPEM 2018) (2018),
DOI:10.1109/CPEM.2018.8501001,
"Zero-Field Quantized Anomalous Hall Resistance of $(Bi,Sb)_2Te_3$".

6. M. Kayyalha, D. Xiao, R. Zhang, J. Shin, J. Jiang, F. Wang, Y.-F. Zhao, R. Xiao, L. Zhang, K. M. Fijalkowski, P. Mandal, M. Winnerlein, C. Gould, Q. Li, L. W. Molenkamp, M. H. W. Chan, N. Samarth, and C.-Z. Chang,
Science **367**, 6473, 64-67 (2020),
DOI:10.1126/science.aax6361
"Absence of Evidence For Chiral Majorana Modes in Quantum Anomalous Hall-Superconductor Devices".

7. K. M. Fijalkowski, M. Hartl, M. Winnerlein, P. Mandal, S. Schreyeck, K. Brunner, C. Gould, and L. W. Molenkamp,
Physical Review X **10**, 011012 (2020),
DOI:10.1103/PhysRevX.10.011012,
"Coexistence of Surface and Bulk Ferromagnetism Mimics Skyrmion Hall Effect in a Topological Insulator".

8. K. M. Fijalkowski, N. Liu, M. Hartl, M. Winnerlein, P. Mandal, A. Coschizza, A. Fothergill, S. Grauer, S. Schreyeck, K. Brunner, M. Greiter, R. Thomale, C. Gould, and L. W. Molenkamp,
Physical Review B **103**, 235111 (2021),
DOI: 10.1103/PhysRevB.103.235111,
"Any Axion Insulator Must be a Bulk Three-Dimensional Topological Insulator".

9. K. M. Fijalkowski, N. Liu, P. Mandal, S. Schreyeck, K. Brunner, C. Gould, and L. W. Molenkamp,
Nature Communications **12**, 5599 (2021),
DOI:10.1038/s41467-021-25912-w,
"Quantum Anomalous Hall Edge Channels Survive up to the Curie Temperature".

Bibliography

[1] E. Hall, American Journal of Mathematics, vol. 2 , 3, 287-292 (1879), DOI:10.2307/2369245, "On a New Action of the Magnet on Electric Currents".

[2] E. Hall, Philosophical Magazine vol. 12, 157 (1881), DOI:10.1080/14786448108627086, "On the Rotational coefficient in nickel and cobalt".

[3] N. Nagaosa et al., Reviews of Modern Physics vol. 82, 1539 (2010), DOI:10.1103/RevModPhys.82.1539, "Anomalous Hall effect".

[4] K. v. Klitzing et al., Physical Review Letters vol. 45, 6, 49497 (1980), DOI:10.1103/PhysRevLett.45.494, "New Method for High-Accuracy Determination of the Fine-Structure Constant Based on Quantized Hall Resistance".

[5] K. S. Novoselov et al., Nature vol. 438, 197-200 (2005), DOI:10.1038/nature04233, "Two-dimensional gas of massless Dirac fermions in graphene".

[6] M. Koenig et al., Science vol. 318, 5851, 766-770 (2007), DOI:10.1126/science.1148047, "Quantum Spin Hall Insulator State in HgTe Quantum Wells".

[7] C-Z Chang et al., Science vol. 340, 6129, 167-170 (2013), DOI:10.1126/science.1234414, "Experimental observation of the quantum anomalous Hall effect in a magnetic topological insulator".

[8] B. D. Josephson, Physical Letters vol. 1, 251 (1962), DOI:10.1016/0031-9163(62)91369-0, "Possible new effects in the superconductive tunnelling".

[9] S. Shapiro, Physical Review Letters vol. 11, 80 (1963), DOI:10.1103/PhysRevLett.11.80, "Josephson currents in superconducting tunneling: The effect of microwaves and other observations".

[10] B. P. Kibble, Atomic Masses and Fundamental Constants, vol. 15, 1 (1976), DOI:10.1088/0026-1394/15/1/002, "A measurement of the gyromagnetic ratio of the proton by the strong field method".

[11] M. Stock, Metrologia vol. 50, R1 (2012), DOI:10.1088/0026-1394/50/1/R1, "Watt balance experiments for the determination of the Planck constant and the redefinition of the kilogram".

[12] M. Götz et al., Applied Physics Letters vol. 112, 072102 (2018), DOI:10.1063/1.5009718, "Precision measurement of the quantized anomalous Hall resistance at zero magnetic field".

[13] E. J. Fox et al., Physical Review B vol. 98, 075145 (2018), DOI:10.1103/PhysRevB.98.075145, "Part-per-million quantization and current-induced breakdown of the quantum anomalous Hall effect".

[14] C.-Z. Chang et al., Nature Materials vol. 14, 473-477 (2015), DOI:10.1038/nmat4204, "High-precision realization of robust quantum anomalous Hall state in a hard ferromagnetic topological insulator".

[15] S. Grauer et al., Physical Review B vol. 92, 201304(R) (2015), DOI:10.1103/PhysRevB.92.201304, "Coincidence of superparamagnetism and perfect quantization in the quantum anomalous Hall state".

[16] E. O. Lachman et al., Science Advances vol. 1, 10, e1500740 (2015), DOI:10.1126/sciadv.1500740, "Visualization of superparamagnetic dynamics in magnetic topological insulators".

[17] A. J. Bestwick et al., Physical Review Letters vol. 114, 187201 (2015), DOI:10.1103/PhysRevLett.114.187201, "Precise Quantization of the Anomalous Hall Effect near Zero Magnetic Field".

[18] K. M. Fijalkowski et al., Physical Review X vol. 10, 011012 (2020), DOI:10.1103/PhysRevX.10.011012, "Coexistence of surface and bulk ferromagnetism mimics skyrmion Hall effect in a topological insulator".

[19] K. Yasuda et al., Nature Physics vol. 12, 555 (2016), DOI:10.1038/nphys3671, "Geometrical Hall effects in topological insulator Heterostructures".

[20] X.-L. Qi et al., Physical Review B vol. 82, 184516 (2010), DOI:10.1103/PhysRevB.82.184516, "Chiral topological superconductor from the quantum Hall state".

[21] Q.-L. He et al., Science vol. 357, 6348, 294-299 (2017), DOI:10.1126/science.aag2792, "Chiral Majorana fermion modes in a quantum anomalous Hall insulator-superconductor structure".

[22] M. Kayyalha et al., Science vol. 367, 6473, 64-67 (2020), DOI:10.1126/science.aax6361, "Absence of evidence for chiral Majorana modes in quantum anomalous Hall-superconductor devices".

[23] F. Wilczek, Physical Review Letters vol. 58, 1799 (1987), DOI:10.1103/PhysRevLett.58.1799, "Two applications of axion electrodynamics".

[24] J. E. Kim et al., Reviews of Modern Physics vol. 82, 557 (2010), DOI:10.1103/RevModPhys.82.557, "Axions and the strong CP problem".

[25] K. Nomura et al., Physical Review Letters vol. 106, 166802 (2011), DOI:10.1103/PhysRevLett.106.166802, "Surface-quantized anomalous Hall current and the magnetoelectric effect in magnetically disordered topological insulators".

[26] J. Wang et al., Physical Review B vol. 92, 081107 (2015), DOI:10.1103/PhysRevB.92.081107, "Quantized topological magnetoelectric effect of the zero-plateau quantum anomalous Hall state".

[27] M. Mogi et al., Nature Materials vol. 16, 516 (2017), DOI:10.1038/nmat4855, "A magnetic heterostructure of topological insulators as a candidate for an axion insulator".

[28] S. Grauer et al., Physical Review Letters vol. 118, 246801 (2017), DOI:10.1103/PhysRevLett.118.246801, "Scaling of the quantum anomalous Hall effect as an indicator of axion electrodynamics".

[29] D. Xiao et al., Physical Review Letters vol. 120, 056801 (2018), DOI:10.1103/PhysRevLett.120.056801, "Realization of the axion insulator state in quantum anomalous Hall sandwich heterostructures".

[30] M. Z. Hasan et al., Reviews of Modern Physics vol. 82, 3045 (2010), DOI:10.1103/RevModPhys.82.3045, "Colloquium: Topological insulators".

[31] D. Hsieh et al., Nature vol. 452, 970-974 (2008), DOI:10.1038/nature06843, "A topological Dirac insulator in a quantum spin Hall phase".

[32] Y. Zhang et al., Nature Physics vol. 6, 584-588 (2010), DOI:10.1038/nphys1689, "Crossover of the three-dimensional topological insulator Bi_2Se_3 to the two-dimensional limit".

[33] M. Onoda et al., Physical Review Letters vol. 90, 206601 (2003), DOI:10.1103/PhysRevLett.90.206601, "Quantized anomalous Hall effect in two-dimensional ferromagnets: quantum Hall effect in metals".

[34] R. Yu et al., Science vol. 329, 5987, 61-64 (2010), DOI:10.1126/science.1187485, "Quantized anomalous Hall effect in magnetic topological insulators".

[35] C-X Liu et al., Physical Review Letters vol. 101, 146802 (2008), DOI:10.1103/PhysRevLett.101.146802, "Quantum anomalous Hall effect in HgMnTe quantum wells".

[36] J. G. Checkelsky et al., Nature Physics vol. 10, 10, 731-736 (2014), DOI:10.1038/nphys3053, "Trajectory of the anomalous Hall effect towards the quantized state in a ferromagnetic topological insulator".

[37] X. Kou, et al., Physical Review Letters vol. 113, 137201 (2014), DOI:10.1103/PhysRevLett.113.137201, "Scale-invariant quantum anomalous Hall effect in magnetic topological insulators beyond the two-dimensional Limit".

[38] A. Kandala et al., Nature Communications vol. 6, 7434 (2015), DOI:10.1038/ncomms8434, "Giant anisotropic magnetoresistance in a quantum anomalous Hall insulator".

[39] M. Winnerlein et al., Physical Review Materials vol. 1, 011201(R) (2017), DOI:10.1103/PhysRevMaterials.1.011201, "Epitaxy and structural properties of $(V,Bi,Sb)_2Te_3$ layers exhibiting the quantum anomalous Hall effect".

[40] M. Winnerlein, Doctoral thesis, URN:20-opus-211666, "Molecular beam epitaxy and characterization of the magnetic topological insulator $(V,Bi,Sb)_2Te_3$".

[41] S. Schreyeck, Doctoral thesis, URN:20-opus-145812, "Molecular beam epitaxy and characterization of Bi-based V_2VI_3 topological insulators".

[42] L. Vistoli et al., Nature Physics vol. 15, 67 (2019), DOI:10.1038/s41567-018-0307-5, "Giant topological Hall effect in correlated oxide thin films".

[43] Q. L. He et al., Nature Communications vol. 9, 2767 (2018), DOI:10.1038/s41467-018-05166-9, "Exchange-biasing topological charges by antiferromagnetism".

[44] L. Wang et al., Nature Materials vol. 17, 1087 (2018), DOI:10.1038/s41563-018-0204-4, "Ferroelectrically tunable magnetic skyrmions in ultrathin oxide heterostructures".

[45] C. Liu et al., Physical Review Letters vol. 119, 176809 (2017), DOI:10.1103/PhysRevLett.119.176809, "Dimensional crossover-induced topological Hall effect in a magnetic topological insulator".

[46] J. Matsuno et al., Science Advances vol. 2, e1600304 (2016), DOI:10.1126/sciadv.1600304, "Interface-driven topological Hall effect in $SrRuO_3$-$SrIrO_3$ bilayer".

[47] B. M. Ludbrook et al., Scientific Reports vol. 7, 13620 (2017), DOI:10.1038/s41598-017-13211-8, "Nucleation and annihilation of skyrmions in Mn_2CoAl observed through the topological Hall effect".

[48] Y. Ohuchi et al., Nature Communications vol. 9, 213 (2018), DOI:10.1038/s41467-017-02629-3, "Electric-field control of anomalous and topological Hall effects in oxide bilayer thin films".

[49] K. M. Fijalkowski et al., Proceedings: 2018 Conference on Precision Electromagnetic Measurements (CPEM 2018) (2018), DOI:10.1109/CPEM.2018.8500974, "On the nature of the quantum anomalous Hall effect".

[50] M. Götz et al., Proceedings: 2018 Conference on Precision Electromagnetic Measurements (CPEM 2018) (2018), DOI:10.1109/CPEM.2018.8501001, "Zero-field quantized anomalous Hall resistance of $(Bi,Sb)_2Te_3$".

[51] K. M. Fijalkowski et al., Nature Communications vol. 12, 5599 (2021), DOI:10.1038/s41467-021-25912-w, "Quantum anomalous Hall edge channels survive up to the Curie temperature".

[52] J. Zhang et al., Nature Communications vol. 2, 574 (2011), DOI:10.1038/ncomms1588, "Band structure engineering in $(Bi_{1-x}Sb_x)_2Te_3$ ternary topological insulators".

[53] M. Planck, Annalen der Physik vol. 1, 69 (1900), DOI:10.1002/andp.19003060105, "Ueber irreversible Strahlungsvorgaenge".

[54] D. Drung et al., Semiconductor Science and Technology vol. 22, 114004 (2009), DOI:10.1088/0953-2048/22/11/114004, "Improving the stability of cryogenic current comparator setups".

[55] F. J. Ahlers et al., Metrologia vol. 54, 516 (2017), DOI:10.1088/1681-7575/aa75d4, "Direct comparison of fractional and integer quantized Hall resistance".

[56] R. Ribeiro-Palau et al., Nature Nanotechnology vol. 10, 965 (2015), DOI:10.1038/nnano.2015.192, "Quantum Hall resistance standard in graphene devices under relaxed experimental conditions".

[57] M. Büttiker, Physical Review B vol. 38, 9375 (1988), DOI:10.1103/PhysRevB.38.9375, "Absence of backscattering in the quantum Hall effect in multiprobe conductors".

[58] K. M. Fijalkowski et al., Physical Review B vol. 103, 235111 (2021), DOI:10.1103/PhysRevB.103.235111, "Any axion insulator must be a bulk three-dimensional topological insulator".

[59] R. B. Laughlin, Physical Review B vol. 23, 5632(R) (1981), DOI:10.1103/PhysRevB.23.5632, "Quantized Hall conductivity in two dimensions".

[60] B. I. Halperin, Physical Review B vol. 25, 2185 (1982), DOI:10.1103/PhysRevB.25.2185, "Quantized Hall conductance, current-carrying edge states, and the existence of extended states in a two-dimensional disordered potential".

[61] D. E. Khmelnitskii, Pis'ma v Zhurnal Eksperimental'noi i Teoreticheskoi Fiziki vol. 38, 9, 454 (1988), "Quantization of Hall conductivity".

[62] A. M. M. Pruisken, Physical Review B vol. 32, 2636 (1985), DOI:10.1103/PhysRevB.32.2636, "Dilute instanton gas as the precursor to the integral quantum Hall effect".

[63] A. M. M. Pruisken, Physical Review Letters vol. 61, 1297 (1988), DOI:10.1103/PhysRevLett.61.1297, "Universal singularities in the integral quantum Hall effect".

[64] B. Huckestein, Reviews of Modern Physics vol. 67, 357 (1995), DOI:10.1103/RevModPhys.67.357, "Scaling theory of the integer quantum Hall effect".

[65] I. Ruzin et al., Physical Review Letters vol. 74, 154 (1995), DOI:10.1103/PhysRevLett.74.154, "Universal relation between longitudinal and transverse conductivities in quantum Hall effect".

[66] M. Hilke et al., Nature vol. 395, 675 (1998), DOI:10.1038/27160, "Experimental evidence for a two-dimensional quantized Hall insulator".

[67] M. Hilke et al., Europhysics Letters vol. 46, 775 (1999), DOI:10.1209/epl/i1999-00331-2, "Semicircle: An exact relation in the integer and fractional quantum Hall effect".

[68] J. Wang et al., Physical Review B vol. 89, 085106 (2014), DOI:10.1103/PhysRevB.89.085106, "Universal scaling of the quantum anomalous Hall plateau transition".

[69] J. Wang et al., Nature Communications vol. 6, 8474 (2015), DOI:10.1038/ncomms9474, "Metal-to-insulator switching in quantum anomalous Hall states".

[70] M. Mogi et al., Science Advances vol. 3, eaao1669 (2017), DOI:10.1126/sciadv.aao1669, "Tailoring tricolor structure of magnetic topological insulator for robust axion insulator".

[71] X. Wu et al., Nature Communications vol. 11, 4532 (2020), DOI:10.1038/s41467-020-18312-z, "Scaling behavior of the quantum phase transition from a quantum anomalous Hall insulator to an axion insulator".

[72] M. Mogi et al., Applied Physics Letters vol. 107, 182401 (2015), DOI:10.1063/1.4935075, "Magnetic modulation doping in topological insulators toward higher-temperature quantum anomalous Hall effect".

[73] Y. Ou et al., Advanced Materials vol. 30, 1703062 (2017), DOI:10.1002/adma.201703062, "Enhancing the quantum anomalous Hall effect by magnetic codoping in a topological insulator".

[74] M. Serlin et al., Science vol. 367, 6480, 900 (2020), DOI:10.1126/science.aay5533, "Intrinsic quantized anomalous Hall effect in a moire heterostructure".

[75] Y. Deng et al., Science vol. 367, 6480, 895 (2020), DOI:10.1126/science.aax8156, "Quantum anomalous Hall effect in intrinsic magnetic topological insulator $MnBi_2Te_4$".

[76] G. Qiu et al., Physical Review Letters vol. 128, 217704 (2022), DOI:10.1103/PhysRevLett.128.217704, "Mesoscopic transport of quantum anomalous Hall effect in the submicron size regime".

[77] K. M. Fijalkowski et al., ArXiv:2206.03972 (2022), "Macroscopic quantum tunneling of a topological ferromagnet".

[78] L.-J. Zhou et al., ArXiv:2207.08371 (2022), "Confinement-induced chiral edge channel interaction in quantum anomalous Hall insulators".

Acknowledgements.

Finally I want to thank the people who helped me in some way over the years.

- Prof. Dr. Charles Gould for a great guidance and help
- Prof. Dr. Laurens W. Molenkamp for this great opportunity to work in EP3
- Dr. Stefan Grauer for introducing me to the project, and making it easy for me to carry on the project
- Prof. Dr. Karl Brunner, Dr. Steffen Schreyeck, Dr. Martin Winnerlein, Dr. Nan Liu, and Martin Klement for an unlimited supply of great quality MBE samples
- Prof. Dr. Ronny Thomale for illuminating theoretical discussions
- Dr. Tanja Borzenko, and Dr. Johannes Kleinlein for always being willing to help with lithography problems
- Pankaj Mandal, and Matthias Hartl for great contributions to the project
- Volkmar Hock for keeping the clean room in excellent technical condition
- Our colleagues from PTB Braunschweig: Dr. Martin Götz, Eckart Pesel, Dr. Hansjörg Scherer, and Dr. Franz J. Ahlers for a fruitful collaboration on the metrological precision experiments on our samples
- Thesis reviewers: Prof. Dr. Charles Gould, Prof. Dr. Ronny Thomale, and Prof. Dr. Tomasz Dietl
- Defence jury: Prof. Dr. Charles Gould, Prof. Dr. Ronny Thomale, Prof. Dr. Tomasz Dietl, and Prof. Dr. Sebastian Klembt
- Dr. Saquib Shamim, and Dr. Mohamed Abdelghany for always being willing to help with equipment problems
- Dr. Marcin Syperek for guidance during my Bachelors and Masters studies
- Dariusz Kowalik for guiding me towards physics

- Pankaj Mandal, and Diptanu Roy for making our office a fun work environment
- All EP3 members, present and former, for a fantastic working atmosphere
- My friends and family who always supported me

Chciałbym jeszcze gorąco podziękować całej mojej rodzinie za ogromne wsparcie. Nie był bym tu gdzie jestem bez was.